Stimuli-Responsive Polymer-Based Colorimetric Sensors

by

Wildemar Stefanio Pereira Carvalho

A thesis submitted in partial fulfillment of the requirements for the degree of

Doctor of Philosophy

Department of Chemistry
University of Alberta

© Wildemar Stefanio Pereira Carvalho, 2020

Abstract

We have witnessed significant progress in the past few decades in the development of stimuli-responsive polymer-based smart materials. A great deal of work has been dedicated to the development of sensors and biosensors that are portable, inexpensive and easy-to-use to be used in resource limited settings where these technologies need to be incredibly robust. The Serpe group discovered colorimetric sensors that are composed of a highly packed pNIPAm-based microgel monolayer “sandwiched” between two thin reflective Au layers, forming an etalon structure. The versatility of the microgels, the ability to easily modify their composition to obtain different responsiveness, and their incorporation into an etalon device makes it possible to develop optical sensors for a numerous of applications. The color of the etalon is a result of light interference within its structure. The group has demonstrated in various publications their potential in detecting a number of analytes in aqueous solution. My Ph.D. research focused on the etalon fabrication process and exploring their ability to be used as portable sensors. Firstly, we developed a painting platform and fabricated highly uniform and reproducible etalon devices using the proposed “doctor blade” technique. We also demonstrated that the quality of the etalon devices is not affected when fabricated by different individuals. Furthermore, we decreased the size of the etalons down to 4 mm^2, which allows the fabrication of 1,024 etalons per batch. This is extremely important for larger scale production and commercialization of the technology. Following, a quality control procedure was developed and the etalon’s ability to predict solution pH was evaluated. Here, we characterized their color (RGB values) as a function of pH and studied the effects of variations on temperature, ionic strength and type of ions in solution on their pH measurement accuracy. Moreover, we also demonstrated their potential to be used as portable sensors for quality control. In collaboration with SolarDew International, the etalon devices were used to detect changes in ionic strength of distilled water. Finally, we investigated how the etalon devices respond to different ions belonging to the Hofmeister series and analysed their response kinetics. It was observed that the responses to ions could be predicted based on Hofmeister series and detailed analysis of the response kinetics could provide information of the type of ions in solution.

Preface

This thesis is an original work by Wildemar Carvalho under the supervision of Dr. Michael J. Serpe. The chapters of this thesis have not been published yet with exception of Chapter 5, which has been submitted for publication. Dr. Serpe was involved in the experimental design and the discussion of the results obtained in all the chapters.

In Chapter 2, I was responsible for the experimental design, data collection and analysis. Yu Wan and Anni Huang participated on the experimental procedure and Siyuan Guo and Yingnan Zhang participated on the design of the painting platform.

In Chapter 3, I was responsible for the experimental design, data collection, and data analysis. Menglian Wei and Xiaochen Dong also participated on the data collection and Keith Cuff was responsible for most of the data analysis. Yingnan Zhang and Nduka Ikpo participated in useful discussions.

In Chapter 4 and 5, I was again responsible for the experimental design, data collection and analysis. In Chapter 4, Anni Huang and Gaganpreet Jhajj also participated on the data collection while in Chapter 5, Cayo Lee and Adam Czarnecki participated on the data collection and Yingnan Zhang on important discussions.

In appendix A, Ryan Duruisseau-Kuntz and I contributed equally to the work presented. I participated on the experimental design and Duruisseau-Kuntz participated on the data collection. Menglian Wei also participated in the data collection. In Appendix B, Yu Wan helped participated on the micro fabrication process and Wei Zhang on important discussions.

Acknowledgement

Foremost, I would like to express my deep and sincere gratitude to my supervisor, Dr. Michael J. Serpe, for giving me the opportunity to conduct research in his laboratory and providing invaluable guidance throughout my research projects. Under his supervision, I learned the methodology to carry out research and to communicate my work as clear as possible. His enthusiasm and motivation in science has inspired me to continue to do research after my Ph.D studies. I am extremely grateful for his friendship, life advice, and for the great times we shared. Undoubtedly, it was an honor to work under his guidance. I would like to extend my thanks to his wife, Tiffany Stokes, for the great holiday parties and for patience during the times we took Mike away from home.

I cannot express enough thanks to my supervisory committee members, Dr. Richard McCreery and Dr. Robert Campbell for their valuable suggestions, challenging questions and constructive criticism on my research projects. I am also grateful to Dr. Sarah Styler and Dr. Arturo Sanchez-Azofeifa for participating in my candidacy examination and Dr. Mark McDermott and Dr. Russ Algar for agreeing to serve as the arm's length examiners for my final doctoral examination.

I would like to thank Gareth Lambkin from Biological Service for helping me during my project involving the detection of bacteria and Anita Weiler for answering my questions about the graduate program and making sure all the requirements were fulfilled. I am also grateful to Norman Gee, Yoram Apelblat, and Gregory Kiema for their assistance during my TA duties.

I thank my fellow labmates in the Serpe group and all the undergraduate students who worked with me, a special thanks to Andrews Ahiabu, Menglian Wei, Lauren Huybregts, Siyuan

Guo, Yingnan Zhang, and Wei Zhang. You guys definitely made this journey more fun. Thanks for sharing the up and down moments and for your encouragement during my research. A big thanks also goes to Keith Cuff for helping me with my data analysis.

I would like to thank my family and friends for their love, support, and encouragements. A special thanks to my dear friends Felipe Luiz, Shirley Oliveira, Geane Menezes, and Ricelli Gomes. I would like to express my deepest gratitude to my fiancé Michael Martel for his care, love, and support. Thank you for standing by me and for your encouragement when times got rough. My heartfelt thanks.

Finally, I would like to thank all the people who have supported me to complete my research work directly or indirectly.

Table of Contents

List of Figures

List of Tables

List of Schemes

List of Abbreviations

1/2/3D	One/two/three-dimensional
3-RBF	Three-neck round bottom flask
AAc	Acrylic acid
ACh	Acetylcholine
ADU	Analog-to-digital
AFM	Atomic force microscopy
APMAH	*N*-(3-aminopropyl) methacrylamide hydrochloride
APS	Ammonium persulfate
ATRP	Atom transfer radical polymerization
BIS	*N,N'*-methylene(bisacrylamide)
CIE	International Commission on Illumination
CMOS	Complementary metal-oxide-semiconductor
CNS	Central nervous system
CRP	Controlled/living free radical polymerization
DEAAM	*N,N'*-diethylacrylamide
DI	Deionized
DIC	Differential interference contrast
DLS	Dynamic light scattering
DMAEMA	2-(dimethylamino)ethyl methacrylate
DN	Digital number

DSPE-PEG-PDP	1,2-distearoyl-*sn*-glycero-3-phosphoethanolamine-*N*-poly(ethylene glycol)-2000-*N*-[3-(2-pyridyldithio)propionate]
E. coli	*Escherichia coli*
FTIR	Fourier-transform infrared spectroscopy
HA	Amphipathic a-helix peptide
HMDS	1,1,1,3,3,3-hexamethyldisilazane
IS	Ionic strength
K_a	Dissociation constant
KPS	Potassium persulfate
LEDs	Light-emitting diodes
LC-MS	Liquid chromatography-mass spectrometry
LCST	Lower critical solution temperature
MAAc	Methacrylic acid
MAE	Mean absolute error
MALDI-TOF-MS	Matrix-assisted laser desorption ionization time-of-flight mass spectrometry
MCH	6-mercapto-1-hexanol
NAChR	Nicotinic acetylcholine receptors
NBD-DPPE	1,2-dipalmitoyl-sn-glycero-3-phosphoethanolamine-N-(7-nitro-2-1,3-benzoxadiazol-4yl)
NIPAm	*N*-isopropylacrylamide
NIPMAM	Poly-*N*-isopropylmethacrylamide
PBS	Phosphate buffered saline

PC	Photonic crystals
pDEAAM	Poly(*N,N'*-diethylacrylamide)
pDMAEMA	Poly(2-(dimethylamino)ethyl methacrylate)
pDMAPS-MA	Poly(2-dimethyl[methacryloxyethyl] ammonium propane sulfonate)
pDMAPS-MAM	Poly(3-[*N*-(3-methacrylamidopropyl)-*N*,*N*-dimethyl] ammonium propane sulfonate)
PEG	Poly(ethylene glycol)
pEGMA	Poly(ethylene glycol methacrylate)
pMAm	Poly(methacrylamide)
pNAGA	Poly(*N*-acryloylglycinamide)
pNIPAm	Poly(*N*-isopropyl acrylamide)
pNIPAm-BIS	Poly(*N*-isopropyl acrylamide) microgel
pNIPAm-*co*-(%)AAc microgel	Poly(*N*-isopropyl acrylamide)-*co*-acrylic acid microgel
pNIPAm-*co*-(%)MAAc microgels	Poly(*N*-isopropyl acrylamide)-*co*-methacrylic acid microgel
pNIPAm-*co*-(%)VAAc microgels	Poly(*N*-isopropyl acrylamide)-*co*-vinylacetic acid microgel
PNS	Peripheral nervous system
POC	Point-of-care
POPC	1-palmitoyl-2-oleoyl-*sn*-glycero-3-phosphocholine
QCM	Quartz crystal microbalance
RAFT	Reversible addition fragmentation chain transfer
SEM	Scanning electron microscopy
SDS	Sodium dodecyl sulfate

SDGs	Sustainable development goals
SPR	Surface plasmon resonance
sRGB	Standard RGB
TDS	Total dissolved solids
TEM	Transmission electron microscopy
UCST	Upper critical solution temperature
UN	United Nations
VAAc	3-Butenoic acid
VPTT	Volume phase transition temperature
WHO	World Health Organization

Chapter 1

Introduction

1.1 Introduction to Stimuli-Responsive Polymers

Stimuli-responsive polymers, also known as smart polymers, are polymeric materials that have the ability to respond to changes in their environment (external stimuli) by changing their chemical and/or physical properties.[1-4] In nature, stimuli responsive behaviours can be observed in many living organisms, such as the sudden collapse of the *Mimosa pudica*'s leaves when touched,[5] the color changes in chameleons and cephalopod in response to their environment for camouflage,[6] the Venus flytrap snaps shut to catch its pray,[7] and the young sunflowers tracking the sun from east to west due to light responsive genes that regulates the plant growth.[8] Inspired by nature, synthetic stimuli-responsive polymers have been developed that respond to a variety of stimuli, such as pH,[9-10] ionic strength,[11-12] light,[13-15] mechanical force,[16-19] humidity,[20-21] electric/magnetic fields,[22-24] solvents,[25-26] and the presence of specific molecules.[27-28] These polymers can be synthesized through the polymerization of specific stimuli-sensitive monomers or by incorporating them physically or chemically into the polymer matrix. They can be designed to have different compositions and arrangements, such as linear polymers (homopolymers, di/triblock copolymer, random/statistical copolymers, and gradient copolymers) and non-linear polymers (start polymers and graft/branched polymers) as demonstrated in **Figure 1.1** where at least one of the monomers/block is stimuli-sensitive. Furthermore, they can be physically or chemically crosslinked to generate three-dimensional (3D) responsive polymer materials such as hydrogels and hydrogel particles (**Figure 1.1**).

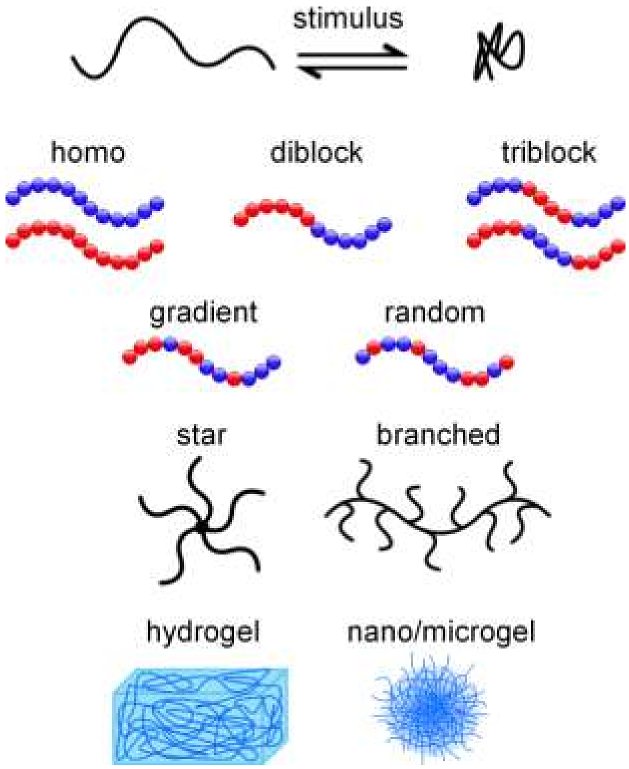

Figure 1.1 Illustrations of the stimuli-responsive polymers showing the variety of compositions and arrangements.

Frequently, these polymers produce observable/detectable changes in response to their environment due to the formation or interruption of secondary forces, such as hydrogen bonding, electrostatic interactions, and hydrophobic effects, the ionization of pendent groups (acid-base reactions) that results in osmotic pressure differentials, and due to entropy changes in the system. In other cases, however, the application of an external stimulus can result in more dramatic alterations in the polymer network, such as degradation of the polymer material due to the reversible or irreversible bond breakage of the polymer's backbone or the crosslinkers.

Due to the variety of polymer matrix and functional groups (stimuli responsive) available, smart polymer-based materials have been designed with a wide range of responsivities for industrial and scientific purposes over the years, exploring new and innovative applications. They have been engineered into many forms including bulk/thin films, particles (nano/micro), and composites that found applications in the development of sensors and biosensors, actuators, for controlled and triggered drug delivery, and smart coatings.[29] In this chapter, stimuli-responsive polymers will be discussed with focus on thermoresponsive polymers as it was used for all investigations presented in this dissertation.

1.2 Thermoresponsive Polymers

Polymers that respond to temperature changes are the most well-studied and best understood systems in the class of stimuli responsive polymers due to their large changes in solubility, refractive index, and volume that can be easily manipulated over a wide range of temperatures.[30-32] Temperature-responsive polymers, also known as thermoresponsive polymers, exhibit a critical solution temperature where the polymer changes phase. They can be described as having a lower critical solution temperature (LCST) or an upper critical solution temperature (UCST). A polymer is considered to has an LCST if the polymer undergoes a transition behaviour from soluble (monophasic) to an insoluble (biphasic) state when the temperature is increased above the critical temperature. On the opposite, a polymer is considered to has an UCST if the polymer undergoes a transition behaviour from insoluble to soluble when the temperature is raised, respectively.[33-35] The temperature induced phase transition in these thermoresponsive polymers is highly reversible. For instance, if the temperature is decreased below the transition temperature for LCST-polymers, they become soluble again.

The most common type of UCST polymers are so-called poly(betaine)s (also known as polyzwitterions) that contains both anionic and cationic species in every repeat unit.[36] Some examples of poly(betaine)s that exhibit UCST behavior include poly(2-dimethyl[methacryloxyethyl] ammonium propane sulfonate) (pDMAPS-MA) and poly(3-[*N*-(3-methacrylamidopropyl)-*N*,*N*-dimethyl] ammonium propane sulfonate) (pDMAPS-MAM).[35] Other non-zwitterionic polymers that also show UCST include poly(methacrylamide) (pMAm)[37] and poly(N-acryloylglycinamide) (pNAGA).[38] Most common LCST polymers are poly(*N*-isopropyl acrylamide) (pNIPAm), poly(*N,N'*-diethylacrylamide) (pDEAAM), poly(ethylene glycol methacrylate) (pEGMA), and poly(2-(dimethylamino)ethyl methacrylate) (pDMAEMA). The structures of these UCST and LCST thermoresponsive polymers are shown in **Figure 1.2**. In this dissertation, our attention will be focused on LCST polymers, specifically those composed of pNIPAm which has an LCST of 32 °C and is one of the most studied thermoresponsive polymer not only because of its LCST is close to the physiological temperature, making it very interesting for biomedical applications, but also due to its robust tunable phase behaviour.[3] PNIPAm undergoes an abruptly coil-to-globule transition in aqueous solution when the $T > 32$ °C that can be explained based on the changes in the competition between inter/intramolecular interactions below and above pNIPAm's LCST.

For LCST polymers, the temperature at which point the mixing of the two phases changes from spontaneous to non-spontaneous normally defines their LCST in aqueous solutions. This process was described as an entropy-driven transition by Heskins and Guillet in 1968 and can be explained thermodynamically based on Gibbs free energy equation (Equation 1.1).[39]

$$\Delta G = \Delta H - T\Delta S \tag{1.1}$$

where ΔG corresponds to the changes in the free energy of dissolving the polymer in water, ΔH corresponds to the changes in enthalpy of the dissolution, T is the solution temperature in Kelvin, and ΔS is the changes in the system entropy as a result of the of the interactions between the polymer chains and solvent water molecules. From a thermodynamic perspective, the transition from soluble to a phase separation when the temperature is increased implies a negative ΔG at lower temperatures that becomes more positive as the temperature increases, meaning that the polymer dissolution is nonspontaneous and resulting in a phase separation. This is only possible because at lower temperatures (T < LCST), ΔH is negative as water molecules arrange themselves in a cage like structure around the polymer backbone and isopropyl groups, resulting in ΔS being also negative. In the case of pNIPAm, when it is dissolved in water at lower temperatures, ΔH makes a negative contribution due to the formation of intermolecular hydrogel bonding between water molecules and the C=O and N-H groups in the pNIPAm chains, and the ΔS is negative as water loss entropy due to the formation of an ordered "cage-like" structure surrounding the hydrophobic isopropyl groups and the polymers backbone, resulting in a positive entropic contribution ($-T\Delta S$) that tends to increase with temperature. Therefore, $\Delta G < 0$ at lower temperatures as the enthalpy contribution is dominant and the dissolution of the polymer is spontaneous.

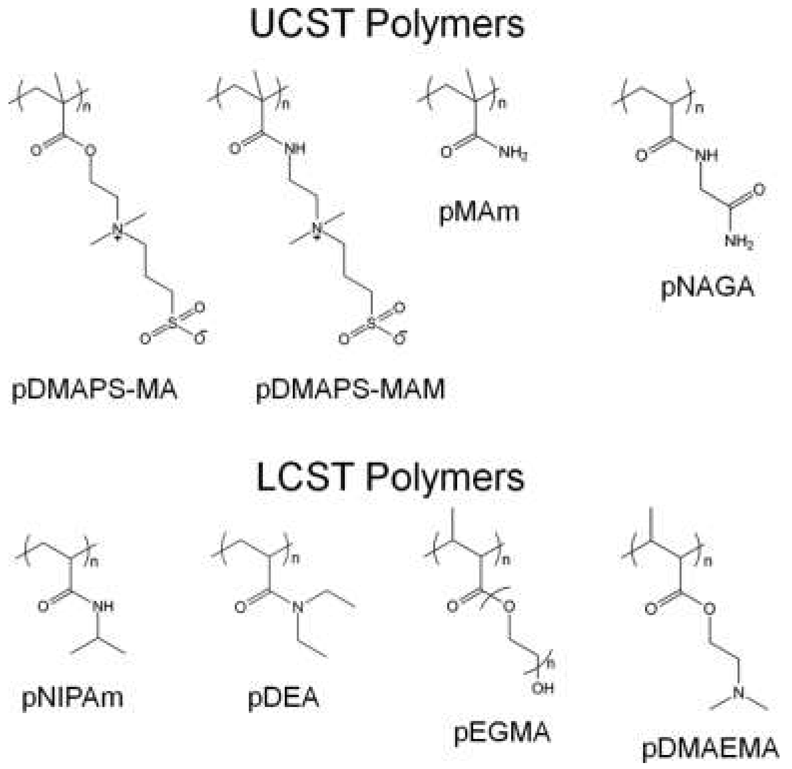

Figure 1.2 Structures of some common thermoresponsive polymer that exhibit UCST (top) and LCST (bottom).

Upon increasing the temperature, ΔG becomes more positive and at T > LCST, the entropy term becomes dominant and overcomes ΔH, resulting in $\Delta G > 0$. This leads to a nonspontaneous dissolution of the polymer and a phase separation occurs where intramolecular interactions are favored and the polymer collapse in a globule conformation as shown in **Figure 1.3(a)**. This process is also illustrated on the molecular level in **Figure 1.3(b),** where the inter/intramolecular interactions between pNIPAm and water molecules at low and high temperatures is shown. Furthermore, the phase transition behaviour is a fully reversible process, where the pNIPAm becomes soluble again if the temperature is decreased below its LCST. It is important to point out that the polymer is never fully dehydrated at T > LCST and the degree of dehydration highly depends on the hydrophilicity of the polymer. Indeed, studies done by Maeda *et al.* on the hydration state of pNIPAm during the coil-to-globule transition using fourier-transform infrared spectroscopy (FTIR) revealed that the polymer is only partially dehydrated at T > LCST, retaining around 66% of the water that is directly interacting with the polymer even in its fully collapsed state.[40] The authors observed the formation of inter/intra chain hydrogen bonding interactions in the amide group but most (87%) of the hydrogen bonding of the C=O groups with water molecules was unchanged. Furthermore, making the polymer more hydrophilic causes more retention of water molecules in the collapsed polymer globules.

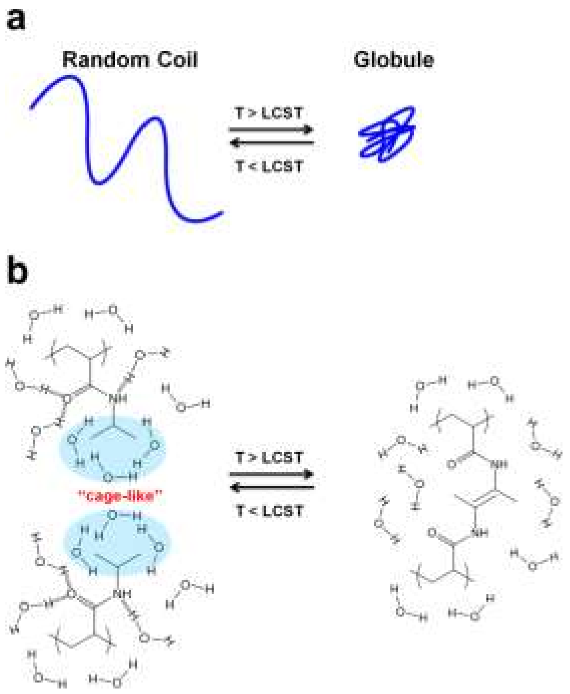

Figure 1.3 (a) Illustration of the conformational change induced by temperature changes on a pNIPAm molecule and (b) details of this transition showing inter/intramolecular interactions of pNIPAm chains with water molecules. Hydrogen bonding between the C=O and N-H groups in the polymer chains also occurs at high temperatures (T > LCST) but it is omitted in this scheme.

These globules formed when the temperature is raised above pNIPAm's LCST grow into aggregates composed of a number of polymer molecules and in many cases stop growing when they reach a certain size. A colloidal suspension is formed with the dispersed phase made of stable polymer particles, known as mesoglobules, with a typical radius in the range of 50-200 nm.[41-42] Pelton *et al.* suggested that the stability of these particles was due to electrostatic repulsion.[43] They found that the particles were weakly negatively charged, which was attributed to the presence of negatively charged end groups in some of the polymer chain introduced by the persulphate radicals used in the polymerization reaction. Winnik *et al.* further explored the properties of the mesoglobules and found that their formation happens in a narrow temperature range close to the transition temperature, where phase-separated particles merge and grow in size and mass.[44] As the temperature is further increased, the mesoglobules undergo a transition from fluid like particles into rigid spheres that are unable to merge or further grow upon collision or chain exchange between the polymer particles. The authors also found that, even though a significant number of water molecules are firmly attached to the polymer mesoglobule as demonstrated by Maeda *et al.*,[40] the water molecule loosely bound to the polymer chain at low temperatures are ejected from the mesoglobule into the external bulk water as indicated by an increased in the rigidity of the mesoglobules. The driving force for this transformation still remains unclear.

Generally, the LCST of thermoresponsive polymers is affected by the hydrophilic and hydrophobic nature of the substituent groups. This is because their LCST is particularly dependent on the degree of hydrogen bonding between the solvent water molecules and the substituent groups. Polymers that are more hydrated have higher LCST than less hydrated polymers. For instance, when pNIPAm is copolymerized with more hydrophilic monomers such as acrylamide and acrylic acid, its LCST is shifted to higher temperatures or even disappears.[45-47] On the contrary, incorporation of hydrophobic monomers such as N-butylacrylamide and Nhexadecylacrylamide usually shifts its LCST to lower temperatures.[3, 48] The possibility to tune the LCST of pNIPAm from < 0 to > 100 °C by incorporating hydrophilic or hydrophobic comonomers is essential to develop materials for specific applications, especially in the case of drug delivery systems.[3, 49]

Stimuli-responsive polymers can be prepared by free radical polymerization of the responsive vinyl/acryl monomers in the presence of an initiator.[50] Although conventional free radical polymerization provides a simple route, is cost-effective, relatively insensitive to impurities, and the vinyl/acryl monomers are easily polymerized, a few disadvantages include uncontrolled free reactive monomer levels, the molecular weight, molecular weight distribution and complications in synthesizing well-defined copolymers. The growing demand for preparing well-defined functional polymer materials with control over their architecture lead to the development of new methods that produce very uniform molecules with narrowly defined structures, molecular weight, which preserves chain end functionality essential for preparing block copolymers.[51] These methods are known as controlled/living free radical polymerization (CRP) and include atom transfer radical polymerization (ATRP)[52-53] and reversible addition fragmentation chain transfer (RAFT).[54-55] The common ground in these methods is that they control the number reactive radicals during the polymerization and they display a living character where chain termination or transfer is absent, meaning that the end of the growing chain is still active and is able to continue polymerization once the initial monomer is consumed by adding more monomers. In the case of pNIPAm, free radical precipitation polymerization reaction is normally carried out in aqueous solution using the monomer *N*-isopropylacrylamide (NIPAm) to obtain single polymer chains. Temperatures can vary from 50 to 75 °C and common initiators used include ammonium persulfate and potassium persulfate.[3] Variations in the initiator and monomer concentrations can result in polymers with different molecular weights. In addition, pNIPAm can be crosslink to produce thermoresponsive bulk hydrogels and microgel particles. The next section we will be focused on the properties and polymerization routes for synthesizing pNIPAm-based microgels.

1.2.1 Thermoresponsive pNIPAm-Based Microgels

Microgels are highly porous hydrogel particles composed of crosslinked networks of hydrophilic polymers with average diameters ranging from 50 nm to 5 µm,[56] although the synthesis of larger particles (ca. 2 mm) have been reported.[57] In this dissertation, chemically crosslinked pNIPAm-based microgels were used for some investigations. First synthesized in Pelton's lab,[58] thermoresponsive pNIPAm-based microgels also undergo a reversible phase transition between 32 and 35 ^{o}C that is often referred to as the volume phase-transition temperature (VPTT), which is close to the LCST of linear pNIPAm chains. In this case, the microgels are highly swollen (extremely hydrated) at $T < \text{VPTT}$, containing around 82% of water by volume and have low refractive index difference with water. However, when the temperature increases above its VPTT, the microgels undergo a reversible deswelling transition, assuming a volume that is 10-times less than its volume in the swollen state and retaining only ~25% of its initial water content.[56, 59] This is accompanied by an increase in their refractive index which makes it possible to track the swelling/deswelling behaviour using light scattering techniques such as dynamic light scattering (DLS) and UV-vis absorption. Like linear pNIPAm, the properties of the microgels also depend on the balance between polymer-polymer vs. polymer-water interactions. As such, their physical properties like swelling degree (particle size), refractive index, and the VPTT can be fine-tuned by introducing functional comonomers to produce microgels responsive to not only temperature, but pH, ionic strength, solvent composition, and light. Furthermore, their response is much faster in response to external stimuli compared to hydrogels/macrogels due to their dimensions, having much higher surface area by volume, whereas the response from hydrogels or macrogels is limited due to the shrink of the exterior layer that prevents the water flow from the interior to the exterior.[56] **Figure 1.4** shows the temperature-induced transition from a swollen to collapsed state for pNIPAm microgels.

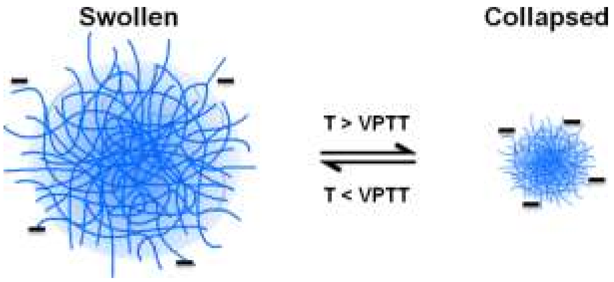

Figure 1.4 Schematic illustration of the temperature-induced volume change of pNIPAm-based microgels. The microgels have few negatively charged groups at end of chains that are incorporated by the persulfate initiator which makes them slightly negatively charged. Microgels positively charged are possible using cationic initiators.

Given the extensive interest in pNIPAm-based microgels, a number of polymerization routes have been explored aiming to control their size, size distribution, and functionality. For this dissertation, we exclusively used surfactant-free free radical precipitation polymerization to synthesize all microgels, which is similar to the polymerization method used to prepare single pNIPAm chains, but with the addition of a crosslinking agent. Here, we chemically crosslinked the microgels using *N,N'*-methylene(bisacrylamide) (BIS) as the crosslinker. The polymerization reaction is carried out in a three-neck round bottom flask (3-RBF) containing water where the principal monomer, NIPAm, and the crosslinker, BIS, are dissolved. The monomer solution is then purged with N_2 gas while stirring and heated to 70 °C for over 1 h. Purging the monomer solution with N_2 is extremely important to remove any dissolved O_2 molecules to avoid quenching of the free radicals, which can slow down the reaction or even prevent it from occurring.[60] The polymerization reaction is initiated by quickly adding the free radical initiator, such as ammonium persulfate (APS) or potassium persulfate (KPS), to the heated monomer solution. The APS/KPS decomposes at high temperatures (50-70 ^{o}C) to produce sulfate radicals that are able to react with the monomers and crosslinkers in solution, thereby initiating their polymerization. Due to the high temperature and its quick addition, the APS is decomposed at a fast rate, leading to a homogeneous nucleation. In addition, high temperature is required to trigger the collapse of the growing pNIPAm oligomers that, upon reaching a critical length (~10 monomer units), collapse and form colloidally unstable precursor particles that serve as seeds for the microgel growth.[39, 60-61] This happens because the solution temperature is far above the VPTT of the formed polymer chains. Studies done by Heskins and Guillet on the phase separation of linear pNIPAm suggest that the LCST was not affected by the polymer's molecular weight.[39] Thus, when achieving a critical length, all the polymer chains collapse. The precursor particles can grow by aggregation with other particles to form large colloidal stable hydrogel particles; by depositing onto an existing colloidally stable particle; or by addition of monomers or capturing oligoradicals.[62] Upon reaching a critical size, the microgel particles are stabilized by the negative charges incorporated into the polymer chains from the initiator fragments during the nucleation and particle growth process. At this point, the microgels are in the collapsed state as T > VPTT and have high charge density on the surface as indicated by high electrophoretic mobility, suggesting that in low ionic strength and surfactant free conditions, the electrostatic repulsion contribute to their colloidal stability.[59] Early studies done by Pelton *et al.* also suggested that the dehydrated microgels at T > VPTT are stabilized by electrostatic forces as the microgels coagulated in the presence of electrolytes ($CaCl_2$).[58] It is also important to note that even though the microgels are in a collapsed state, they still contain large amount of water. **Figure 1.5** displays this mechanism for the formation of microgel particles using precipitation polymerization. Upon cooling the pNIPAm microgel, they become soluble and swell. In the swollen state, the charge density on the microgel surface decreases as demonstrated by their low electrophoretic mobility, implying that the colloidal stability at lower temperatures is not caused by electrostatic repulsion.[59] However, it was proposed that the polymer chain extending from the microgels act as steric stabilizers and the van der Waal's attraction between the highly hydrated microgels are very low, giving their colloidal stability.[56, 60] In addition, even though their charge density is low when hydrated, the presence of charged groups introduces a dependency of their swelling behavior on electrolyte concentration.[63-64] **Figure 1.6** shows transmission electron microscopic (TEM) images for pNIPAm microgels prepared by free radical precipitation polymerization. A significant amount of non-crosslinked polymer chains is produced during the polymerization reaction, which should be removed from the microgels. This can be accomplished by centrifuging the resultant suspension and resuspending it in fresh water for multiple times or by dialysis.

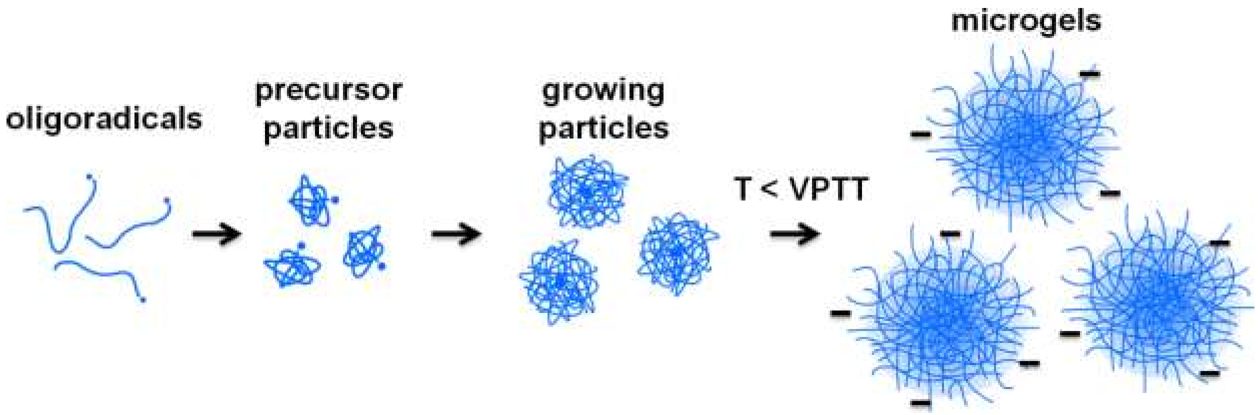

Figure 1.5 Mechanism for the formation of microgel particles via free radical precipitation polymerization. Initially, pNIPAm chains forms and grow up to a critical chain length, after which they collapse forming precursor particles. Following, the precursor particles grow until reaching a critical size where it becomes stable and stop growing.

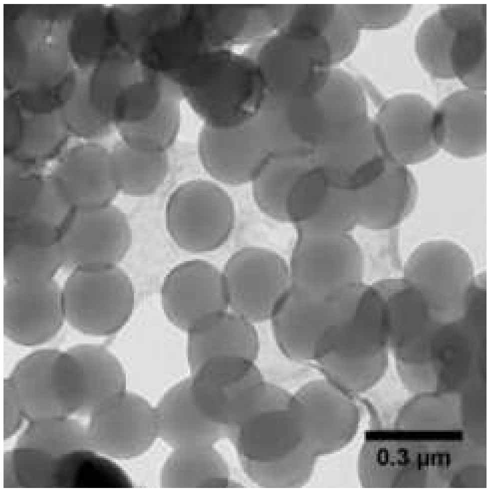

Figure 1.6 TEM image of PNIPAm microgels synthesized by surfactant-free free radical precipitation polymerization.

Preparation of microgels via free radical precipitation polymerization result remarkably uniform particles and offers several advantages including particle size control (from 100 nm to 3 μm) and functionality. The final size of the microgels is affected by several factors, such as reaction temperature, the presence and concentration of surfactants, and ionic strength. The synthesis of microgels at high temperature tends to produce microgels smaller than those formed at lower temperatures.[65] Wu *et al.* observed that microgels synthesized at 70 °C were 10% smaller than the microgels prepared at 50 °C.[60] Furthermore, they observed that the particles grew quicker at 70 °C than at 50 °C and that the reaction at 70 °C yielded more particles as the initial monomers were the same and the final conversion of the monomers were high for both reactions. The smaller size for microgels prepared at high temperature is attributed to the faster activation of the initiator, resulting in a larger conversion of the monomers into precursor particles (seeds). The remaining monomers are distributed among a large population of precursor particles, resulting in microgels with smaller size. These particles, however, are limited to the submicron range. A new free radical precipitation polymerization method was introduced by Lyon's groups to synthesize larger diameters (2.5 – 5 μm) particles.[66] The authors used a programmed temperature ramp from 45 to 65 °C during the nucleation stage to control the decomposition rate of the initiator (control the amount of seed formed) and the formation of oligomeric radicals. The high monomer concentration at lower temperature favors the chain propagation rather than the nucleation and the precursors grow larger. The reaction temperature was then increased to 65 °C to increase the reaction kinetics as the monomer concentration and the propagation rate decreases over time. Moreover, the size of microgels can be controlled by addition of inorganic salts and/or ionic surfactants to the reaction mixture. Usually, increasing the ionic strength tends to increase the microgel size.[67-68] This is primarily due to a decrease in the electrostatic stabilization of the charged precursor particles when the solution ionic strength is increased while attractive forces increase, causing them to easily aggregate and a high rate of coalescence to occur, resulting in larger particle sizes. Consequently, the aggregation process is affected by the concentration of ions in solution. However, very high salinity conditions tend to decrease the solubility of the monomer and the growing polymer chains, causing them to precipitate and resul in small polydisperse particles.[68]

To synthesize smaller microgels, the growing precursor particles must be stabilized earlier in the reaction. The charges incorporated into the polymer chain from the ionic initiator are not enough to provide colloidal stability to the small precursor particles. Therefore, ionic surfactant can be added to the polymerization reaction to impart stability of the precursor particles in the early stages and minimize their growth by aggregation. Therefore, the growth of particles is likely to occur through oligomer or monomer addition rather than the coalescence of the precursor particles. Pelton and coworkers showed that the presence of sodium dodecyl sulfate (SDS) at low concentrations (up to 1.15 g/L) can produce more uniform pNIPAm particles than those obtained using surfactant-free free radical precipitation polymerization and that the average particle size decreased when the SDS concentration was increased.[69] Moreover, microgels size can also be controlled by the nature of the crosslinker. In another study, Lyon's group also used SDS for stabilization of pNIPAm microgels synthesized using poly(ethylene glycol) (PEG) diacrylates of different molecular weights.[70]

The physical properties of pNIPAm microgels including its VPTT can be controlled by copolymerization of NIPAm with other comonomers having different degrees of hydrophilicity/hydrophobicity, by varying nature of the crosslinker, or by controlling the distribution of the monomers in the particle architecture. Using free-radical precipitation polymerization, functional comonomers are introduced together with the primary monomer, NIPAm, and the crosslinker before adding the ionic initiator. The functional comonomers become covalently attached to the polymer network of the microgels through the polymerization process, affecting their colloidal stability and swelling behaviour. Richtering's group prepared via free radical precipitation polymerization copolymer microgels with different portions (ratios) of NIPAm and *N,N'*-diethylacrylamide (DEAAM) (see **Figure 1.2**) and observed that the VPTT, characterized by DLS, was extremely influenced by the monomer composition.[71] Interestingly, they found that the VPTT of microgels composed of 60% DEAAM and 40% NIPAm was lower than that of both homopolymer microgels. The authors attributed the dependence of VPTT on the monomer composition due to the favored hydrogen bonding between DEAAM and NIPAm. However, no linear relationship between the copolymer composition and the VPTT was observed. Richtering and coworkers further investigated how the macromolecular architecture of the copolymer influences in the VPTT.[72] In this case, the authors prepared microgels composed of DEAAM/NIPAm, DEAAM/poly-*N*-isopropylmethacrylamide (NIPMAM) at various ratios and core-shell microgels composed of DEAAM (core) and NIPAm (shell). The same non-linear dependence of phenomena was also observed for DEAAM/NIPMAM systems. However, due to the modified backbone of NIPMAM containing a methyl group, the backbone flexibility of the entire copolymer system is restricted, hindering the formation of hydrogen bonding between the monomer groups (lower intramolecular interactions) and increasing the VPTT of the copolymer to higher temperatures compared to NIPAm systems. To synthesize the core-shell DEAAM/NIPAM microgels, the authors first prepared the core DEAAM particles by surfactant-aided radical precipitation polymerization that served as nuclei for the following polymerization of the pNIPAm shell.

Besides tuning the VPTT, microgels can be synthesized to respond to a variety of external stimuli by incorporating functional comonomers. Numerous water-soluble functional comonomers are available to produce microgels with multiple functionalities. For instance, adding ionisable comonomers such as acrylic acid (AAc), methacrylic acid (MAAc), or/and 2-

(dimethylamino)ethyl methacrylate (DMAEMA) can result in microgels responsive to pH, ionic strength, and temperature. These systems will be discussed in details in the next section.

1.3 pH Responsive pNIPAm-Based Microgels

pH-responsive polymers undergo changes in their physical properties in response to a change in the environmental pH due to the presence of weak acid or base groups that can either accept or release protons depending on the solution pH. The most commonly used functional pH responsive monomers are those having carboxyl and tertiary amine groups that can be ionized similar to the ionization of monoacids or monobasics. However, unlike small molecules, to achieve full ionization in these systems is difficult as the protonation of different sites in the polymer is affected by the ionization state of adjacent units and the distribution of ionisable units. Therefore, the apparent dissociation constant (K_a) and pK_a are different from that of the corresponding monoacid/monobasic. The structure for some monomers having weak acid and base units is shown in **Figure 1.7**. When these monomers are incorporated into the microgels through free radical precipitation polymerization, the swelling properties of the resultant pNIPAm-based microgels depend on the solution pH and ionic strength in addition to temperature. For instance, microgels containing carboxylic acid groups swell at high pH and shrink at low pH. The swelling of ionic hydrogels have been described by Paul Flory and others based on Donnan equilibrium theory.[73-75] The charge density of the microgels increases with pH as the carboxylic groups become deprotonated and negatively charged. The increase in charge density as a function of pH causes an increase in the osmotic pressure exerted by the mobile ions screening the fixed charges. Moreover, increasing the pH gives rise to internal charge repulsions between the neighboring deprotonated carboxylic groups. The increase in osmotic pressure and internal charge repulsions with pH causes the microgels to swell. However, when the pH is decreased, the anionic microgels shrink due to lower charge-charge repulsion forces and reduced osmotic pressure. The swelling-deswelling transition is affected by any condition that can interfere in the electrostatic repulsions, such as the ionic strength and the type of the mobile counterions. For instance, at higher pH values (pH >> pK_a), the carboxylic groups in the polymer become less ionized and the internal charge repulsion is reduced due to the screening of the charges by the mobile ions (Na^+ and OH^-), causing the microgels to shrink instead. It is not surprising that the swelling properties of these microgels are also affected by the amount of comonomer incorporated as it influences in the total charge density.

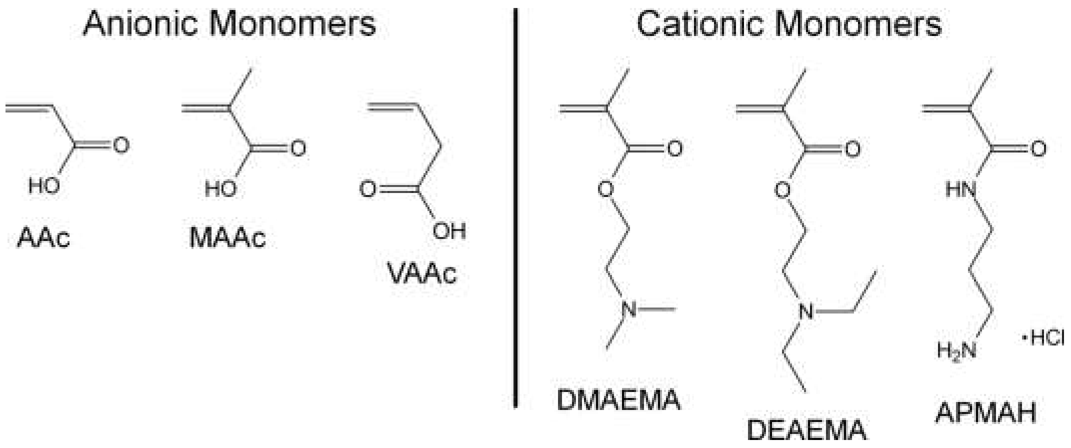

Figure 1.7 Examples of anionic and cationic monomers. From left to right are acrylic acid, methacrylic acid, vinylacetic acid, 2-(dimethylamino)ethyl methacrylate, 2-(diethylamino)ethyl methacrylate, and N-(3-aminopropyl)methacrylamide hydrochloride.

Snowden *et al.* reported the preparation of microgels containing 5% AAc and how temperature, pH and ionic strength affected their swelling properties and temperature response.[76] The authors observed that in the absence of electrolytes, the microgels are highly swollen but their hydrodynamic diameter decreased when sodium chloride concentration was increased from 0.001 to 0.1 M at 25 °C, pH 6. They attributed this deswelling behaviour to the electrolyte screening of the internal charge repulsion. Furthermore, they observed that this behaviour was fully reversible. When the electrolytes were removed from the microgels by dialysis, they expanded to their original size in water (electrolyte-free). At very low electrolyte concentration (0.001 M NaCl) and temperature (25 ^{o}C), the hydrodynamic diameter of the microgels increased when the pH was raised from 2.6 to 9.5 with highest increment between pH 3.9 and 6, around the pK_a of the AAc groups. While investigating how the incorporation of AAc would affect the thermoresponsive properties of the microgels, the authors observed that the microgels have a larger hydrodynamic diameter at pH 6.5 than at lower pH values at all temperatures investigated. In addition, their response behaviour to temperature was similar to the behaviour of pure pNIPAm microgels (not containing AAc) at low pH values, although the LCST was shifted to 34 ^{o}C. However, the decrease of the hydrodynamic diameter with increasing the temperature at high pH values was less pronounced and the LCST was shifted to 55 ^{o}C, implying that the negatively charged groups originated from the AAc groups greatly affect their temperature response behaviour. These studies were also performed at very low electrolyte concentration (0.001 M NaCl). Eimer and coworkers further investigated the influence of charge density on the swelling properties of pNIPAm microgels by incorporating different amounts of AAc.[77] The authors observed that at pH 7 and salt-free suspensions, the swelling/deswelling capacity of microgels containing AAc was significantly increased compared to pure pNIPAm microgels and two phase transitions were observed for higher AAc content (12.5%). The two phase transition was accompanied by an increase in the solution pH which the authors used to explain this behaviour. They observed that at low temperatures, the hydrodynamic diameter of the microgels increases with pH in salt-free solutions, similar to the observations made by Snowden *et al.*, however, depending on the pH, the microgels collapse at their VPTT and quickly coagulate in response to temperature. Furthermore, the microgels with higher AAc content showed higher swelling/deswelling degree in response to pH.

1.4 pNIPAm-Based Etalon Optical Interferometers

In 2010, Serpe's group introduced a new class of materials capable of color tunability based on pNIPAm microgels, which they called etalon interferometers, or simply etalons.[78] Since then, they have demonstrated their potential for a numerous applications including drug delivery and sensing/biosensing applications.[79-84] Etalons are composed of a highly packed microgel layer sandwiched between two thin reflective Au layers. These assemblies exhibit colors and have characteristic peaks in the reflectance spectra, which are sensitive to the swelling state of the pNIPAm microgels. The color of etalons is a result of light interference within its structure, similar to an etalon interferometer. When light strikes the material, some of the light is reflected by the first Au layer and some enters the cavity consisting of the microgel layer where it undergoes multiple internal reflections. As a result, constructive and destructive interferences occur, resulting in the reflection/transmission of specific wavelengths, which can be predicted based on Equation 1.1:

$$\lambda m = 2d\eta cos\theta \tag{1.1}$$

where λ is the reflected/transmitted wavelength, m is the order of reflection (an integer for constructive interference), η is the refractive index of the microgel layer, d is the distance between the two reflective Au layers, and θ is angle of incident light. Hu and Serpe demonstrated empirically when investigating the etalons response hysteresis that the color of the etalons is mainly dictated by the distance between the Au layers, which is controlled by the microgel layer thickness.[74] As the microgel layer is made of pNIPAm, the thickness decreases when the temperature is increased above 32 °C, decreasing the distance between the two Au layers and resulting in a color change. Furthermore, etalon devices can be prepared to respond to a verity of external stimuli by simply changing the composition of the microgels. In one example, Islam and Serpe reported a label-free assay for DNA concentration using etalons composed of pNIPAm microgels containing 5% of N-(3-aminopropyl) methacrylamide hydrochloride (APMAH), which gives the microgels a cationic characteristic.[85] Upon DNA exposure, the cationic microgels shrink due to a decreased in the electrostatic repulsion caused by the negatively charged DNA backbone.

1.5 Conclusions

Stimuli responsive polymers have been used to design smart materials such as actuators, drug delivery systems, and sensor/biosensors that respond to a variety of external stimuli. The design and fabrication of smart materials is rapidly evolving and, in most approaches, thermo responsive polymers have been applied to develop such materials. The Serpe group has developed microgel-based interferometers (etalons) using pNIPAm-based microgels and applied these color tunable devices for the development of sensors and biosensors. In several publications the sensors have demonstrated the ability to detect changes in solution temperature, pH, and quantify various biomolecules by simply engineering the microgels to swell/deswell in response to the target analyte. The etalon devices are easy to use, inexpensive, reusable, can be made portable, and they require no electricity to operate. Therefore, they show promising potential for point-of-care applications that are needed in remote areas and developing countries. In Chapter 2 of this dissertation, we describe the fabrication of a platform that uses the doctor blade technique to fabricate in large scale, reproducible etalon devices of high color uniformity. Further, the ability of the etalons to be used as portable sensors is described in Chapter 3 and 4 where, for the first time, their response was characterized using their digital color. Moreover, the color change of the etalons was characterized for different types of salts belonging to the Hofmeister series as described in Chapter 4. This is of great interest when using these optical devices for ion sensing applications. The findings described here are very important for future studies in our group and are essential for taking the technology to the next level where they can be used as portable sensors and leads to a potential commercialization of the technology. Moreover, several other areas can directly benefit from the sensing capability and portability the etalon devices, especially in the area of medical diagnosis and water quality monitoring systems.

Chapter 2

Fabrication of High Purity Color and Uniform Etalon Devices by Doctor Blade Technique

2.1 Introduction

Photonic crystals (PC) are highly ordered optical structures periodically arranged and composed of two or more dielectric materials with varying refractive index that can be used to control and manipulate the propagation and transmission of light. Their unique optical properties are a result of the dielectric periodicity at the length scale of the electromagnetic waves striking the material. When light propagates through the PC, it undergoes interferences that lead to the formation of a photonic band gap. This band consists of frequencies in which electromagnetic waves cannot be transmitted through the material due to destructive interference, which leads them to display distinct structural colors.[86-87] The photonic band gap can be modulated by changing the lattice parameters and the refractive indexes of the materials. PCs have been the subject of many investigations with potential applications in solar cells[87-89], development of colorimetric sensors[90-92], biosensors[93-94], waveguides (optical filters)[95-96], and displays[97-98]. They can be classified as one-dimensional (1D), two-dimensional (2D), or three-dimensional (3D) depending on their spatial periodic arrangements and variations in their refractive index/dielectric constants. Particularly, 1D PCs consist of dielectric layers of alternating high- and low-refractive index periodically arranged in only one dimension have been extensively studied.[99] Examples of 1D PCs are dielectric mirrors, Bragg reflectors, dichroic filters, antireflection coatings, and Fabry-Pérot etalons or interferometers. A schematic illustration of a typical Fabry-Pérot etalon (or simply etalon) is displayed in **Figure 2.1(a)**. It consists of two parallel reflective surfaces separated by a thin dielectric layer.[100-101] Their optical properties are a result of multiple beam interference between the two reflecting surfaces (mirrors). That is, when light enters the cavity, it undergoes multiple internal reflections, resulting in constructive and destructive interference and specific wavelengths of light being reflected/transmitted. The purpose of the two reflective surfaces, the distance between them, and the refractive index of the dielectric material is to create a path length difference between the transmitted/reflected wavelengths, which dictates where the waves are in phase or not. Constructive interference occurs when the transmitted/reflected wavelengths are in phase, and can be predicted using Equation 2.1:

$$\lambda m = 2d\eta cos\theta \tag{2.1}$$

where λ is the maximum reflected/trasmitted wavelength, m is an integer for constructive interference (or order of reflection), η is the refractive index of the dielectric material, d is the distance between the two reflective mirrors, and θ is angle of incident light. The etalon will appear visually colored when constructive interferences occur in the visible region of the electromagnetic spectrum. Their visible color depends on the wavelength of the light, its incident angle, the thickness of the etalon and the refractive index of the dielectric. A number of ways can be used to tune their visible color, including changing the refractive index of the medium or controlling the distance, *d*, between the two reflective mirrors. The use of stimuli-responsive polymers as a dielectric material is one of the many ways used to tune and control the distance between the two reflective mirrors.

The Serpe Group has developed etalon devices by sandwiching poly (*N*-isopropylacrylamide) (pNIPAm)-based microgels between two thin, reflective Au layers that act similar to Fabry-Pérot interferometers.[78] PNIPAm-based microgels are thermoresponsive, colloidally stable hydrogel microparticles.[58, 102] Specifically, pNIPAm microgels experience a volume phase transition at 32 °C in water, commonly referred as the lower critical solution temperature (LCST). Below the LCST, the crosslinked polymer chains are highly solvated and swollen. Above the LCST, the microgels collapse, expelling their water of solvation that results in a decrease in their diameter. This process is highly reversible over many cycles, so they reswell when the $T < LCST$. Furthermore, pNIPAm microgels can be chemically modified with other comonomers to provide additional responsivity.[103-106] One of the most common comonomer used is acrylic acid (AAc) that can render pNIPAm-based microgels pH responsive due to the ionization of the carboxylic acid groups.[77, 107] AAc has a pK_a of 4.25, so when pNIPAm-*co*-AAc microgels are in a medium where the pH is higher than its pK_a, the carboxylic groups are deprotonated, causing the microgels to swell as a result of charge-charge repulsion. However, the microgels shrink when the pH of the medium decreases $< pK_a$ due to the lack of charge-charge repulsion from the neutralized AAc groups. From these microgels, etalons were fabricated using the "paint-on" method.[108] The "paint on" method consists of a concentrated microgel solution (achieved via centrifugation of a dilute microgel solution) being continuously spread on a Au-coated glass substrate (typically 15 nm Au) using the side of a micro pipette tip while the microgel solution dries. After the microgel solution cannot be spread any further on the surface, the microgel layer is allowed to dry for 2 h after which the excess microgels are removed by extensively rinsing the substrate with DI water. Following overnight incubation in DI water, the samples are rinsed again with DI water, dried with N_2 gas and a second Au layer (usually 15 nm of Au, but can be 5-30 nm) is finally deposited on top of the microgel layer, obtaining the etalon structure. The structure of the device is shown in **Figure 2.1(b)**. The resulting etalons show characteristic peaks in the visible range as shown in **Figure 2.2(c)**, which are modulated by the microgel size. For instance, based on Equation 2.1 described above, the peaks in the reflectance spectra are expected to shift to higher wavelengths (red shift) when the microgel layer swells (e.g., when pNIPAm-*co*-AAc microgels are exposed to solutions with pH > pKa of the AAc), while the reflectance peaks are expected to shift to lower wavelengths (blue shift) when the microgel layer shrinks (e.g., when pNIPAm-*co*-AAc microgels are exposed to solutions with pH < pKa of the AAc). Similarly, varying the solution temperature above/below the microgels' LCST can lead to blue/red shifts in the reflectance peaks, respectively.

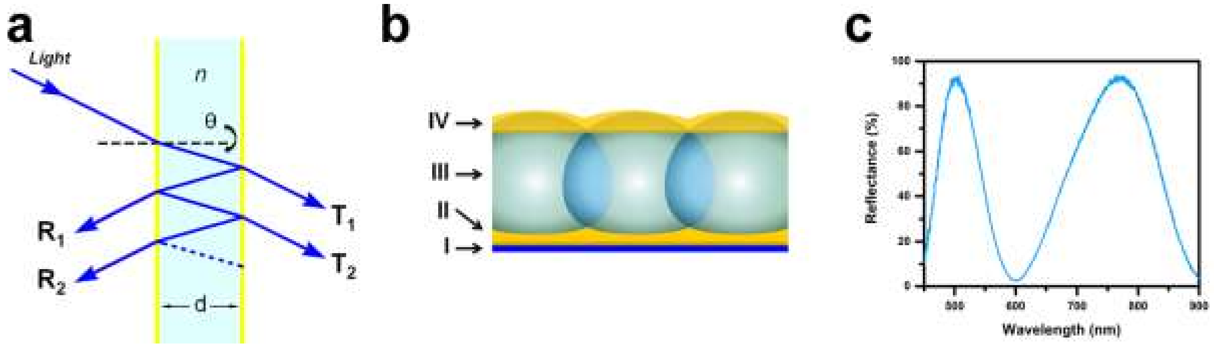

Figure 2.1 (a) Schematic illustration of a typical Fabry-Pérot etalon composed of two reflective mirrors (vertical yellow lines) separated by a dielectric material with refractive index $\boldsymbol{\eta}$ and thickness of d. Incident light (blue arrows) striking the etalon at an angle $\boldsymbol{\theta}$ enter its cavity and undergo multiple internal reflection where constructive and destructive interferences occurs in the transmitted (T1 and T2) or reflected (R1 and R2) waves. (b) Structure of the microgel based etalon device composed of two reflective Au layers (II and IV) separated by a microgel layer (III) and constructed on a glass substrate (I). (c) Representative spectra for an etalon composed of pNIPAm-*co*-AAc microgels.

The Serpe Group has conducted extensive studies on microgel-based etalons and demonstrated in a number of publications their universality for sensing, biosensing, and controlled/triggered drug delivery applications via simple modification of the chemistry of the microgels or the properties of the Au layers.[79-80, 109-112] While the etalon fabrication process is simple and straightforward, it is time consuming as each microgel layer has to be painted individually, one at a time. Furthermore, their optical properties (i.e., color purity and homogeneity) are highly dependent on the expertise and skills of the individual doing the painting. In this chapter, I outline a new method based on doctor blade technique to obtain highly packed microgel layers with minimal defects, resulting in etalon devices of high color purity and uniformity, which is essential for using them as portable sensors where we will be using inexpensive camera components to obtain images to determine RGB values. Doctor blading is a well-established technique widely used in printing, coating processes, textile, paper making, and photographic film to produce highly uniform flat films on large surface areas.[113-116] The name is thought to be originated from the blades used in the equipment for flatbed letterpress printing, where it was first called a “ductor blade”, meaning to draw across surface. The blades were used to control the amount of ink being deposited on the ductor rolls (printing cylinders) by wiping the excess ink from the ductor rolls surface while the ductor rolls rotate in an ink supply. The word ductor later became doctor. Doctor blade technique has been used by Jiang and coworkers to fabricate in large scale highly ordered colloidal crystal-polymer nanocomposites.[117] Here, we utilize doctor blade technique to spread the microgel solution evenly across the surface of the substrates, eliminating the variability of the painting process from person to person as everyone does it slightly different. Moreover, we have developed a painting platform that can fabricate over 1000 etalon devices in a single fabrication process, which is extremely important for their future commercialization. The optical quality and visual color purity of the etalons prepared by both methods were compared using their reflectance spectra and the distribution of their RGB values. Furthermore, the uniformity of the microgel films was characterized by ellipsometry. The microgel films prepared using the doctor blade technique proved to be more uniform and consistent from etalon to etalon and had higher microgel packing density. In addition, the etalons that resulted from the microgel layers deposited using the doctor blade technique were highly reproducible from batch to batch as demonstrated by their low standard deviations. We also investigated how the conditions of the microgel synthesis (temperature and batch size) impacted the optical properties of the resultant etalons. We found that microgels synthesized at higher temperature (75 ^{o}C) yielded smaller microgels size than when synthesized at lower temperature (70 ^{o}C) which resulted in etalons with different reflectance spectra but similar color (visually). Furthermore, microgels prepared in large scale also showed smaller sizes, resulting in etalons with reflectance spectra blue shifted and different colors. In addition, microgels synthesized twice following the same procedure showed different sizes, resulting in etalons with different reflectance spectra but similar colors (visually), implying that small variability in the microgel size does not impact their visual color but the small variations in the microgel film thickness can be observed in their reflectance spectra. Finally, we showed that the quality of the etalons fabricated by different individuals were not significantly different in terms of the position of the reflectance peaks and RGB values obtained from photographs.

2.2 Experimental Section

2.2.1 Materials

The monomer *N*-isopropylacrylamide (NIPAm) was obtained from TCI (Portland, Oregon) and purified by re-crystallization from hexane (ACS reagent grade, EMD, Gibbstown, NJ) prior to use. *N,N'*-methylenebisacrylamide (BIS), acrylic acid (AAc), methacrylic acid (MAAc), 3-Butenoic acid (VAAc), ammonium persulfate (APS), sodium hydroxide (NaOH), sodium chloride (NaCl), and phosphate buffered saline (PBS) pH 7.4 were purchased from Sigma-Aldrich (Oakville, Ontario) and used as received. Cover glasses (25 x 25 x 0.15 mm) and calcium chloride ($CaCl_2$) were obtained from Fisher (Ottawa, Ontario). Hydrochloric acid (HCl) was obtained from Caledon Lab. (Georgetown, Ontario). A pH meter (JENCO 6173, San Diego, CA) coupled with ROSS micro pH electrode (Thermo Scientific, Markham, ON) was used to prepare solutions of pH 4 and 7.8. Cr and Au, both 99.999%, were obtained from ESPI Company and MRCS Canada (Edmonton, AB), respectively. Whatman #1 paper filters were obtained from GE Healthcare (U.K.) and deionized (DI) water with resistivity of 18.2 MΩ·cm was obtained from a Millipore Milli-Q-Plus system (Billerica, MA).

2.2.2 Painting Platform Fabrication

The custom-built platform for doctor blade was fabricated in house from aluminum. The platform contains 16 square substrate holders as shown in **Figure 2.2**. The platform has a total length, width and height of 145 mm, 145 mm, and 60 mm respectively, where 16 squares of 26 mm length, 26 mm width and 0.3 mm height were created to form the substrate holders. As the height of the substrate holder is 0.3 mm and the thickness of the glass substrate is around 0.15 mm, it leaves a space of 0.15 mm to be filled with the microgel solution. The spacing between each substrate holder is 60 mm and 130 mm away from the edges. Apertures with round shape of 190 mm in diameter were created in the center of each substrate holder for easy removal of the glass substrates from the platform after the painting process. In addition, each substrate holder is connected to a vacuum chamber to hold the glass substrate flat and prevent it from moving during the painting process.

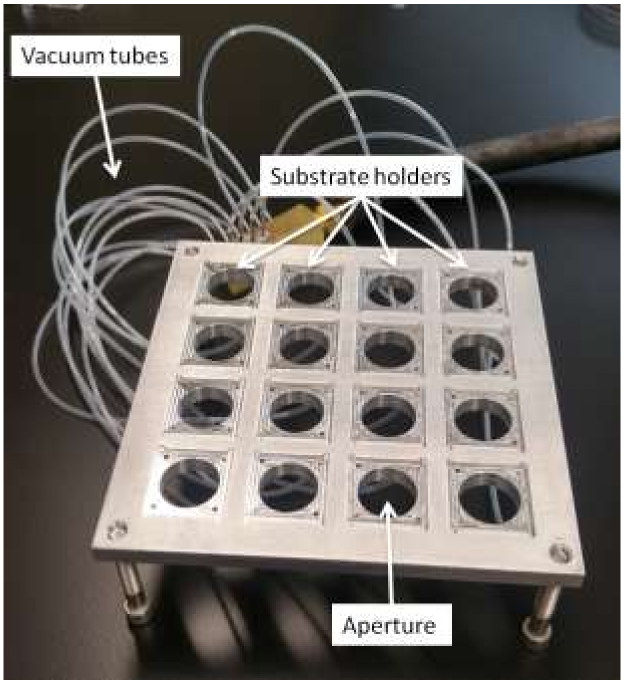

Figure 2.2 Photograph of the painting platform used to form homogenous microgel films onto Au coated glass substrates.

2.2.3 Synthesis of pNIPAm-Based Microgels

Microgels were synthesized by surfactant free, free radical precipitation polymerization as described previously.[79, 118-119] In our synthesis, the monomer NIPAm (11.9 mmol) and the crosslinker BIS (0.703 mmol) were dissolved in 99 mL of DI water in a 250 mL beaker. The mixture was stirred for 30 minutes after which it was filtered through a 0.2 μm filter that was attached to a 10 mL syringe which led into a 250 mL 3-necked round bottom flask to remove any particulate matter. The round bottom flask was fitted with a reflux condenser, thermometer, and N_2 gas inlet (needle). The solution was then stirred at 400 rpm and bubbled with N_2 gas while increasing the temperature to 70 ^{o}C over 1 h, after which the comonomer AAc (1.43 mmol) was added to the reaction mixture in one aliquot. Following the addition of the initiator APS (0.2 mmol) dissolved in 1 mL of DI water, the polymerization reaction was carried out at 70 ^{o}C for 4 h under N_2 atmosphere. The suspension was then allowed to cool down overnight under stirring and then filtered through glass wool to eliminate large aggregates. The suspension was again filtered through a Whatman #1 filter paper and distributed into 50 mL centrifuge tubes for purification. The suspension was centrifuged at ~10 000 rpm for 1 h to form a pellet and the supernatant was replaced with DI water. The pellet was resuspended by vortexing and centrifuged again. This process was repeated 6 times to remove any unreacted species and linear polymer from the microgels. In the last centrifugation step, the supernatant was removed and a concentrated solution of pNIPAm-*co*-10%AAc microgel was obtained. The synthesis of pNIPAm-*co*-10%AAc microgels was carried out twice at 75 ^{o}C following the same procedure described above and they are referred as pNIPAm-*co*-10%AAc-75A and pNIPAm-*co*-10AAc-75B. Furthermore, pNIPAm-*co*-10%AAc microgel synthesis was also carried out in larger scale at 75 ^{o}C. For instance, the volumes and moles were increased by 5 times and the reaction stirring rate to 700 rpm. This microgel is referred to as pNIPAm-*co*-10%AAc-75C. All the following microgels were also synthesized in larger scales but at 70 ^{o}C and stirring rate of 700 rpm. For pNIPAm-*co*-10%VAAc microgels, the AAc monomer was replaced by VAAc in the procedure above. For pNIPAm-BIS microgels, no comonomer was added and the procedure above was followed but this time skipping the comonomer addition step. For pNIPAm-*co*-5%MAAc microgels, the mols of monomers were changed to 63.148 mmol for NIPAm (90%), 3.508 mmol for BIS (5%), 3.508 mmol for MAAc (5%), and 1 mmol for APS. Finally, the viscosity of the microgel solution was further adjusted so that all types of microgels had similar concentrations. For this, 100 μL of the microgel solution was deposited onto a microscope glass slide as a single droplet. The microscope slide was quickly positioned vertically at 130^o as shown in **Figure 2.3** and the distance that it was dislocated in 1 min was recorded. DI water was added or removed by centrifugation until the microgel solutions reached 0.15 to 0.3 inches in 1 min. Before each measurement, the microgel solution was vortexed to ensure homogeneity and centrifuged in low speed for 5 min to remove bubbles formed when vortexing. This process was repeated 3 times for each microgel solution.

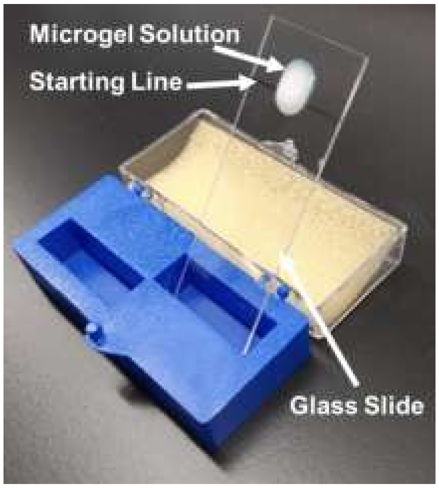

Figure 2.3 Photograph of the experimental procedure for adjusting the viscosity of the microgel solution.

2.2.4 Etalon Fabrication

2.2.4.1 Paint-on Technique

Etalons were fabricated following the paint-on technique found in ref.[108]. In our fabrication, 625 mm^2 cover glasses (0.15 mm thickness) were washed using ethanol/DI water and dried over a stream of N_2 gas. Following, 2 nm Cr (used as adhesion layer) and 15 nm Au were deposited onto the cover glasses using a thermal evaporator system (Torr International Inc., New Windsor, NY) at a rate of 0.19 Å s^{-1} and 0.17 Å s^{-1} respectively. The Au coated glass substrates were placed onto a hot plate set at 35 °C where an aliquot of 40 µL of the desired concentrated microgel solution was deposited and spread using the side of a micropipette tip until the glass substrate was fully covered being mindful not to scratch the surface. The microgel film was allowed to air-dry for 2 h, after which any excess of microgel was washed away by rinsing the glass substrate with copious amount DI water. Next, the glass substrates were incubated in DI water overnight and rinsed again with DI water then dried over a stream of N_2 gas before a second layer of 2 nm Cr/15 nm Au (or 5 nm Au when mentioned) was deposited, yielding 625 mm^2 etalon optical devices. Furthermore, etalon devices of different sizes were prepared in the cover glasses (625 mm^2) using a metal mask that was placed in front of the cover glasses before each Cr/Au deposition.

2.2.4.2 Doctor Blade Technique

Cover glasses (25 x 25 x 0.15 mm) were washed by placing them into a container containing a mixture of 1:1 ethanol/DI water and sonicating for 10 min using a ultrasonic cleaner (Fisher Scientific, FS20). The cover glasses were then transferred to another container containing DI water and sonicated again for another 10 min, after which they were removed from the container and dried with N_2 gas. Following this, the clean cover glasses were coated with 2 nm Cr/15 nm Au as described above. The Cr/Au coated glass substrates (16 in total) were placed in each substrate holder of the fabricated painting platform with the coated side facing upwards. Vacuum was then applied to hold the glass substrates flat in place. On the left side of each substrate holder, 200 µL of the desired microgel solution was used to draw a straight line with a length larger than 26 mm using a micropipette as showing in **Scheme 2.1**, removing any bubbles that formed during this process. With the assistance of a microscope glass slide (25 x 75 x 1 mm), the microgel solution was dragged from left to right along the surface of the painting platform, filling the gap of 0.15 mm for the first two rows and then for last two rows. It is important to point out that the microscope slide was not forced against the surface of the platform, it was lightly dragged using only the weight of the slide to avoid scratching the surface and contaminating the microgel solution. After forming the microgel films, the glass substrates were removed from the platform and transferred to a hot plate set at 35 ^{o}C where they were allowed to air-dry for 1 h. After the drying process, the excess microgel was washed away by extensively rinsing the glass substrates with DI water until no traces of the gel could be seen. Following, the glass substrates were placed into a Petri dish containing DI water and incubated overnight at room temperature to remove any microgel that was not directly attached to the gold surface. After the overnight water bath, the glass substrates were rinsed again with DI water and dried with N_2 gas before a second layer of Cr/Au was deposited. Again, etalon devices of different sizes were also fabricated using a metal mask that was placed in front of the glass substrates (625 mm^2) before Cr/Au deposition. Moreover, the thickness of the second Au layer deposited was either 5 nm or 15 nm to demonstrate that the thickness of the top Au layer has minimal effect on the quality of the etalon. Furthermore, the choice of the Au layer thickness depends on the application. For instance, 5 nm top Au layer yield etalons with faster responses than 15 nm. However, thicker top Au layer is preferred when conducting chemical modifications on the top Au layer. It is important to note that the deposition rate for Cr an Au was kept constant for all depositions to obtain reproducible films as the gold film quality varies with its thickness and deposition rate.[120]

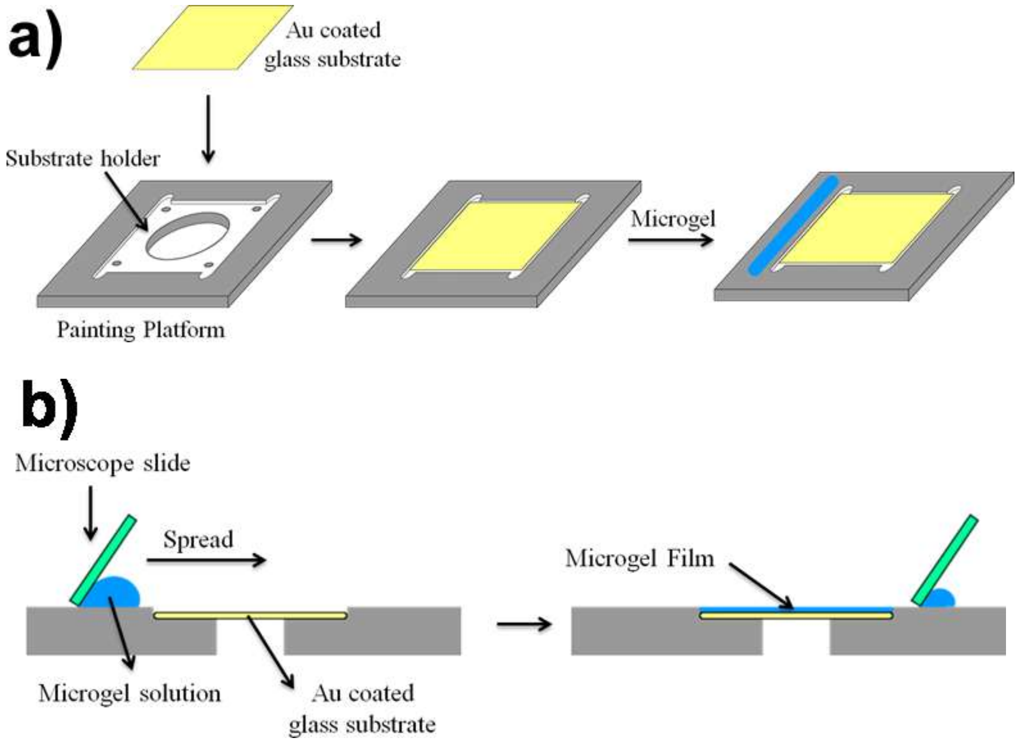

Scheme 2.1 Schematic illustration of the painting process for a single glass substrate using the fabricated painting platform. (a) The Au coated glass substrate is placed in the substrate holder and vacuum is applied. A micropipette is used to draw a straight line using 200 µL of the concentrated microgel solution beside the substrate holder. (b) A microscope glass slide is used to drag the microgel solution across the platform surface, filling the space between the glass substrate and the surface of the platform, yielding a homogeneous microgel film.

2.2.4.3 Method Validation Using Doctor Blade Technique

The etalon fabrication method using the doctor blade technique was tested for optical quality based on reflectance spectra, visual color purity and uniformity based on their RGB value distribution obtained from photographs. We also investigated how these properties depended on the individual that was generating the devices. To do this, two individuals that had minimal to no experience with the etalon fabrication process were shown how to conduct the painting process once and were then provided with a written protocol the following day for them to attempt the fabrication. They were given 3 glass substrates that had 64, 4 mm^2 Au squares patterned, and a pre-concentrated solution of pNIPAm-*co*-10%AAcB75 microgel. The students were asked to paint the Au patterned substrates using the microgel solution following the protocol provided. The students returned the substrates, now coated with a microgel layer, and a second 2 nm Cr/5 nm Au layer was deposited. The resultant etalon arrays were incubated in DI water overnight before reflectance spectra and pictures were collected. Moreover, etalon arrays were fabricated from the same microgel reaction batch (pNIPAm-*co*-10%AAc) on two different days to investigate their day-to-day variability.

2.2.5 Characterization and Measurements

2.2.5.1 Dynamic Light Scattering (DLS) Measurements

The hydrodynamic diameter of the microgels in DI water was measured using a commercial Zetasizer Nano ZS – Malvern Instrument (Westborough, MA, USA) equipped with a 633 nm light source at 25 °C and the results can be found in **Table 2.1**. The reported value is an average of 3 measurements where each measurement had 13-15 scans with an acquisition time of 4-5 seconds. The light scattering intensity was detected at 173°.

Table 2.1 Hydrodynamic Diameter and Standard Deviations for the Investigated Microgels

Microgel	**Hydrodynamic Diameter, D_H (nm)**
pNIPAm-*co*-10%AAc	1251 ± 36
pNIPAm-*co*-10%AAc-75A	1089 ± 35
pNIPAm-*co*-10%AAc-75B	958 ± 30
pNIPAm-*co*-10%AAc-75C	868 ± 10
pNIPAm-*co*-10%VAAc	853 ± 9
pNIPAm-*co*-5%MAAc	643 ± 6
pNIPAm-BIS	674 ± 11

2.2.5.3 Ellipsometric Measurements

Ellipsometric measurements were performed in air on the dry microgel films after soaking them overnight in water, after final water rinsing and before the second Au layer was deposited using an imaging ellipsometer EP3-SE (Nanofilm, Accution GmbH, Germany) at wavelength ranging from 380 to 750 nm and using nulling four zone mode at 42°. The thickness measurements were done on microgel films coated on 4 mm^2 and 625 mm^2 Au substrates. For 4 mm^2, 16 measurements were done in 1 sensor array in the center of each square across the array. Each measurement was an average of 3 spots as shown in **Figure 2.10**. For the 625 mm^2, 8 measurements were done around the region where the reflectance spectra were collected. Again, each measurement was an average of 3 spots. EP4Model software (Nanofilm, Germany) was used to perform the optical modeling and the thickness calculation. Cauchy dispersion model was used to predict the thickness of the polymer layer and an effective medium approximation (EMA) with 50%/50% mixture between the polymer optical constants and those of air was used for the surface roughness.

2.2.5.4 Reflectance Measurements and Spectrum Analysis

Reflectance measurements in different locations of the etalons (625 mm^2) were conducted using a reflectance probe from Ocean Optics (Dunedin, FL) coupled with a LS-1 tungsten light source (spectral range of 360 to 20000 nm), and a Red Tide USB650 spectrometer (detection range of 360 to 1100 nm). Prior the measurements, the etalons were incubated overnight in a Petri dish containing pH 4, 300 ppm $CaCl_2$ solution. The probe was inserted into the solution and its height was adjusted so the illuminated spot had a diameter of 3 mm. In addition, the angle of the probe with respect to the etalon was kept at 90° to ensure that all reflectance spectra were recorded at the same incident angle. The reflectance spectra were recorded using Ocean Optics Spectra Suite Spectroscopy Software over a range of 400 to 900 nm. At least 7 spectra for each etalon device of 625 mm^2 at different locations were recorded. For etalon arrays, a spectrum was recorded for each etalon in pH 4 and pH 7 solutions, both containing 300 ppm $CaCl_2$ to investigate the effect of the two painting techniques on their pH responsivity. The reflectance spectra were collected in DI water for the method validation experiments.

For etalon size response-dependence experiments, etalons composed of pNIPAm-*co*-10%AAc microgels, top Au layer thickness of 15 nm, prepared with different sizes ranging from 625 mm^2 to 4 mm^2, were incubated in PBS buffer pH 7.4 prior to being exposed to an NaCl solutions of increasing concentration, which was prepared using PBS buffer as a blank. The etalons were fixed in a Petri dish where 600 μL of PBS buffer was transferred to the center of the device. The reflectance probe was inserted into the solution and the reflectance spectrum was recorded after 20 min of stabilization. Then, various amounts of 1 M NaCl solution in PBS buffer (38.4, 47.7, 114.2, 160 and 240 μL) was successively added to the 600 μL of PBS buffer solution using a micropipette.

The reflectance spectra for the pH and NaCl response experiments were analysed by choosing a peak to be monitored and fitting it into a Gaussian to obtain an objective measure of the peak position.

2.2.5.5 Picture Acquisition and Color Analysis

Photographs of the etalons in different pH solutions were acquired using a custom-built 3D printed white box, referred as 3D printed box #1, as shown in **Figure 2.3**. It was coupled with a raspberry pi, raspberry pi camera, diffuser, and white light-emitting diodes (LEDs). The camera was fixed at an angle of 10^o relative to the etalon arrays, and the distance from the camera to the sensors was ~7 cm. Here, the etalons in a Petri dish containing the desired pH solution was placed inside the box and the box was closed. Following, a picture was acquired using the raspberry pi system for each etalon device. For the method validation experiments, photographs of the etalon arrays were taken using a cell phone camera (LG 4), a mini studio box coupled with white LEDs, and a tripod. The photographs were taken in the lab bench where the angle of the cell phone to the bench was kept at 10^{o} and the distance from the cell phone to the etalon array was kept at ~20 cm. The color of the etalons (4 mm^2) were further characterized by cropping the images, removing the background and edges, and extracting the RGB values from an area of 68 x 68 pixels using MATLAB software (R2018b).

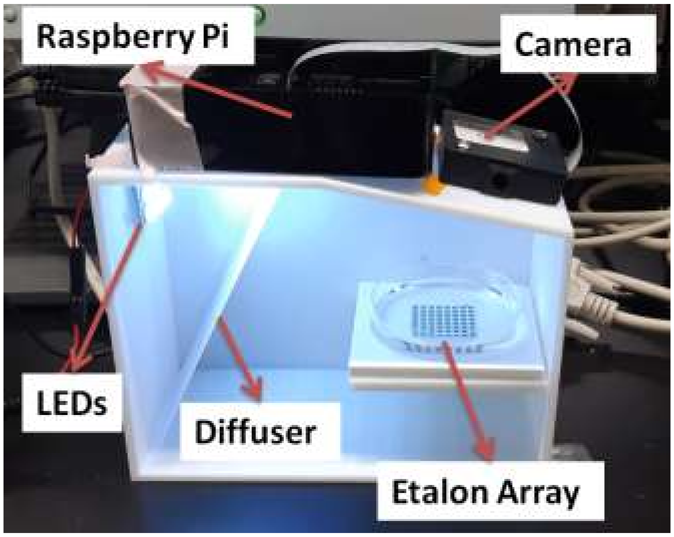

Figure 2.4 Photograph showing the costume-built 3D printed white box #1 and set up used to take pictures of the etalon devices at different pH values. The camera is angled at 10^{o} relative to the sensor array surface.

2.3 Results and Discussion

pH and temperature-responsive pNIPAm-*co*-AAc microgels were synthesized in different reaction conditions. These reactions are known to produce highly dispersed and porous, spherical microgels and it was confirmed by visualizing them under an optical microscope. **Table 2.1** shows their hydrodynamic diameter in DI water measured by DLS. Specifically, pNIPAm-*co*-10%AAc microgels were synthesized at a different reaction temperatures and batch volume to investigate how fluctuations in temperature and reaction scale impacts the microgel size and the reproducibility of the fabricated etalons. In addition, for industrial purposes and large scale production of the etalon devices, a large amount of microgel solution is needed. Thus, a reaction volume of 100 mL is not feasible as it yields only ~ 5 mL of the concentrated microgel solution. We increased the reaction volume by 5x and evaluated how this affected the microgel size, which in turn could impact the color of the resulting etalons devices. **Figure 2.4** shows TEM images of the dried microgels prepared in small scale at 70 ^{o}C, 75 ^{o}C, and large scale at 75 ^{o}C and their average size, calculated using ImageJ software from the measurement of at least 150 microgels, were 534 ± 17 nm, 511 ± 36, and 513 ± 22, respectively. Microgels prepared at 70 ^{o}C were larger than those prepared at 75 ^{o}C, presumably due to the higher temperature causing the microgels to collapse earlier in the synthesis, and leading to more nuclei that can grow into smaller microgels. In addition, microgels prepared at a different reaction scale (same temperature) showed similar sizes, suggesting that the temperature is a more important factor affecting the microgel size rather than the reaction scale. However, as can be seen from the DLS measurements, the size of the pNIPAm-*co*-10%AAc microgels synthesized in a larger reaction scale showed to be significantly smaller (868 ± 10 nm) than those synthesized in a smaller reaction scale (1089 ± 35 nm and 958 ± 30 nm). Pelton and coworkers also observed that increasing the reaction scale result in microgel with smaller diameters.[69] The authors prepared microgels in a total reaction volume of 0.5 and 4 liters which gave microgels with average diameters of 402 and 308 nm respectively. Based on these results, we decided to keep the synthesis of pNIPAm-*co*-10%VAAc, pNIPAm-*co*-5%MAAc, and pNIPAm-BIS at larger scale and 70 °C reaction temperature.

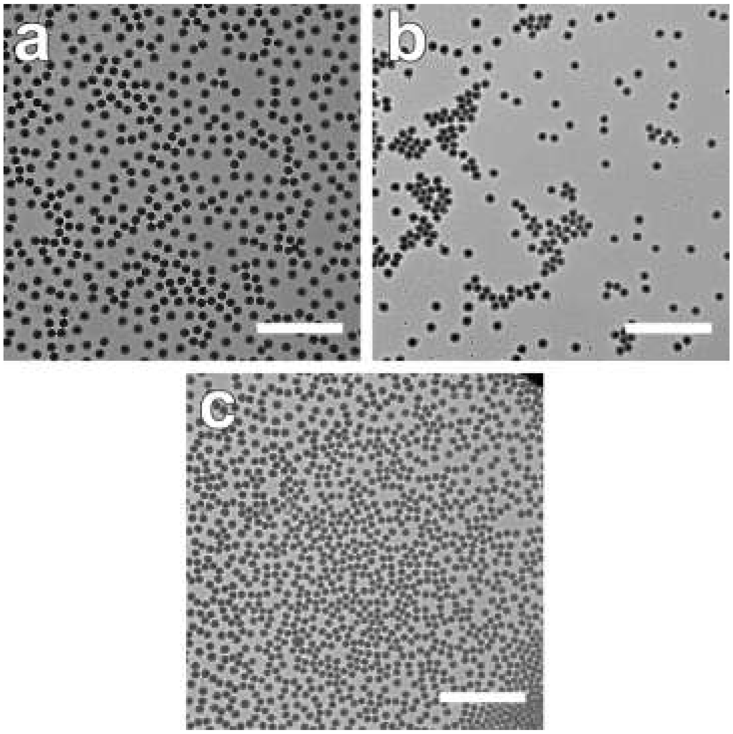

Figure 2.5 TEM images of (a) pNIPAm-*co*-10%AAc, (b) pNIPAm-*co*-10%AAc-75B, and (c) pNIPAm-*co*-10%AAc-75C microgels, scale bars are 5 μm in each image.

From these microgels, etalon devices were fabricated using the "paint-on" and doctor blade technique to evaluate their ability to produce homogeneous microgel films and pure colored devices. **Figure 2.5** shows photographs and reflectance spectra for 4 different etalon devices of 625 mm^2 constructed using the "paint-on" technique at different pH values. Details of the paint-on technique can be found in the experimental section. Briefly, a small aliquot of the concentrated microgel solution was spread over the surface of a Au coated glass substrate using the side of a micropipette tip. The excess microgel was removed by continuously washing the glass substrates with DI water, overnight incubation in DI water, and a final water rinsing step.

Following, the substrates were dried with N_2 gas and a second Au layer was deposited to yield the etalon structure. The resulting etalons were incubated overnight in the desired pH solution to ensure stability and that any color heterogeneity comes from the thickness variation of the microgel film across the device rather than some regions reaching an equilibrium state faster than other regions. As can be seen in **Figure 2.5(a-d)**, the pH responsive etalons prepared with pNIPAm-*co*-5%MAAc, pNIPAm-*co*-10%AAc75C,and pNIPAm-*co*-10%VAAc microgels showed different colors at high and low pH. This is attributed to the protonation and deprotonation of the carboxylic groups present in the microgels. At high pH values, the carboxylic groups are deprotonated and, as a result of the charge-charge repulsion, the microgel layer swell, changing the distance between the two Au layers and resulting in a color change. As expected, the etalon constructed from pNIPAm-BIS microgels showed no color change at the different pHs as they do not contain weak acid groups. Furthermore, the uniformity of the color for these etalons was very poor, which is a result of variations in the packing density of the microgels presumably caused by the way the microgel was spread on the surface. The color purity of the etalon devices is highly dependent on the quality of the microgel layer acting as a dielectric layer between the two Au layers. **Figure 2.5(e-h)** shows spectra collected from different regions of the devices that were incubated overnight in pH 4, 300 ppm $CaCl_2$ solution and the insets show the corresponding location where the spectra were recorded. As can be seen, the spectrum significantly varies from location to location, which can compromise the usability of these devices for sensing application. It has been shown that a highly concentrated microgel solution and the drying process are critical to obtaining jammed microgel films and overcome the "coffee-ring effect".[108] However, the procedure by which the microgel solution is spread on the substrate surface and the microgel concentration are also crucial to obtain a highly packed microgel layer with minimal defects. To visualise this, we can assume the glass substrate is a blank canvas, the microgel as paint, and the pipette tip as a brush. As the brush spreads the paint on the surface of the blank canvas, traces are left behind that correspond to the locations where the brush was passed on the canvas. In addition, every time the microgel solution is spread on the substrate surface, it is spread at a different concentration as the microgel solution is continuously drying, becoming viscous and yielding films with different packing densities. Moreover, it is fairly easy to scratch the surface with the pipette tip and the procedure is time consuming as the substrates have to be painted one at a time, which makes this approach not ideal for large scale fabrication. Thus, from a practical point of view, the paint-on technique used to fabricate the etalon devices is not ideal and the quality of the devices is highly dependent on the individual's expertise.

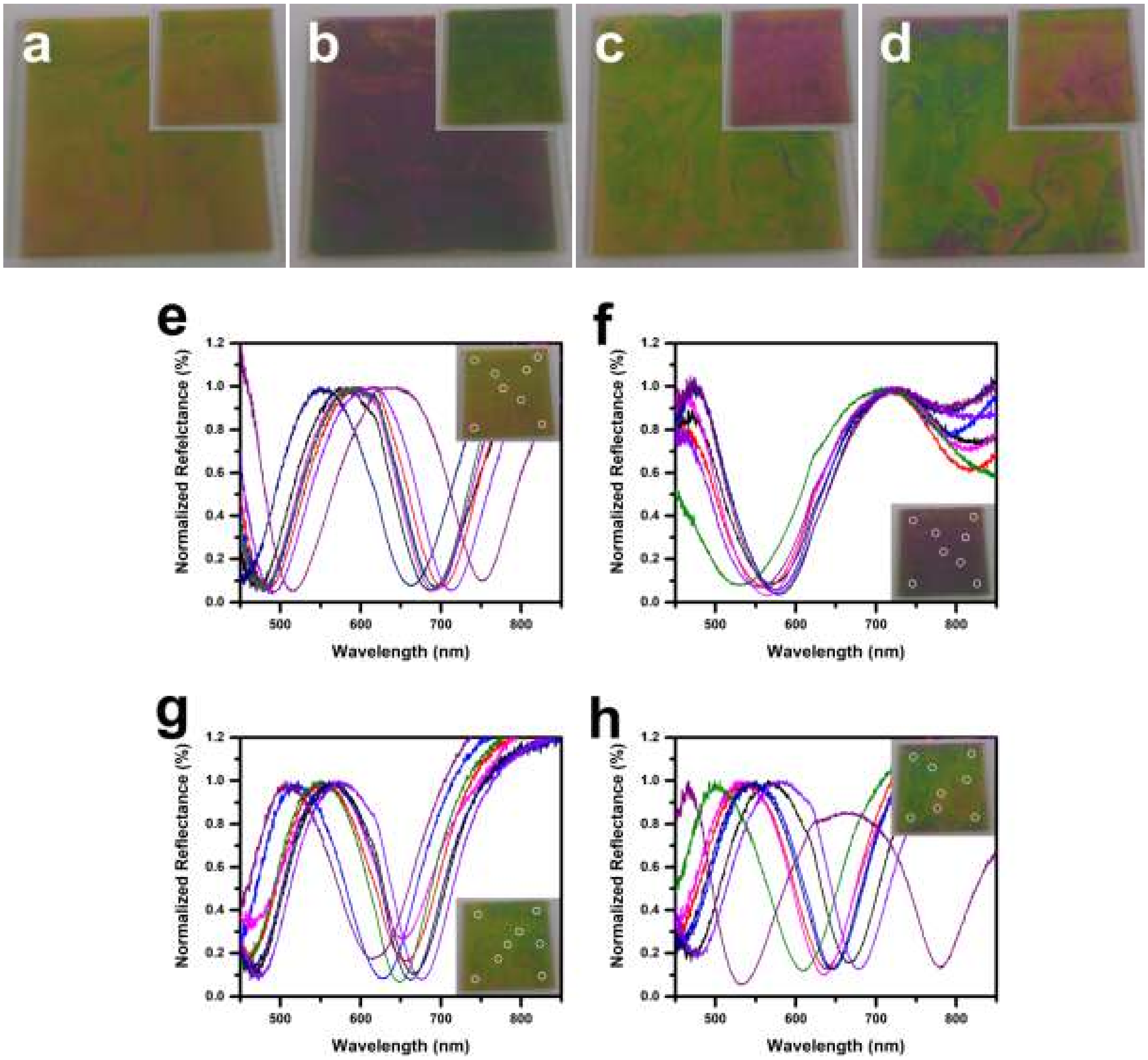

Figure 2.6 Photographs showing etalon devices made from (a) pNIPAm-BIS, (b) pNIPAm-*co*-5%MAAc, (c) pNIPAm-*co*-10%AAc75C, and (d) pNIPAm-*co*-10%VAAc microgels fabricated using the "paint-on" technique obtained in pH 4, 300 ppm $CaCl_2$ and pH 7.8, 300 ppm $CaCl_2$ solutions (insets). (e-h) Reflectance spetra for the corresponding etalon devices obtained in pH 4, 300 ppm $CaCl_2$ collected from 8 different regions (insets).

To address these issues, we developed a painting platform that uses doctor blade technique to spread the microgel solution evenly and can paint many substrates of 625 mm^2 (16 in total) at the same time. Details of the painting procedure are described in the experimental section and shown in **Scheme 2.1**. Briefly, Au coated glass substrates were placed in each substrate holder and the microgel solution of fixed concentration was spread with the assistance of a microscope glass slide. After forming the microgel film, the Au coated glass substrates were transferred to a hot plate set at 35 ^{o}C and allowed to dry in air for 1 h. Then, the excess microgels were removed by extensively rinsing the substrates with DI water and incubating overnight in DI water. Incubating the films in DI water overnight increases the quality of the resultant microgel layer by possibly breaking up multiple microgel layers and removing them from the microgel layer that is directly attached to the Au, leaving only a highly packed microgel monolayer that is directly bound to the Au surface. Finally, a second Au layer was deposited to obtain the etalon structure. The top Au layer had a thickness of 15 nm for all the etalons except for the etalon composed of pNIPAm-*co*-10%AAc-75C microgels, which was 5 nm. In this case, 5 nm was used to demonstrate that the thickness of the top Au layer does not influence the quality (color uniformity) of the etalons. **Figure 2.6** show photographs of the resulting etalon devices at different pH values and their corresponding reflectance spectra collected from 7 different regions. As shown, the etalons prepared by the doctor blade method are more uniform in color than etalons made using the paint-on method, which is a direct result of the increased microgel layer quality. Moreover, the reflectance spectra collected from different regions on the corresponding etalon devices show minimal variation compared with the paint-on method, demonstrating that these films have similar packing densities. Furthermore, decreasing the thickness of the top Au layer to 5 nm had no significant effect on their quality. Still, these etalon devices also showed some color variation, presumably due to their large surface area.

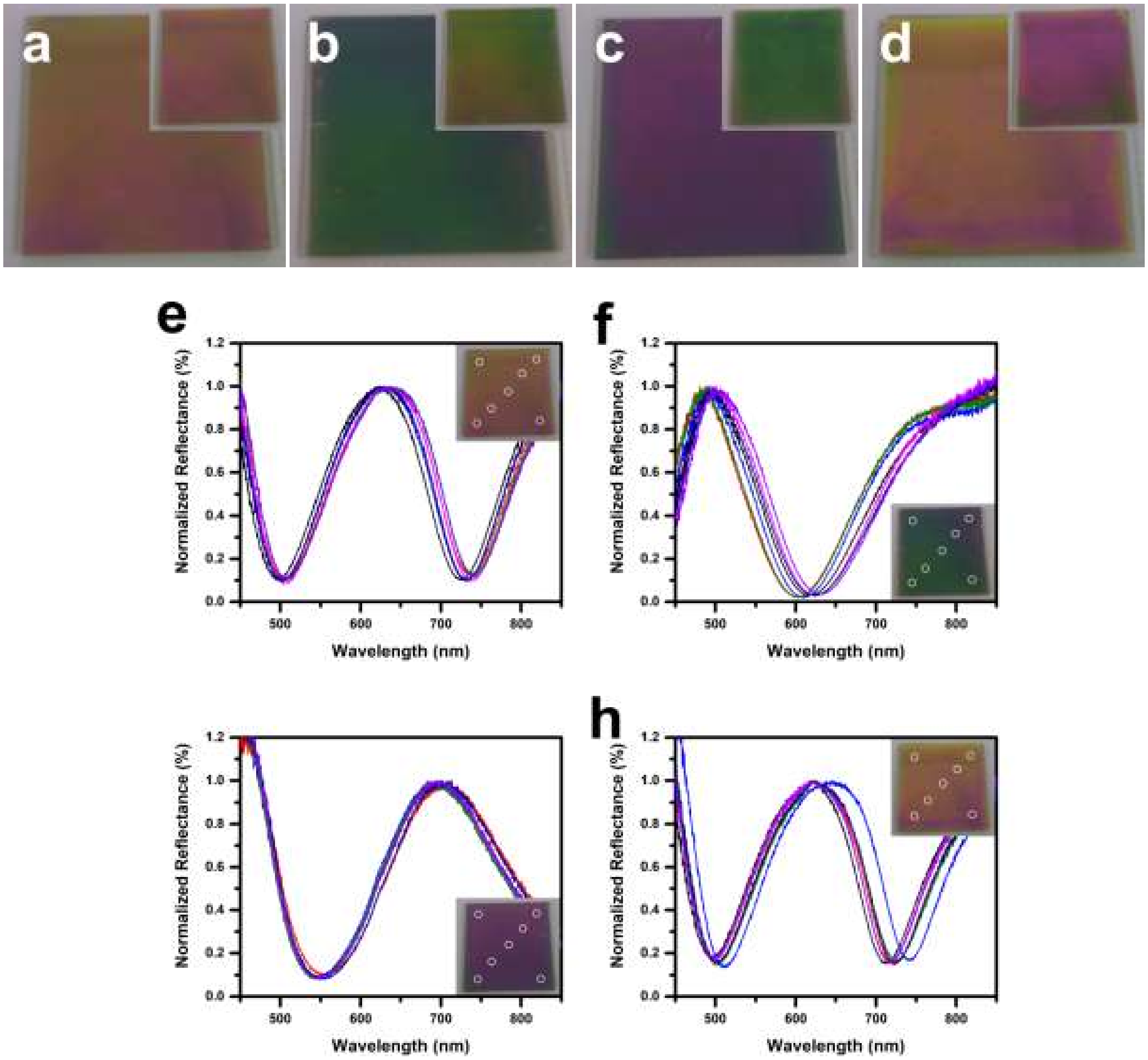

Figure 2.7 Photographs showing etalon devices made from (a) pNIPAm-BIS, (b) pNIPAm-*co*-5%MAAc, (c) pNIPAm-*co*-10%AAc75C, and (d) pNIPAm-*co*-10%VAAc microgels fabricated using the doctor blade technique obtained in pH 4, 300 ppm $CaCl_2$ and pH 7.8, 300 ppm $CaCl_2$ solutions (insets). (e-h) Reflectance spetra for the corresponding etalon devices obtained in pH 4, 300 ppm $CaCl_2$ collected from 7 different regions (insets).

To obtain etalon devices with higher color purity, we further decreased its size to 4 mm^2. We hypothesized that the probability of forming defects on the microgel layer decreases as the surface area decreases. Furthermore, 1,024 etalon devices could be made in a single fabrication process, which is extremely important for high production and commercialization of the devices. Here, 64 etalon devices composed of pNIPAm-*co*-10%AAc microgels were constructed on a 625 mm^2 cover glass using a metal mask as showing in **Figure 2.7**. The etalons had a top Au layer thickness of 5 nm and were incubated in DI water. As shown, these etalons are of high color purity, uniformity and highly reproducible. To quantify the color purity of these etalon devices, we compared the RGB value distributions for etalons fabricated using both methods as shown in **Figure 2.8(a,b)**. As evident, the distributions of the R, G, and B values for etalons prepared by the doctor blade technique are less broad, with a shape that resembles a normal distribution, which is a result of their higher color purity and uniformity. On the contrary, the RGB distributions for etalons fabricated using the paint-on method is much broader due to the color heterogeneity presented on these devices (**Figure 2.8(c,d)**). In addition, doctor blade technique also yields etalons with higher spectral quality. **Figure 2.9** shows the average for 102 reflectance spectra collected from individual pNIPAm-*co*-10%AAc-75C microgel based etalons (4 mm^2) devices that were prepared by both methods and the shaded area on each spectrum corresponds to their standard deviation. As we can see, the shaded area in the spectrum for the etalons prepared using the paint-on method is much higher due to the poor thickness consistency from etalon to etalon while the shaded area is significantly smaller in the spectrum for etalons fabricated using the doctor blade technique, which demonstrates the reproducibility of the fabrication process. These results revealed that the microgel films prepared by the paint-on method not only vary in a single etalon, but also from etalon to etalon.

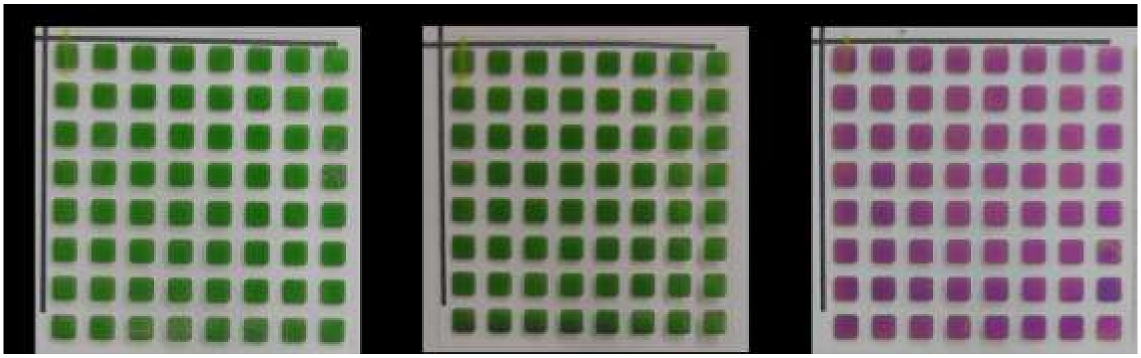

Figure 2.8 Photograph of 64 etalon devices fabricated on a 625 mm^2 glass substrate using doctor blade technique. Each green square corresponds to an individual etalon device. Etalons were constructed from (a) pNIPAm-*co*-10%AAc, (b) pNIPAm-*co*-10%AAc-75A, and (b) pNIPAm-*co*-10%AAc-75C microgels and the top Au layer had thickness of 5 nm. Etalons were incubated in DI water.

The uniformity of the microgel layer was further investigated by measuring their film thickness by ellipsometry before the second Au layer was deposited. Ellipsometric measurements were done on 8 different locations of a film composed of pNIPAm-*co*-10%AAc-75C microgels formed on 625 mm^2 Au coated substrates (etalons found in **Figure 2.5(c)** and **Figure 2.6(c)**). The thickness was measured on 3 spots of each location and the averages for the 8 measurements were 91 ± 6 and 96 ± 2 for films made by the paint-on and doctor blade method respectively. Furthermore, ellipsometric measurements were also performed on 16 microgel layers formed on 4 mm^2 Au coated glass substrates and their average thickness was 88 ± 8 and 103 ± 3 for films made by the paint-on and doctor blade method respectively. As noted, the standard deviation for films prepared based using the doctor blade technique is significantly lower than those prepared using the paint-on method. The precision of the film thickness was increased by 3x, indicating that the variation of the packing density of the microgel films is significantly smaller from location to location and from etalon to etalon. In addition, variations in film thickness could also be observed in the ellipsometric measurements as shown in **Figure 2.10**. From the ellipsometric contrast images we can see dark and lighter regions on films prepared by the paint-on technique, which was very common with the paint-on method. In contrast, the films prepared by the doctor blade technique were highly homogeneous. Moreover, the measured film thickness is slightly higher when using the doctor blade technique, which is in agreement with the measured reflectance spectra shown in **Figure 2.9** as the peak with max reflectivity is positioned at longer wavelengths, which is a result of a larger distance between the two Au layers when the microgels are hydrated.

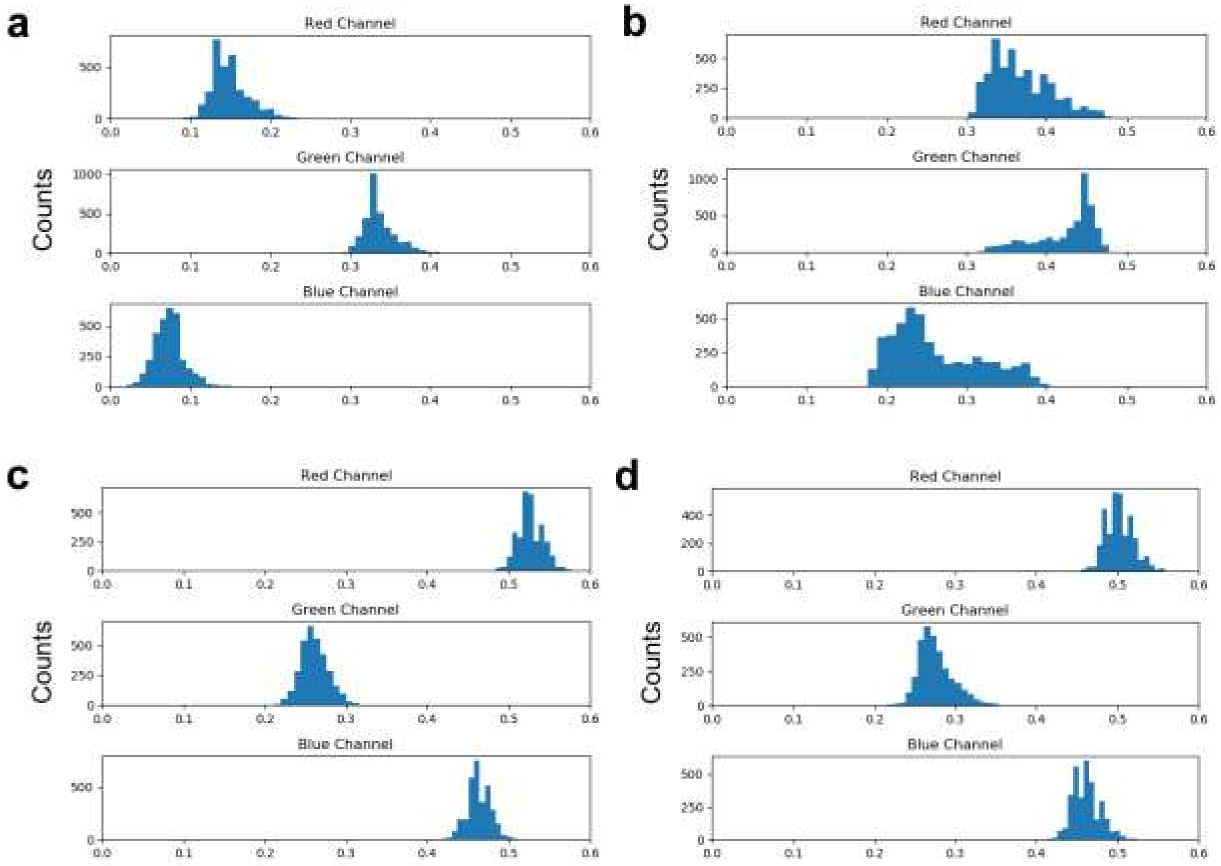

Figure 2.9 RGB value distribution for etalons constructed from pNIPAm-*co*-10%AAc-75C microgels using (a) doctor blade techinque, (b) paint-on method. RGB values distribution for etalons prepared by (c) student A and (d) student B.

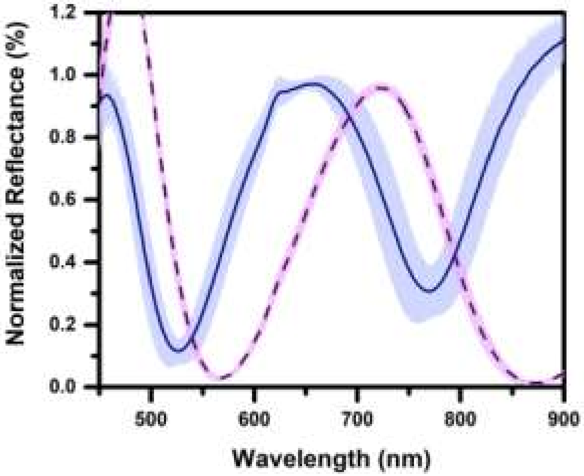

Figure 2.10 Average reflectance spectra for 102 etalon devices of 4 mm^2 composed of pNIPAm-*co*-10%AAc-75C microgels that were fabricated by the paint-on technique (solid) and doctor blade technique (dashed). The shade on lines corresponds to their standard deviations.

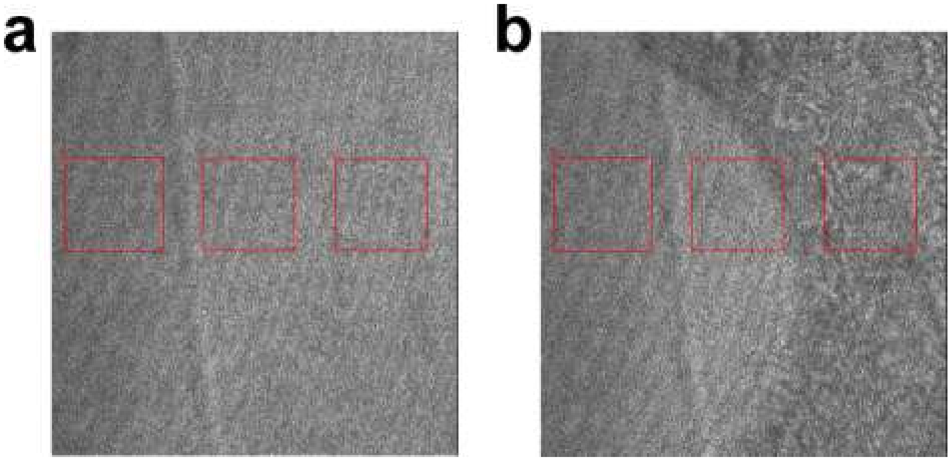

Figure 2.11 Ellipsometric contrast images of pNIPAm-*co*-10%AAc75C microgel films prepared by (a) doctor blade and (b) paint-on techniques. Images were acquired using 532 nm laser and the red squares are the locations where the measurements were done.

The color uniformity and purity of the etalons fabricated using the doctor blade technique was also demonstrated by investigating their pH dependent optical properties and by comparing it with responses from the etalons fabricated by the paint-on technique. **Figure 2.11** shows representative spectra for different etalons at pH 4 and 7.8, and their corresponding peak shift can be found in **Table 2.2**. As shown, the precision of the measurements was significantly increased for all 4 types of etalons prepared by the doctor blade method. This implies that these etalons exhibit more consistent optical properties from etalon to etalon as evidenced by their lower standard deviation and yield more reproducible results. In addition, the calculated peak shift (response) for the pH responsive etalons was higher, with lower standard deviations, than those prepared by the paint-on technique, presumably due to the higher packing density of microgel films formed when using the doctor blade method as suggested from the ellipsometric measurements. In the case of etalons composed of pNIPAm-*co*-10%VAAc microgels prepared via the paint-on method, the peak at 542 nm could not be monitored as it moved to wavelengths higher than our detection range. Thus, we calculated the response based on the peak at ~622 nm.

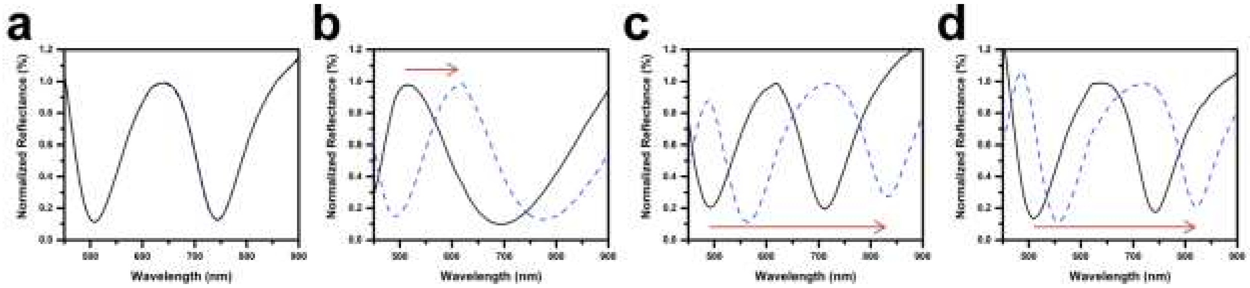

Figure 2.12 Representative spectra for etalons composed of (a) pNIPAm-BIS, (b) pNIPAm-*co*-5%MAAc, (c) pNIPAm-*co*-10%AAc, and (d) pNIPAm-*co*-10%VAAc microgels at pH 4 (solid) and pH 7.8 (dashed). The arrows indicate the direction and total peak shift.

Table 2.2 Peak position and response (peak shift) to pH for etalons prepared by paint-on and doctor blade methods.

Etalon composed of	Method	Peak at pH 4	Peak at pH 7.8	Response
pNIPAm-BIS	Paint-on	592 ± 8	588 ± 10	-3 ± 6
	Doctor blade	637 ± 6	637 ± 6	0 ± 1
pNIPAm-co-5%MAAc	Paint-on	557 ± 9	615 ± 12	58 ± 7
	Doctor blade	519 ± 8	611 ± 7	92 ± 4
pNIPAm-co-10%AAc	Paint-on	447 ± 12	768 ± 16	311 ± 10
	Doctor blade	494 ± 5	831 ± 9	337 ± 5
pNIPAm-co-10%VAAc	Paint-on	542 ± 26	622 ± 25	81 ± 12
	Doctor blade	513 ± 6	820 ± 10	307 ± 6

To investigate how the size variability of the microgels prepared at a different reaction temperature (70 and 75 °C), scale (100 and 500 mL) impact the reproducibility of the fabricated etalons, we compared the average reflectance spectra collected from 102 etalon devices (4 mm^2) constructed from pNIPAm-*co*-10%AAc, pNIPAm-*co*-10%AAc-75A, pNIPAm-*co*-10%AAc-75B, and pNIPAm-*co*-10%AAc-75C microgels. The results can be found in **Figure 2.12(a)**. As can be seen, the peaks in the reflectance spectra for these etalons are positioned at different values, suggesting that these microgels generated films with different thickness presumably due to their different hydrodynamic diameters. Interestingly, microgels prepared at different temperature (70 and 75 °C) and same reaction scale (100 mL) showed different hydrodynamic diameters (**Table 2.1**) and generated etalons with distinct reflectance spectra. However, their visual color was very similar as shown in **Figure 2.7(a,b)**. Similarly, microgels prepared at the same temperature (75 °C) and same reaction scale (100 mL) also showed different hydrodynamic diameters and yielded etalons with distinct reflectance spectra, but with a very similar visual color (data not shown). On the contrary, microgels that were fabricated at the same temperature (75 °C) but different reaction batch (100 and 500 mL) generated etalons with distinct reflectance spectra and color as shown in **Figure 2.7(b,c)** and **Figure 2.12(b)**, presumably due to their significant size difference. As noted from their reflectance spectra, the wavelengths at ~ 500 nm undergo constructive interference for etalons composed of pNIPAm-*co*-10%AAc-75A microgels while they undergo destructive interference for etalons composed of pNIPAm-*co*-10%AAc-75C microgels, which can explain their different visual color. Therefore, the results here suggest that small variability in the microgel size does not have a major impact on their visual color, but these variations can be easily observed in the reflectance spectra and can compromise the reproducibility of the fabricated etalons. However, the low standard deviation in the reflectance spectra for these etalons demonstrates that they were highly reproducible in each batch.

Subsequently, we investigated the reproducibility (day-to-day variability) of the fabrication process. For this, etalons composed of pNIPAm-*co*-10%AAc microgels were fabricated on two different days and the average reflectance spectra for each batch is shown in **Figure 2.12(b)**. As we can see, the reflectance spectra were very similar with peaks at ~ 770 and 772 nm, demonstrating that these etalons had similar optical properties and their fabrication was very reproducible.

To illustrate the universality of the doctor blade method, etalon devices were fabricated by two students that had minimal to no experience on the fabrication process and their color uniformity and consistency were compared by evaluating their reflectance spectra and distributions of the RGB values. Student A had fabricated etalon device once using the paint-on method while student B had never had contact with the fabrication process. Once again, 102 spectra were collected from individual etalon devices and the average spectrum along with their standard deviation can be found in **Figure 2.12(c)**. Etalons were composed of pNIPAm-*co*-10%AAc-75C and the spectra were also recorded in DI water. As we can see, the reflectance spectra for both students were very similar to the one previously prepared by the investigator and the small standard deviations in each spectrum demonstrate the high precision of the fabricated etalon devices. The RGB values distributions for these etalons were also sharp and similar to each other as can be seen in **Figure 2.9 (c,d).** Using the proposed doctor blade method, the quality of the etalons in terms of color purity, uniformity, and consistency were greatly enhanced and does not depend on the manufacturer expertise.

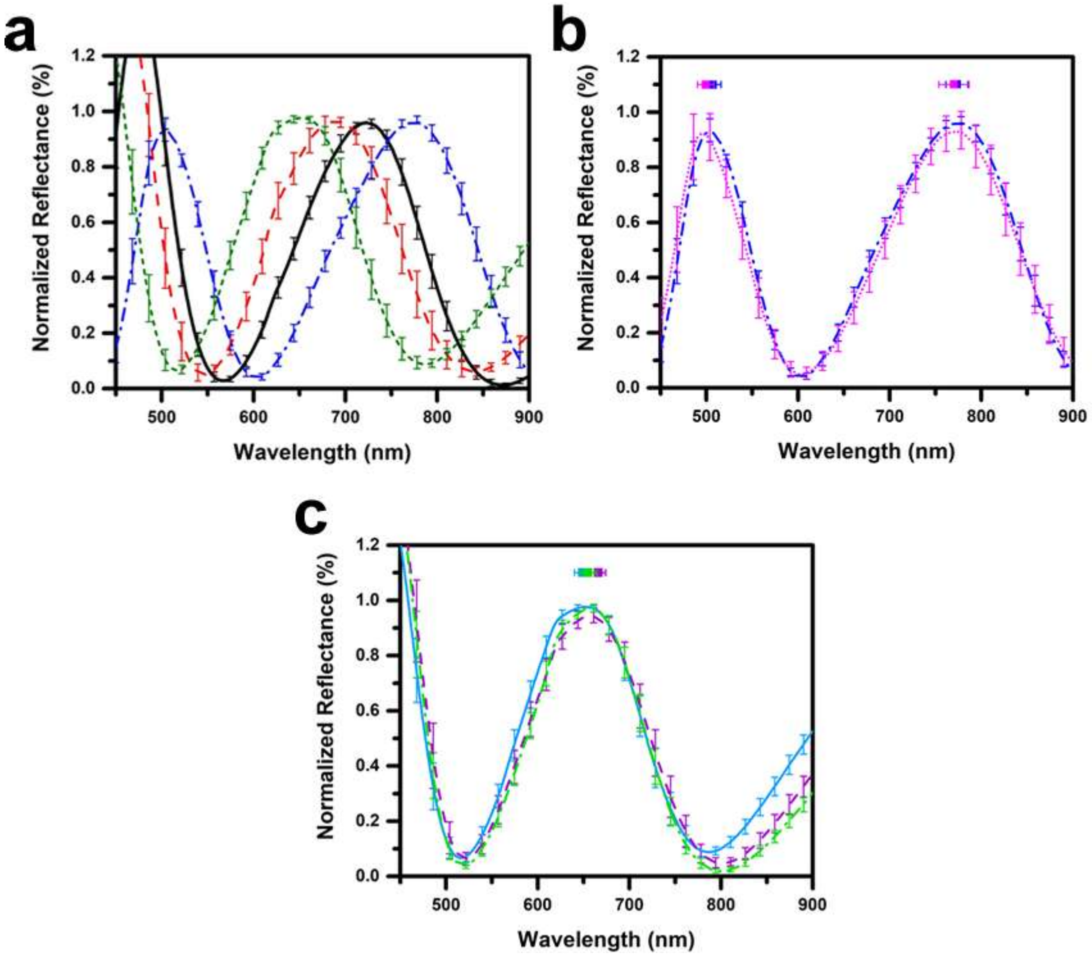

Figure 2.13 Average reflectance spectra for etalons composed of (a) pNIPAm-*co*-10%AAc-75C (green short dashed), pNIPAm-*co*-10%AAc-75B (red dashed), pNIPAm-*co*-10%AAc-75A (black solid), pNIPAm-*co*-10%AAc (blue dashed dot) microgels. (b) Average reflectance spectra for etalons fabricated in two different days using the same microgel solution (pNIPAm-*co*-10%AAc). (c) Average reflectance spectra for etalons fabricated by student A (purple dashed), student B (green dashed dot), and investigator (blue solid) using the doctor blade method. All the spectra represent the average of 102 etalons. The error bars in each spectrum correspond to their standard deviation and the average of the peak position with the standard deviation is located above of the peaks in (b) and (c).

Finally, we investigated the etalon's response dependence with size. For this, etalons composed of pNIPAm-*co*-10%AAc microgels were fabricated in different sizes, ranging from

625 mm^2 to 4 mm^2. The fabricated etalons were incubated in PBS buffer pH 7.4 solution and exposed to increasing concentrations of NaCl solutions (also prepared using PBS buffer pH 7.4 as a blank). The accumulative peak shift was recorded and the results can be found in **Figure 2.13.** As evident, the response to NaCl did not vary significantly with size, suggesting that is more dependent on the microgel film thickness and less on the size of the.

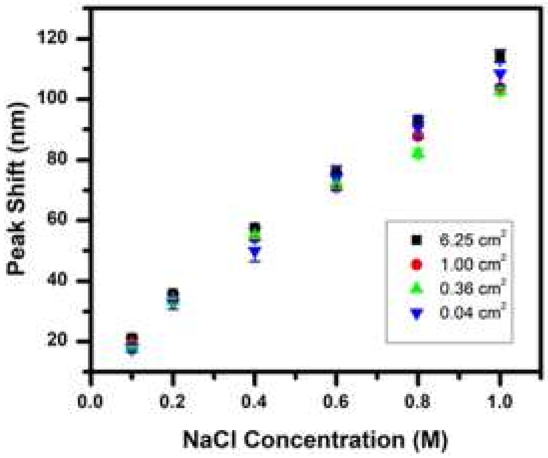

Figure 2.14 Accumulative peak shift for etalons of different sizes composed of pNIPAm-*co*-10%AAc microgels. Each data point represents the average of 4 measurements and the error bars correspond to the standard deviation.

2.4 Conclusions

In summary, we have applied a new method that utilizes a custom-built painting platform and the doctor blade technique to fabricate highly uniform microgel layer on Au coated substrates. Etalon devices were fabricated using 4 types of pNIPAm-based microgels and following the paint-on and doctor blade methods. Their optical properties, color purity and uniformity were compared based on their reflectance spectra and RGB value distributions. Using the proposed method, the variability of the etalons was significantly decreased as demonstrated by the lower standard deviations in their reflectance spectra and pH responses. Furthermore, we showed that the quality of the etalons fabricated does not depend on the manufacturer expertise and someone with no experience in the fabrication process can achieve devices with similar qualities. Furthermore, the variability in the microgel sizes due to reaction temperature and reaction scale on the fabricated etalon devices was also tested. We observed that these variability in microgels size can easily be seen in the reflectance spectra but small changes in the microgel size does not impact on their visual color. In the next chapter, we will evaluate their potential as portable colorimetric pH sensors.

Chapter 3

Detecting Solution pH based on Colorimetric Measurements of pNIPAm Microgel-Based Etalon Optical Devices

3.1 Introduction

Stimuli responsive polymers that respond to external stimuli by changing (reversibly) their chemical and/or physical properties have been a focus of considerable scientific investigations due to their potential application in drug delivery[121], smart coatings[122], sensing and biosensing.[123] Their vast potential is a result of the variety of chemical modifications that can render microgels responsive to specific external stimuli, such as temperature, pH, solvents, biomolecules, light, etc. A well studied stimuli responsive polymer is poly(*N*-isopropylacrylamide) (pNIPAm) which is known to undergo a reversible phase change at the lower critical solution temperature (LCST) of 32 °C, where the polymer switches from a random coil, fully water-soluble when the solution $T < 32$ °C to an insoluble globule conformation when the solution $T > 32$ °C.[56] When crosslinked, thermoresponsive hydrogel colloidal particles, called microgels, can be obtained that exhibit similar properties. Microgels based on pNIPAm are highly soluble and swollen when the solution $T < 32$ °C while they collapse, expelling their water of solvation at $T > 32$ °C. The volume phase transition temperature (VPTT) can be modulated by the addition salts and surfactants in the aqueous medium,[124-127] changes in the solvent polarity,[128] or chemically by copolymerization with a more hydrophilic/hydrophobic comonomer.[47, 77, 129] Increasing the overall hydrophobicity of the copolymer is known to lower the LCST while increasing the overall hydrophilicity tends to raise the LCST to higher temperatures. Hence, the introduction of functional comonomers in the microgels synthesis provides a gateway to obtain versatile systems with particular properties for specific needs. A common modification is the introduction of ionisable comonomers that shifts the VPTT to higher values and renders ionic microgels that are pH responsive in addition to temperature.[107, 130] The swelling of neutral microgels based on pNIPAm is determined by the equilibrium between the polymer elasticity and the osmotic pressure. However, the introduction of localized ionisable groups into the microgels network introduces an additional osmotic pressure to the swelling that depends on the effective charge density of the microgels and can be explained based on the Donnan potential of the mobile counterions.[73, 75] Moreover, additional electrostatic repulsive forces of like charges need to be considered when dealing with these systems. Thus, the swelling state of ionic microgels depends on the amount of the ionisable comonomer introduced, the solution pH and ionic strength that influences the degree of ionization and the Debye screening length. Examples of ionisable comonomers include acrylic acid (AAc), methacrylic acid (MAAc), and vinylacetic acid (VAAc). A schematic representation of the microgels behaviour in containing AAc, MAAc, and VAAc in response to pH variations is displayed in **Figure 3.1**. Anionic microgels that are responsive to either a narrow or broad pH range can be obtained from these comonomers.[107] When the solution pH > pK_a of the pendent groups, most of the carboxylic acid groups are in their deprotonated form and the microgels swell as a result of charge-charge repulsions and increased in the osmotic pressure. However, when the solution pH < pK_a, most of the carboxylic acid groups are protonated and the microgels shrink.

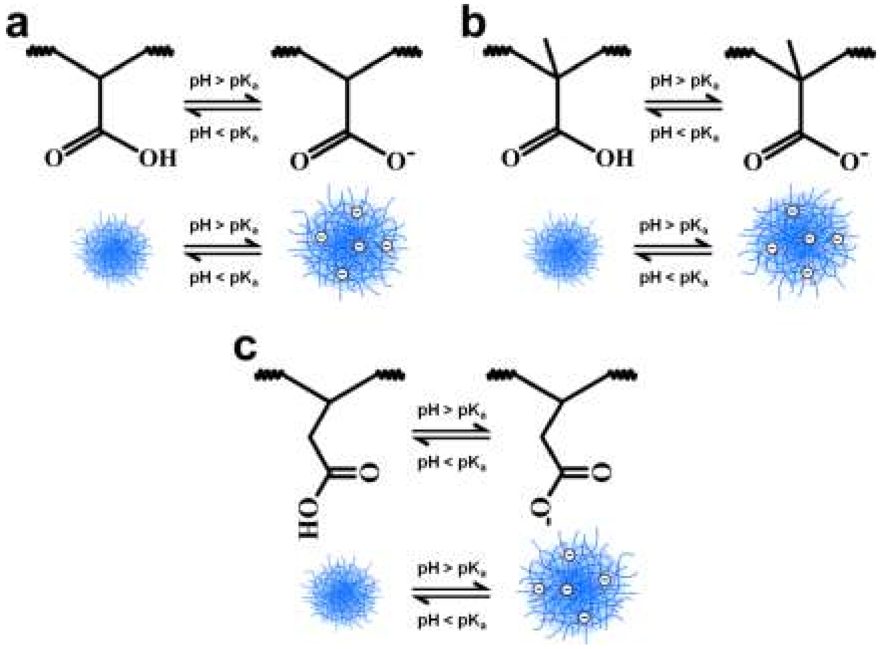

Figure 3.1 Swelling mechanisms of (a) pNIPAm-*co*-AAc, (b) pNIPAm-*co*-MAAc, (c) pNIPAm-*co*-VAAc microgels. At pH = pK_a, the degree of protonation equals the degree of deprotonation. At pH > pK_a, most of the carboxylic groups are in the deprotonated form while at pH < pK_a, most of the carboxylic groups are protonated.

Our group has fabricated etalon optical devices from pNIPAm-based microgels by sandwiching a highly packed microgel monolayer between two thin reflective Au layers.[78-79] Due to their structure, the etalons are visibly colored and show unique multi-peak reflectance spectra which are a result of light interference when resonating in the microgel layer between the two reflective Au layers. For constructive interference, the peak position and order can be predicted using Equation (3.1).

$$\lambda m = 2d\eta cos\theta \tag{3.1}$$

where the maximum wavelength (λ) being reflected/transmitted depends on the refractive index (η) of the dielectric layer (microgel layer), the angle of incident light (θ), the peak order (m), and the distance between the two Au layers (d), which in this case is modulated by the swollen state of the microgels. Therefore, a shift in λ visually seen as a color change is expected as the thickness of the microgel layer, d, changes in response to external stimuli. We have experimentally observed that the optical properties of the etalons is mainly dictated by d when θ is fixed, indicating that the changes in refractive index of the microgels as they collapse is negligible compared to d.[74]

The group has demonstrated in numerous publications the potential of the technology for sensing DNA,[85, 131] proteins,[84, 110, 132] volatile organic compound vapors,[80] hydrogen peroxide (H_2O_2),[82, 133] carbon dioxide (CO_2),[134] lipids (triglycerides),[135] solution pH,[118] glucose, [109] hormone (progesterone) in aqueous medium,[136] humidity,[137] and for determining molecular weight of polymer.[138-139] In all cases, the color change in response to the specific target or stimuli was quantified by tracking the peak shift in the reflectance spectra using a reflectance probe coupled with tungsten light source and spectrometer. In this study, for the first time, colorimetric measurements based on the RGB the etalon devices (obtained from digital images) were carried out to quantify their color change in response to solution pH. Furthermore, the ability of using the etalons as portable pH sensors for drinking water was explored. Four sets of etalons were investigated and those composed of pNIPAm-co-5%MAAc microgels showed promising results. Furthermore, reference models were created covering a pH range of 4 to 8, validated, and tested against a range of salt concentration and temperature. Finally, the sensors were used to predict the pH of drinking water samples. The mean absolute error (MAE) was calculated to be 0.3 pH units for ideal solutions and 0.6 pH units for more complex solutions.

3.2 Experimental Section

3.2.1 Materials

N-isopropylacrylamide (NIPAm) monomer was purchased from TCI (Portland, Oregon) and purified by recrystallization from hexanes (ACS reagent grade, EMD, Gibbstown, NJ) before use. N,N'-methylenebisacrylamide (BIS) (99%), acrylic acid (AAc) (99%), methacrylic acid (MAAc) (99%), vinylacetic acid (VAAc) (97%), ammonium persulfate (APS) (≥98%), sodium chloride (NaCl), sodium hydroxide (NaOH) were obatained from Sigma-Aldrich (Oakville, Ontario) and were used as received. Hydrochloric acid (HCl) was purchased from Caledon Lab. (Georgetown, Ontario). Whatman #1 paper filters were obtained from GE Healthcare (U.K.). Deionized (DI) water with resistivity of 18.2 MΩ·cm was obtained from a Milli-Q Plus system and was used for all experiments. A pH meter (JENCO 6173, San Diego, CA) coupled with ROSS micro pH electrode (Thermo Scientific, Markham, ON) was used to prepare solutions of varying pH values (from 4 to 8) using either NaOH or HCl. Cover glasses (625 mm^2) with thickness of 0.13 – 0.17 mm and calcium chloride ($CaCl_2$) were purchased from Fisher (Ottawa, Ontario). Cr flakes (99.999%) were obtained from ESPI (Ashland, OR) and Au (99.99%) was obtained from MRCS Canada (Edmonton, AB).

3.2.2 Synthesis of pNIPAm-Based Microgels

Microgels were synthesized via surfactant-free free radical precipitation polymerization following a previously published procedure. Briefly, the monomer solution containing NIPAm (59.5 mmol) and BIS (3.515 mmol) was filtered through a 0.2 μm syringe filter and transferred to a 1 L 3-neck round bottom flask fitted with a reflux condenser, nitrogen gas inlet, thermometer, and stir bar. The solution was purged with N_2 gas while stirring and heated to 70

^{o}C for over 1 h. Following, one of the comonomers AAc or VAAc (7.15 mmol) was directly added to the reaction mixture using a micropipette and the polymerization was initiated by injecting in one aliquot a solution of ammonium persulfate (APS) (1 mmol dissolved in 1 mL DI water). The reaction was allowed to proceed at 70 ^{o}C for 4 h under N_2 gas atmosphere. Next, the resulting suspension was cool down overnight at room temperature while stirring and filtered through glass wool to remove large aggregates. The resulting microgel solution was finally purified via centrifugation 6 times and stored as a concentrated microgel pallet. Following this procedure, microgels composed of 10%AAc and 10%VAAc was obtained. For microgels composed of 30%AAc the mols of NIPAm, BIS, and AAc were 45.7, 3.151, and 21.09 mmol respectively while for microgels composed of 5%MAAc the mols of NIPAm, BIS, and AAc were 63.148, 3.508, and 3.508 respectively. Before using the microgels to fabricate the etalon devices, their concentration was adjusted. For this, 100 µL of the microgel solution was transferred to a microscope glass slide as a single droplet, quickly positioning it vertically and recording the distance that it traveled for 1 min. DI water was added or removed until achieve 0.15 to 0.3 inches in 1 min.

3.2.3 Etalon Fabrication

Etalon arrays were fabricated following the doctor blade technique described in Chapter 2. Shortly, ethanol/DI water rinsed cover glasses were coated with 2 nm Cr/15 nm Au using a thermal evaporator system (Torr International Inc., New Windsor, NY). Following, the cover glasses were placed in the painting platform and with the assistance of a microscope glass slide, the microgel solution of fixed concentration was spread through the painting platform surface, forming a film of ~0.15 mm on the surface of the cover glasses. The cover glasses were quickly transferred to a hot plate set at 35 ^{o}C and allowed to air-dry for 1 h. The excess microgel was then removed by extensively rinsing the cover glasses with DI water until no traces of the gel could be seen. The glass substrates were incubated in DI water at room temperature overnight and a second 2 nm Cr/5 nm Au layer was deposited after they were rinsed again with DI water and dried with N_2 gas. The deposition rate was kept constant at 0.19 Å s^{-1} and 0.17 Å s^{-1} for Cr and Au respectively. Furthermore, a metal mask containing 64 squares of 4 mm^2 was placed in front of the cover glasses to obtain 64 etalons as an array in a single cover glass. The resulting etalon arrays were soaked in DI water overnight at room temperature, after which they were ready for the pH experiments.

3.2.4 pH Analysis and Picture Acquisition

Overnight hydrated etalon arrays were exposed to solutions of varying pH and ionic strength (IS). For this, the etalon array was transferred to a Petri dish containing 10 mL of the desired pH/IS solution, allowing the excess of DI water to drip. After 20 minutes incubation, photographs of the etalon array was obtained using a studio mini box and two types of a custom-built 3D printed white box: one with the camera angled at 10^{o} (box #1, see **Figure 2.3** of Chapter 2) and the other one with the camera angled at 0^{o} (box #2) relative to the sensor surface as shown in **Figure 3.2**. Both 3D printed boxes had similar dimensions and were coupled with a raspberry pi 4, raspberry pi camera V2 8MP, LEDs, and a diffuser. Details of the dimensions for the box #2 can be found in Appendix C. After 20 minutes incubation in the desired pH solution, the Petri dish was placed inside the 3D printed box, the box was closed, and a photograph was taken using the raspberry pi system. In the studio mini box set up, photographs were taken using a cell phone camera (LG 4) and a tripod. The cell phone was angled at 10^{o} relative to the bench's surface and the distance from the camera to the sensors was kept at ~20 cm. After photographing, the etalon array was rinsed with DI water for 30 seconds and transferred to another Petri dish containing ~20 mL of DI water where it was incubated for > 30 minutes to reset. After resetting the etalon array, it was again exposed to another solution of the desired pH/IS for 20 minutes repeating the procedure described above. The etalon arrays were reused at least 10 times before being disposed. It is important to point out that as the etalons composed of pNIPAm-based microgels show temperature responses, the temperature for all the solutions during the experiments was tracked, which varied from 19 to 21 °C. We observed (data not shown) that this small variation in temperature did not caused a significant color change.

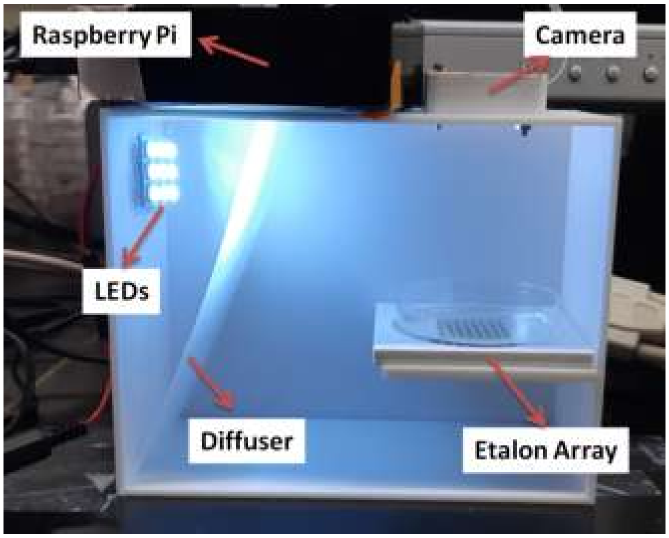

Figure 3.2 Photograph of the costume-built 3D printed box #2 coupled with a raspberry pi, camera angled at 0^o relative to the sensor surface, LEDs, and a diffuser. Its dimensions are 15, 6.9, and 12 cm in length, width, and height respectively. The sensor support is 7.3 cm away from the camera.

3.2.5 Reflectance Measurements

Reflectance spectra for the etalons in response to pH were collected using a Red Tide USB650 spectrometer, a LS-1 tungsten light source, and a reflectance probe obtained from Ocean Optics (Dunedin, FL). The spectra were recorded using Ocean Optics Spectra Suite Spectroscopy Software over a wavelength range of 450-950 nm. Moreover, emission spectra for the LEDs were recorded using the same apparatus but with the tungsten light off.

3.2.6 Color Characterization

Color model is an abstract mathematical representation of colors in space that uses mathematical functions to convert or predict a color coordinates position determined from a combination of primary colors and describing ways that colors can be represented.[140] For instance, the RGB color model is an additive color system that uses various combinations of **R**ed, **G**reen, and **B**lue and it is commonly used for display in electronic systems such as computers, digital cameras, and TVs.[141] In the 24-bit RGB color model, each channel uses 8 bits that corresponds to possible integer values ranging from 0 to 255. For example, a color can be numerically expressed as an RGB triplet (r,g,b), indicating how much (from 0 to 255) of each red, green, and blue is combined. Thus, there are 256*256*256 = 16,777,216 possible colors by combining different ratios of red, green, and blue. Since the colors are represented by three components, a 3D RGB cube can be constructed by considering each component (R, G, and B) as a Cartesian coordinates in a Euclidean space where all the components assume positive integers as showing in **Figure 3.3(a)**. The cube assumes values within 0-1 range where the resulting color is black in the origin (0, 0, 0,) while it is white in the vertex (1, 1, 1) opposite to the origin. RGB values in the range of 0 to 255 can be converted to 0-1 range by simply dividing their values by 255. In this model, the hue of a color is defined by the intensity of each component and the saturation is defined by the difference between the highest and lowest intensity values. As each color in this system is represented by a single dot in the 3D space inside of the RGB cube, it is possible to perform quantitative measurements of their color similarity by calculating the distance between them. In addition, colors can be distinguished based on their brightness, hue, and saturation properties, which can also be represented as luminance (brightness) and chrominance (hue and saturation) components.

The RGB color model is a device dependent as different devices reproduce or detect a specific RGB value differently due to the nature of the light source and the detection system that varies from manufacturer to manufacturer. For example, digital cameras often operate with a Bayer filter arrangement, where the green channel is given 2 detectors while red and blue channels are given 1 detector each. These 4 detectors result in 1 group of 4 pixels where each pixel has only one of the three color component (red, green, or blue) and the other two colors are interpolated. Usually, the green channel is given more detectors to obtain higher luminance (brightness) resolution rather than chrominance resolution as human eyes are more sensitive to the green region of the spectrum.[142]

The CIE XYZ color space, also known as CIE 1931 color space, was the first mathematically defined color space that links spectral colors (wavelengths in the visible region of the electromagnetic spectrum) with the physiological perceived colors that humans can see.[143-144] It was create by the International Commission on Illumination (CIE) in 1931 and is based on the tristimulus values denoted by X, Y, and Z obtained from color matching functions that correlates the light spectral power (spectral radiance) with the spectral sensitivity of the three individual kinds of cone photoreceptor cells.[145-146] Here, colors are represented by a combination of X, Y, and Z where Y is intentionally set to closely match the luminance while X and Z give chromaticity (hue and saturation) information. It maps a range of physically produced colors to an objective description of the colors that we can see from mixing different amounts of the three primary colors red, green, and blue, similar to an additive color model. Thus, the primary colors are considered as hypothetical as they do not correspond to the true wavelengths of light. Rather, it is the amount of each stimulus that defines the color.

The concept of color can be broken down into luminance and chromaticity. Since the Y is intentionally set as luminance, all possible chromaticites will fall in the XZ plane at that specific luminance. Similar to RGB color model, the XYZ values can also be represented in a 3D space considering the three components as the Cartesian coordinates where the XZ plane defines the chromatic color and the Y coordinates specifies the luminance.[147] The chromaticity coordinates can be normalized relative to their sum according to Equation 3.2, 3.3, and 3.4:

$$x = \frac{\mathrm{X}}{\mathrm{X+Y+Z}}; \tag{3.2}$$

$$y = \frac{\mathrm{Y}}{\mathrm{X+Y+Z}}; \tag{3.3}$$

$$z = \frac{\mathrm{Z}}{\mathrm{X+Y+Z}} = 1 - x - y \tag{3.4}$$

Consequently, chromaticity information can be represented in a 2D diagram known as CIE xyY color space as shown in Figure 3.3(b) and is commonly used to represent colors in practice. The CIE XYZ color space is a representation of color that is independent of the device and serves as standard reference from which other color spaces are defined. For instance, a color model is usually associated with a color mapping function that translates the color model to a reference standard color space such as the CIE XYZ, establishing a define color-gamut. Matrix transformations can convert sRGB values into XYZ tristimulus values and be represented in the

CIE xy chromaticity diagram.[148] In **Figure 3.3(b)** we can see the reference CIE XYZ color space containing the standard RGB (sRGB) color space (inset black triangle) of the RGB color model.

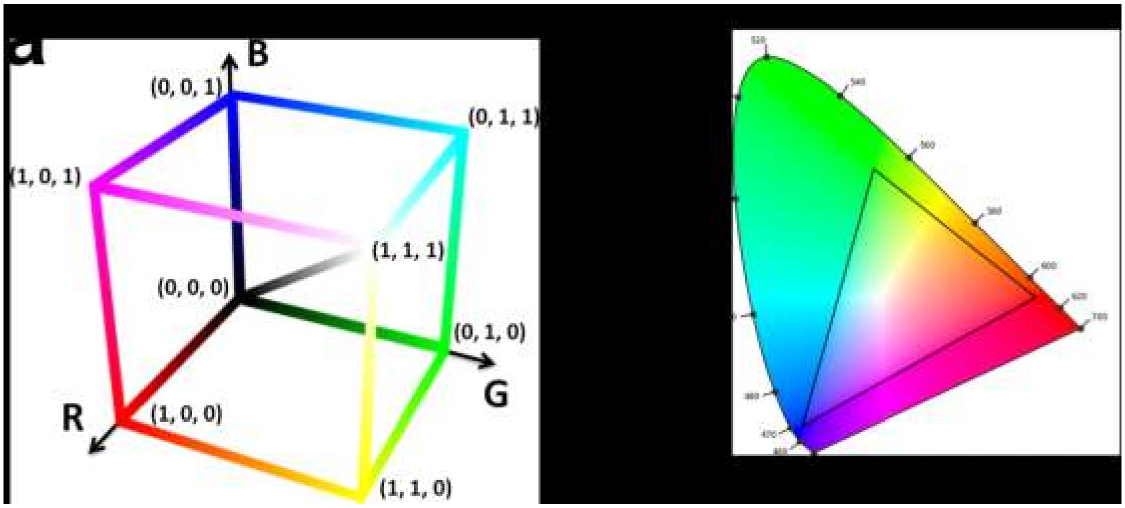

Figure 3.3 (a) RGB color space represented as a cube where the values originate from the origin (0, 0, 0) to a maximum value 1 and (b) CIE xyY chromaticity space where the outer curve boundary correspond to the monochromatic locus with the wavelengths displayed in nanometers and the inset black triangle is the sRGB color space.

For the investigation in this chapter, we used an 8 megapixel raspberry pi camera module V2 that uses a Bayer filter organised as BGGR pattern and a complementary metal-oxide-semiconductor (CMOS) imaging sensor (Sony IMX219) with pixel size of 1.12 x 1.12 µm.[149] When capturing images, the voltage in each pixel is recorded and converted into a digital representation called *analog-to-digital unit* (ADU) or *digital number* (DN), which can be recorded as either 12 or 14 bits depending on the camera's circuitry. If the camera is able to record 12 bits, each pixel can record 4,096 different brightness levels while 14 bits results in 16,384 different brightness levels. When the camera makes an exposure, the photograph can be saved as raw file or in a "positive" file format such as JPG for visualization. If the photograph is saved as raw file, the camera’s data sensor is recorded as raw Bayer data and contains the full resolution, minimally processed data collected from each pixel. In this case, the raw data contains twice as many green pixels as red or blue and a demosaicing process needs to be performed to make it a normal looking image.

Usually, most output devices can only display 8 bits per channel and the original input data in the form of 12 or 14 bits must be converted. By default, most digital cameras process the photograph raw file into JPG/JPEG. In this case, the camera converts the 12 or 14 bits file into 8 bits mode and now each pixel has 256 brightness levels for each color channel. In addition, a Bayer demosaicing process is performed which translates the Bayer array pattern of primary colors into an image that contains values for each primary color (RGB values) at each pixel. This is achieved by using statistical tools to predict the brightness level of the adjacent missing colors. The color in an image is thus represented by the value of brightness that each primary color possesses in each pixel.

The response of a digital image sensor is directly proportional to the number of photons that strike each pixel and the response is said to be linear. Thus, the data that is saved as a raw file is also linear. That is, the input tone will be equal to the output tone and the image will look darker with low contrast compared to normal photographs. However, human perception of brightness is non-linear with higher sensitivity to changes between darker tones than to changes between lighter tones, closely approximating a log curve. Therefore, a non-linear curve must be applied to the image to enhance the contrast between neighbouring regions of brightness, making the tonality of the image more closely match the way human visual perceptual system works. These non-linear adjustments, called gamma correction, are applied by a software inside the camera when the image is saved as JPG/JPEG. In the raspberry pi camera, the sensor is gamma corrected and the image is gamma encoded when it is saved.

Here, the color information of the etalons was stored in 24 bits (8 bits for each channel) as JPG format, which was obtained entering in the command line raspistill application in the default mode where the blue and red gains are set to 1.5 and 1.2 respectively (fixed white balance). In addition, by default, the sharpness, contrast, color saturation, and EV (exposure value) compensation are all set to 0 while the brightness to 50. The images were cropped in order to isolate each individual etalon for further color analysis. Following, the mean sRGB values were obtained from 68 x 68 pixels and when mentioned, they were converted into XYZ tristimulus values using matrix transformations to be represented as CIE xy chromaticity coordinates.

3.2.7 Grouping

All the etalons were clustered into 5 groups based on their chromaticity coordinates at pH 4 and 8 using the k-means clustering algorithm. For a given set of observation vectors (x_1, x_2,…, x_n), the *k*-means clustering algorithm partitions the dataset into k sets (S_1, S_2,…, Sk) of distinct non-overlapping groups, where each observation is assigned to the cluster with the closest centroid while recalculating (updating) the mean of the centroid and minimizing the in-cluster sum of squares of the residuals.[150-152] Mathematically, the centroids are calculated based on Equation 3.5:

$$J = \sum_{i=1}^{k} \sum_{x \in S_i} ||x - \mu_{\mathrm{i}}||^2 \tag{3.5}$$

where μ_{i} is the mean of data set in the centroid Si, x is the set of observations, and k is the specific number of the cluster.

3.3 Results and Discussion

3.3.1 Color variation as a Function of pH for pNIPAm-*co*-10%AAc Microgel-Based Etalons

Initially, we evaluated the ability of predicting solution pH based on the RGB of etalons composed of pNIPAm-*co*-10%AAc microgels. For this, we prepared etalons of 4 mm^2 size following the Doctor blade technique as discussed in the experimental section. Next, the etalon devices were individually exposed to solutions of varying pH (from 2 to 7) for 20 minutes. This range of pH was chosen considering the pH responsivity range of microgels containing acrylic acid (pKa ~ 4.25). Pictures of the etalons were obtained using a cell phone camera (LG 4) with an angle fixed at 10^o and a mini-studio box to maintain constant light conditions. The distance of the camera to the sensors was 12 cm. Furthermore, the etalons were tested against two water samples of pH 5.5 and 3.9 that were prepared by adjusting the pH of DI water and a drinking water sample that was collected from a nearby water fountain, which had a pH 7.7 measured with a pH meter. **Figure 3.4(a)** shows the actual cropped photographs of the etalons in different pH values and the drinking water sample. As we can see, the color of the etalons in the standard solutions gradually changes from red to green, with a color transition between pH 4 to 5, indicating that the etalons can be used to qualitatively classify acidic and neutral solutions based on their color. Furthermore, we can predict from the images that the water sample's pH is higher than 7 as it shows a brighter green. However, for more accurate measurements, we plotted the R, G, and B values of the etalons against the pH. As shown in **Figure 3.4(b)**, the R values decreases as the pH increases while the G value decreases from pH 2 to 4 and increases from pH 4 to 7, and the B value increases from pH 2 to 4 and decreases from 4 to 7. To predict the drinking water sample's pH, which can vary from 5 – 8, the values from 4 to 7 was fitted into a linear regression model using the least squares to obtain the best fit. Using these equations, the predicted pH value for the water sample was 7.3 ± 0.2, which is the mean and standard deviation of the pH calculated from R, G, and B models, while the pH measured using a pH meter was 7.7. A t-test indicated these results do not differ statistically, since the $t_{calculated}$= 3.464, less than the tabulated value of t at the 95% confidence level (4.303). Moreover, the pH predicted for the two water samples of pH 5.5 and 3.9 were 4.8 ± 0.8 and 3.7 ± 0.8 respectively.

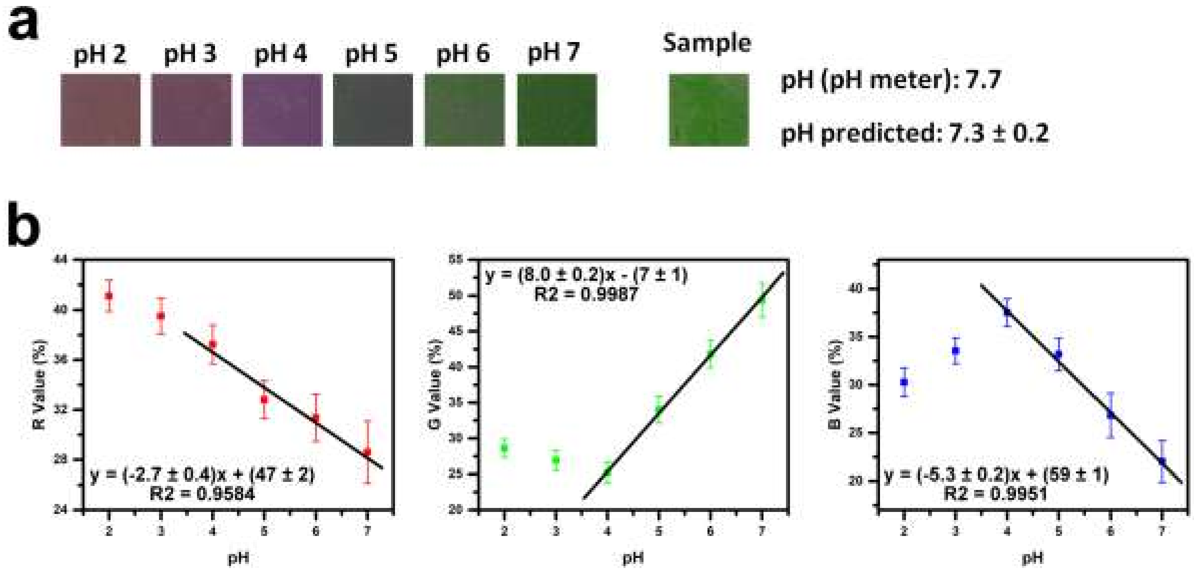

Figure 3.4 (a) Actual photographs of the etalons composed of pNIPAm-*co*-10%AAc microgels under different pH values. Each square correspond to one etalon in the assigned pH value located above each square. These pHs were obtained using a pH meter while the predicted pH for the water sample was calculated based on the RGB regression models from 4 – 7. (b) Changes in RGB value as a function of pH. The inset equations were obtained from fitting the data from pH 4 to 7 into a linear regression model using the least squares.

3.3.2 Evaluation of the Etalon's Performance as Portable pH Sensors

Based on these promising results, we further investigated the performance of the etalons as portable pH sensors. For this, we 3D printed a support for holding etalons as shown in **Figure 3.5(a)**. We will call it prototype 1. Here, etalons arrays of 3 were incubated in pH standard solutions (references) located on both sides of the sample chamber, also containing 3 etalons. The intention of having etalons soaked in the standard pH solutions is to use their color to create internal calibration curves as the RGB model is device dependent. This would eliminate variations in the RGB values caused by different camera manufacturers. In addition, the etalons used for each portable sensor were collected from the same cover glass slide so their color was compared among themselves. A write-on transparency film was used to seal the top of the chambers, except the sample chamber, and they were filled with the standard pH solutions through small holes located on the side of each chamber, after which they were sealed with thermoplastic adhesive (hot glue). The etalons in the sample chambers were hydrated with DI water and then exposed to a water sample of pH 8.5 for 20 minutes after which a picture of the whole device was taken (**Figure 3.5(a)**) with a cell phone at 10^{o} inside of the mini studio box. The picture was analysed by cropping individual etalons and extracting their average %RGB values. **Figure 3.5(b)** shows their average %RGB values as a function of pH. As shown, the RGB values do not follow the linear trend previously observed. This might be due to angle variation from top to bottom of the etalons relative to the camera and the small volume of the standards used to fill the chambers that are subjected to pH variations, affecting the final color the devices. Furthermore, cross contamination between the standards and the formation of bubbles were also an issue in prototype 1, which might have caused this non-linear behaviour in the pH responses. Nonetheless, when fitting the data from pH 8 to 12 into linear regression, except for blue channel that was from 6.5 to 10, and using the models to predict the pH of the water sample, the pH calculated was 7.9 ± 0.7, and using only the green channel, it was 8.5. However, these results were obtained because we knew the pH value of the water sample, which allowed us to use the right calibration curves (from pH 8 to 12). In a more complex situation of measuring unknown pH solutions, the prediction would not be accurate.

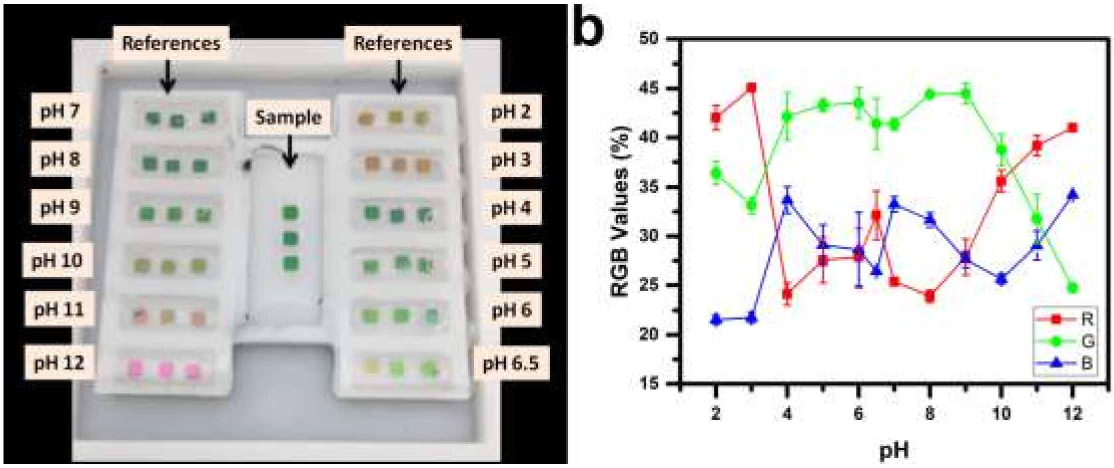

Figure 3.5 (a) Photograph of the prototype 1 pH sensor using the etalon devices composed of pNIPAm-*co*-10%AAc microgels. The photograph was taken after the etalons in the sample chamber were exposed to the water sample for 20 minutes. The etalons in the reference chambers were incubated in the desired pH solution standard for at least 4 hours to assure stability. (b) Averages of the %RGB values as a function of pH obtained from the etalons in (a). Each data point represents the average of 3 etalons and the error bars correspond to their standard deviations.

To avoid the problems above mentioned, we 3D printed another type of support for the etalon devices as shown in **Figure 3.6(a)**. Here, each sensor support contains a square reservoir that holds 3 etalon devices in an array and has dimensions of 2, 1, and 0.2 cm in length, width, and depth respectively. Before assembling the etalons in the sensor support, we exposed them to pH 8 solution and only those that showed a green color were selected for further use. As different cell phones capture and process images differently, we used two colored tapes (blue and green) as a reference for correcting the RGB values of the etalons and correlate it with an already existing internal calibration curves to calculate the solution pH. Initially, these sensors were used to create the internal calibration curves in two environments with different light conditions using the same cell phone to investigate how the light conditions affect the models and the RGB of the tapes. For this, 4 sensors containing 3 etalons each were exposed to pH 4, 6 and 8 solutions (DI water adjusted with HCl or NaOH) and pictures were taken after 20 minutes in the mini studio box and on the lab bench. Moreover, the angle of the cell phone was kept constant at 10^{o} for the mini studio box and the pictures looked similar to the one shown in **Figure 3.6(a)** top. However, when using the same conditions to take pictures on the lab bench, the etalons seemed dim. Thus, we changed the position of the phone to obtain an optimum recording of their colors and the pictures looked similar to the one shown in **Figure 3.6(a)** bottom.

As the G channel showed to be more sensitive to changes in pH (higher slope), we used only the G channel for our calculations and the results are displayed in **Figure 3.6(b, c)**. As we can see, the color changes of the etalons as a function of pH in both conditions were very similar. The linear regression models created on the lab bench and in the mini studio box were $(5.0 \pm 0.3)x + (5.4 \pm 2)$ and $(5.0 \pm 0.4)x + (4.6 \pm 2.5)$ respectively, suggesting that the different light conditions have minimum effect on the models as their sensitivities were very similar. We believe that this was due to the optimal position of the camera where the etalons showed brighter colors. However, the %G values for both tapes did show variations even though the same cell phone was used. For the green tape, the average %G values were 52 ± 3 and 58 ± 4 for the pictures obtained on the lab bench and in the mini studio box respectively while for the blue tape, they were 28 ± 1 and 25.3 ± 0.2 respectively. Interestingly, the changes in the %G value for both tapes were not proportional as expected. The %G value increased from 52 to 58 while it decreased from 28 to 25.3 which might be due to the transfer functions that are automatically applied to the images, converting linear RGB space into non-linear in order to mimic the non-linear way that humans perceive colors. Due to the non-linear variation in the %G values for the tapes, we decided not to use them as a reference for the pH calculations.

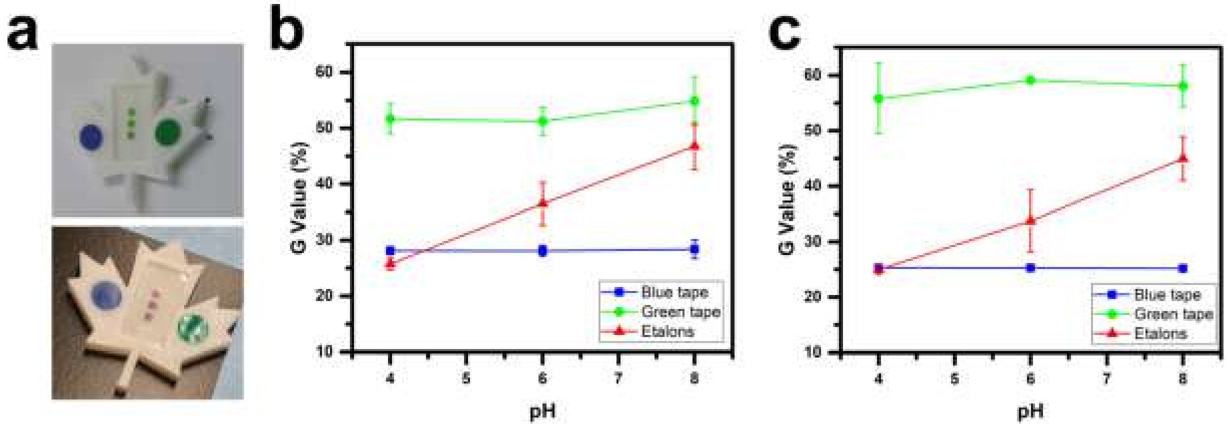

Figure 3.6 (a) Picture of the 3D printed sensor containing 3 etalons incubated in pH 8 solution inside of the mini studio box (top) and incubated in pH 4 solution on the lab bench (bottom). Calibration curves for G channel obtained from the 3D printed sensors in the lab bench (b) and in the ministudio box (c). Each data pont represents the average for 12 individial etalons and the error bars are their corresponding standard deviations.

We further applied the linear regression model obtained on the lab bench to predict the solution pHs used to construct the linear regression model in the mini studio box and vice versa. The average of the calculated pH values using the lab bench linear regression model were 3.9 ± 0.2, 5.6 ± 0.2, and 7.8 ± 0.2 while the average of the calculated pH values using the mini studio box linear regression model were 4.2 ± 0.3, 6.1 ± 0.3, and 8.3 ± 0.3 with a mean absolute error of 0.2 for both models. Following, we investigated how the angle of the camera and incubation time affect the pH calculations. For this, we exposed the 3D sensors with etalons initially dried to a water sample of pH 8.6 and obtained pictures over time at different angles. As shown in **Figure 3.7(a)**, the %G value reaches its maximum after 10 minutes and plateaus up to 65 minutes, after which its value rapidly decreases and seems to plateaus again. **Figure 3.7(b)** shows the corresponding %G values in terms of pH calculated using the lab bench liner regression model. As we can see, the angle had a great impact on the calculated pH. Depending on the angle, the pH could vary 1.6 units, suggesting that the angle is of utmost important parameter and should be fixed through all measurements for good accuracy and precision. Furthermore, the pictures should be taken after 20 minutes and no more than 40 minutes as the standard deviations of the etalons decreased to their minimum after 20 minutes, meaning they achieved a uniform color, and their color drastically changed after 60 minutes. After the experiment, the solution was removed from the pH sensor and the etalons were allowed to air-dry. Following, they were was re-exposed to the pH 8.6 solution and again pictures were taken overtime at different angles. This process was repeated twice and the pH values calculated (data not shown) were significantly different, suggesting that the etalons should be reset with DI water before being used again. Finally, we exposed the pH sensor to drinking water samples and the calculated pH values were not as accurate. The pH of drinking water is usually ≥ 7.0, thus a green color would be expected but it was not always the case. Rather, the etalons showed a red color, suggesting that the composition of the water was impacting the etalons response to pH. This is presumably due to the higher ionic strength of the drinking water which decreases the Debye screening length, decreasing the Columbic repulsion of the dissociated carboxylic acid groups and affecting their swelling behaviour. Thus, more studies needed to be carried out to evaluate how the concentration and type of ions affect their pH responses.

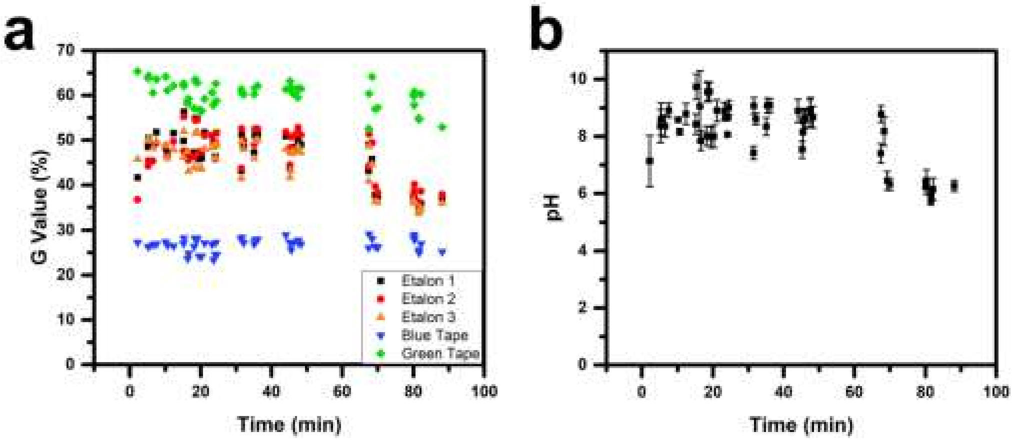

Figure 3.7 (a) %G values over time for one 3D printed pH sensor containing 3 etalons and (b) their corresponding pH values calculated using the lab bench linear regression model.

3.3.3 Type of Light Source

The color change as a function of pH for etalons composed of pNIPAm-*co*-10%AAc microgels was characterized in solutions with different types of radiation to determine the best lighting conditions. For this, 4 sensor arrays containing 64 etalons each were soaked in DI water overnight for hydration. Following, each sensor array was transferred to a Petri dish containing ~10 mL of the desired pH solution and allowed to incubate for 20 min, after which it was placed inside the 3D printed box #1 (with the camera angled at 10^{o}) and a picture was captured using either white, green, or blue LEDs. The emission spectra for the LEDs are displayed in **Figure 3.8(a)**. As shown, the while LED has a sharp peak in the blue region of the electromagnetic spectrum (~443 nm) and a broad peak covering the green and red region (500-650 nm) while the green and red LEDs show a sharp peak at ~ 514 and 630 nm respectively. **Figure 3.8(b)** shows the photographs of the etalons in pH 4 and 8 using the three LEDs. It can be observed from the images that the etalons change color from green to red when using the white LED and interestingly, their color darkens when using the green LED while it lightens when using the red

LED. We hypothesized that their color darkens when using the green LED due to the destructive interference when the pH is increased to 8. When the etalons were in pH 4, they showed a constructive interference peak in the reflectance spectrum at around 500 nm as noted in **Figure 3.8(c)**. As the green LED also emits radiation at around 514 nm, the etalons will look much like the green background and thus they looked lighter with low contrast with the background. However, when the pH was increased to 8, they showed a destructive interference peak at around 540 nm and a constructive peak at around 625 nm. As a result, the wavelengths of light emitted from the green LED undergo destructive interference and the etalons looked darker with high contrast against the background. In the case of the red LED, the etalons looked darker in pH 4 as the LED emits radiation at 630 nm where the etalons showed destructive interferences. However, they had constructive interferences at ~ 630 nm which coincides with the wavelengths of light emitted from the red LED and as a result, the etalons looked lighter with low contrast against the red background.

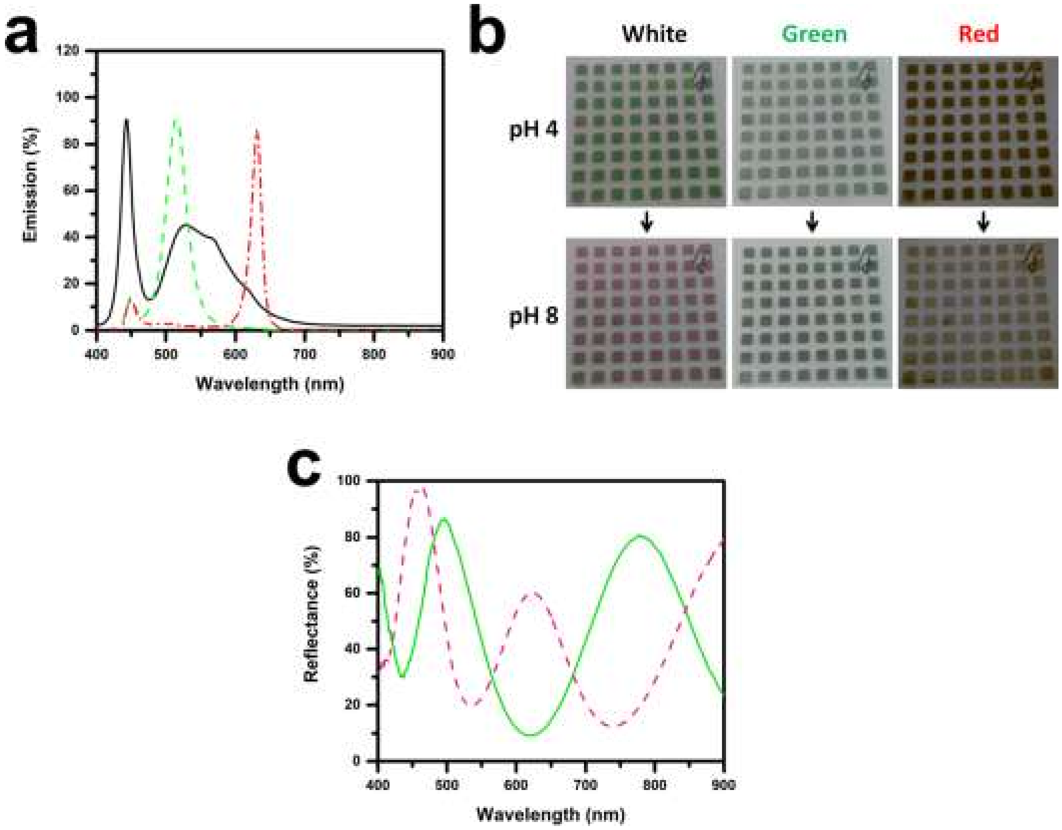

Figure 3.8 (a) Emission spectra for the white (black-solid), green (green-dashed), and red (red-dot dashed) LEDs used for the experiments. (b) Photographs for the same array of etalons composed of pNIPAm-co-10%AAc microgels in pH 4 and 8 captured using white, green, and red LEDs and (c) their corresponding reflectance spectra in pH 4 (green-solid) and 8 (pink-dashed).

The sRGB of the etalons were extracted from the images captured under the three light conditions and were converted into CIE xy chromaticity coordinates as displayed in **Figure 3.9**. This transformation was carried out for a more accurate representation of the etalon's colors as the CIE xyY color space is device independent. We believe that using this approach would eliminate the dependency of the RGB values with the devices. As we can see, the pH responses for the etalons under green light did not show a larger response range compared to the pH responses under the white and red LEDs. Furthermore, their color change was focused on the white spot of the CIE xyY color space while under the white and red LEDs, their showed a wider color variation. We can notice in Figure 3.8 (b) that the pictures obtained using green and red LEDs had a white background, which might be due to the demosaicing process and gamma correction that is automatically applied to the images. In this case, the pictures should be saved as raw Bayer file for further analysis. Based on these results, we decided to continue our experiments using the white LEDs although the red and green LEDs also showed to be very interesting and could be a focus of future investigations.

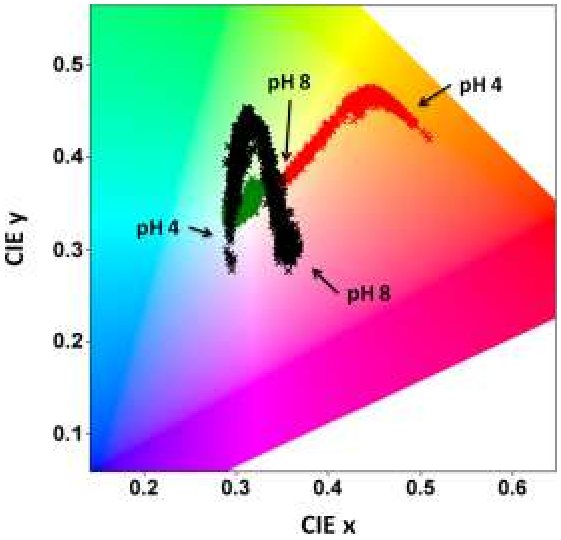

Figure 3.9 Chromaticity coordinates for the etalons as function of pH for the photographs captured under white (black), green (green), and red (red) LEDs represented in the CIE xyY color space. Each plot is represented by 1024 data point.

3.3.4 Color Variation as a Function of pH for Etalons Composed of Different Types of Microgels

The response to pH of etalons fabricated using different types of microgels was further characterized to determine the better system that offers a gradual color change as a function of pH. For this, four sets of pNIPAm-based microgels were synthesized via free radical precipitation polymerization that was fed with 5% mol of AAc, MAAc, VAAc, and 30% mol of

AAc where 5% mol of the crosslinker BIS was kept constant for all the microgels. PNIPAm homopolymer microgels do not exhibit pH responsive properties. However, the incorporation of pH-sensitive comonomers into the network such as AAc, MAAc and VAAc can yield pH responsive microgels due to the protonation/deprotonation of the carboxylic groups. When these anionic microgels are in solution with pH > pK_a of the weak acids, the carboxylic groups are mostly deprotonated, causing the microgels to swells due to the charge-charge repulsions of the localized negatively charged groups and the increased in osmotic pressure inside of the microgels due to the influx of ions from the external solution.[153] However, when the solution pH is decreased < pK_a of the weak acid, the microgels deswell due to the lack of charge repulsion within the network. The transition from swelling to deswelling states of the anionic microgels as a function of pH is not fast at their pK_as as the protonation of the carboxylic groups is directly influenced by their surrounding environment such as the distribution of the carboxylic group units and the ionization state of adjacent units.[154-155] Rather, the microgels gradually swell with increasing pH solution.[76] Indeed, the swelling/deswelling behaviour is highly dependent on the type of the pH-sensitive comonomer, their distribution within the microgels and their concentration.[77, 107] When these anionic microgels are used to fabricate etalon optical devices, pH responsive devices whose color is dependent on solution pH are obtained. Furthermore, taking advantages of the pH responsive properties dependence with the nature and concentration of the pH sensitive comonomers, we prepared etalon optical devices composed of pNIPAm-*co*-5%MAAc, pNIPAm-*co*-10%AAc, pNIPAm-*co*-10%VAAc, or pNIPAm-*co*-30%AAc microgels that are expected to respond differently to variations in solution pH. Here, 4 sensor arrays each containing 64 etalons of 4 mm^2 were fabricated following the Doctor blade method. The fabricated etalons were hydrated overnight with DI water after which they were exposed to solutions with varying pHs. Moreover, based on our previous results suggesting that the presence of ions in solution could affect the etalon's response behaviour to pH, the solutions were prepared by adjusting the pH of DI water with NaOH or HCl and the ionic strength adjusted to 300 ppm using NaCl. In fact, McPhee *et al.* observed that the diameter of pNIPAm microgels at 25 °C (highly swollen) decreased in the presence of small amount of electrolyte (0.0001 M KCl) but no changes were observed when the concentration was increased up to 0.01 M.[59] Following, each etalon array was transferred to a Petri dish containing 10 mL of the desired pH solution and allowed to incubate for 20 minutes, after which they were placed inside of the 3D printed box #1 and photographs were captured. In addition, the 3D printed box was coupled with white LEDs as previous results showed a larger dynamic range in the CIE xy chromaticity coordinates of the etalons response to pH. Following, the sensor array was rinsed with DI water for 30 seconds and soaked in DI water for at least 30 minutes before being exposed again to another pH solution. The photographs were processed for color analysis by cropping the etalons and extracting their corresponding RGB values. Next, the RGB values were scaled to 0-1 by diving all their values by 255 and quality control was assessed. Here, the etalons were classified into 5 groups based on their chromaticity coordinates at pH 4 and pH 8 using *k*-means grouping algorithm. By performing this quality control, etalons that exhibit different colors and pH-response behaviour that are not easily visible are classified to different groups to increase the accuracy and precision of the pH measurements. For simplicity, only the groups that had etalons represented in all the sensor arrays and with high frequencies will be discussed. The changes in RGB values as a function of pH for the 4 sets of etalons are shown in **Figure 3.10(a-d)**. By inspection, it is apparent that among the 4 types of etalons investigated, those composed of pNIPAm-*co*-5%MAAc and pNIPAm-*co*-10%VAAc microgels showed distinct response behaviour in the 3 channels. In the case of pNIPAm-*co*-5%MAAc microgel-based etalons, their R value increased from pH 4 to 5 and decreased linearly from pH 5 to 8. The G value decreased linearly from 4 to 7 and increased from 7 to 8 while the B value increased linearly from 4 to 7 after which it decreased from 7 to 8. The distinct response behaviour in the 3 channels of these etalons makes them a potential candidate to be used as portable pH sensors. Interestingly, etalons composed of pNIPAm-*co*-10%AAc microgels showed significantly different responses to pH in solutions of 300 ppm IS compared with very low IS solutions (**Figure 3.4(b)**), which is in agreement with our earlier observations when measuring the pH of drinking water samples. The same phenomenon was observed for the 4 sets of etalons investigated. **Figure 3.10** (e) and (f) contains the changes in RGB values as a function of pH for etalons prepared with pNIPAm-*co*-5%MAAc and pNIPAm-*co*-10%VAAc microgels but in very low IS solutions. As noted, their responses significantly changed when compared with their pH responses in solutions where the IS was adjusted to 300 ppm (**Figure 3.10(a,c)**). However, when the IS of the solution was varied from 50 ppm to 500 ppm, their pH response behaviour had minimal variations, suggesting that there might be a range of IS where variations in salt concentration have minimal effect on their color change in response to pH. Furthermore, pNIPAm-*co*-10%AAc microgel-based etalons exhibited lower response sensitivities when the solution IS was adjusted to 300 ppm while the opposite was observed for etalons composed of pNIPAm-*co*-5%MAAc and pNIPAm-*co*-10%VAAc microgels. However, no significant changes in the RGB values were observed for pNIPAm-*co*-10%VAAc microgel-based etalons when the pH was varied from 7 to 8 as shown in **Figure 3.10(c)**. Therefore, pNIPAm-*co*-5%MAAc microgel-based etalons were a focus of subsequent investigations.

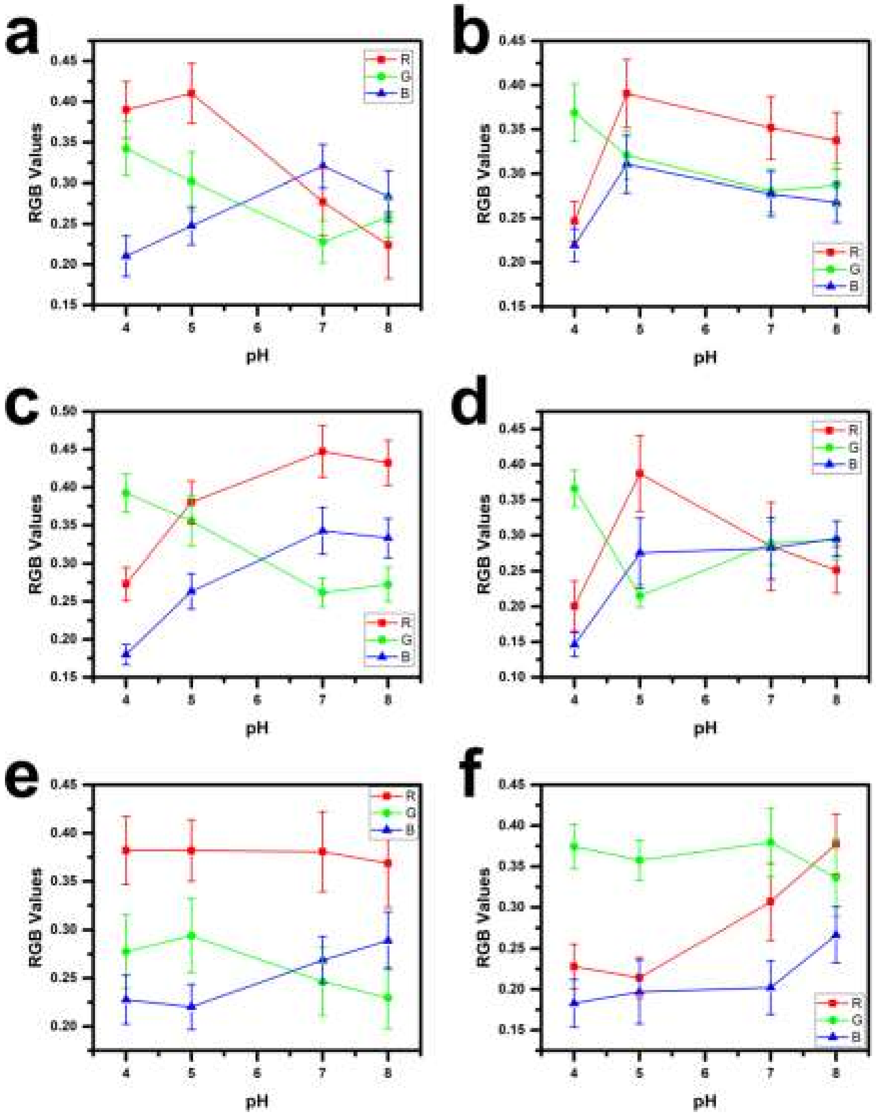

Figure 3.10 Changes in RGB values as a function of pH for etalons prepared using (a) pNIPAm-*co*-5%MAAc, (b) pNIPAm-*co*-10%AAc, (c) pNIPAm-*co*-10%VAAc, and (d) pNIPAm-*co*-30%AAc microgels in solutions with 300 ppm I.S adjusted with NaCl. (e) and (f) correspond to the changes in RGB values as function of pH for etalons composed of pNIPAm-*co*-5%MAAc and pNIPAm-*co*-10%VAAc respectively, but in very low IS solutions. Each data point corresponds to the average of the etalons in the group and the error bars are their standard deviations. The group frequencies were 21, 42, 32, and 31% for (a), (b), (c), and (d) respectively from a total of 1024 etalons.

3.3.5 Evaluation of the 3D Printed Box

We further investigated the performance of the experimental set up used for the digital image acquisition of the etalon devices. For this, images for three sensor arrays incubated in pH 4 and pH 8 solution was obtained using the 3D printed box #1 (with the camera angled at 10^o) and their RGB values as a function of their position in the sensor array are displayed in **Figure 3.11(a)**. The camera was angled in this set up to avoid the shadow of the camera on the etalons and the 10^o was chosen because the etalons showed a brighter color at this angle. The etalons in the sensor array was numbered from left to right in each row (8 rows in total). For instance, etalon #1 correspond to the etalon located on the top-left of the first row while the etalon #64 correspond to the last position of the row 8 bottom-right. As we can see from **Figure 3.11(a)**, the etalons located at the beginning of the sensor array show higher RGB values compared with the etalons located in the last row which was attributed to the angle of the camera as the first etalons were viewed with a slight different angle compared to the last etalons. Therefore, another box was fabricated with the camera angled at 0^o as shown in **Figure 3.2**. The camera was placed so its shadow would be located in the center of the sensor array, affecting only 4 etalons of the sensor array. When repeating the above mentioned experiment, but now using the new fabricated box #2, it was noticed that the patterns previously observed was significantly minimized as shown in **Figure 3.11(b)**. Following, digital images of the sensor array were obtained using both boxes at different positions by rotating the glass slide 90^o for 4 times, completing a full rotation of 380^o. Following, their RGB values were converted to XYZ tristimulus values and their xy chromaticity coordinates along with their luminosity values in the 4 rotation positions are displayed in **Figure 3.12** for both boxes. As noted, the chromaticity and luminosity values had minimal variation when rotating the sensor arrays for the new fabricated 3D printed box #2 as demonstrated by small changes in their xyY values as function of rotation position while for the box #1, significant variations could be observed as their xyY values either decreased or increased depending on the rotation position. Based on these results, the 3D printed box #2 was further used to evaluate the performance of the etalons to detect solution pH as it showed minimal effect on their RGB values.

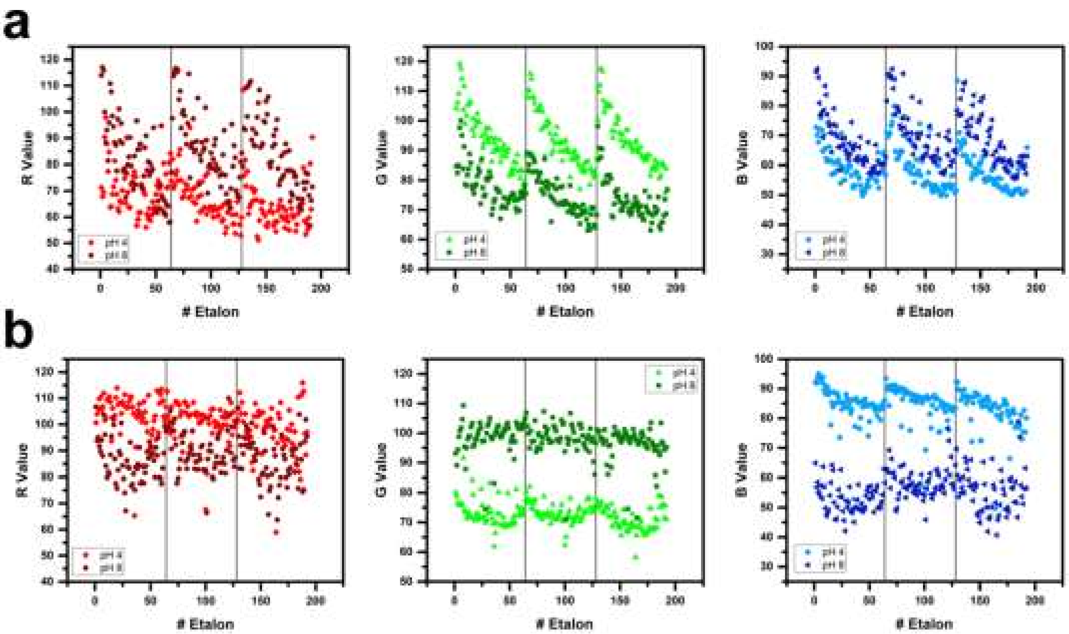

Figure 3.11 RGB values for etalons in pH 4 (lighter colors) and pH 8 (darker colors) obtained with the 3D printed box #1 (a) and #2 (b). Each graphic displays the RGB values for 3 sensor arrays as separated by the vertical lines. The number of the etalon corresponds to its position in the sensor array which was number based on the rows. Etalon #1 correspond to the first row position, left to right.

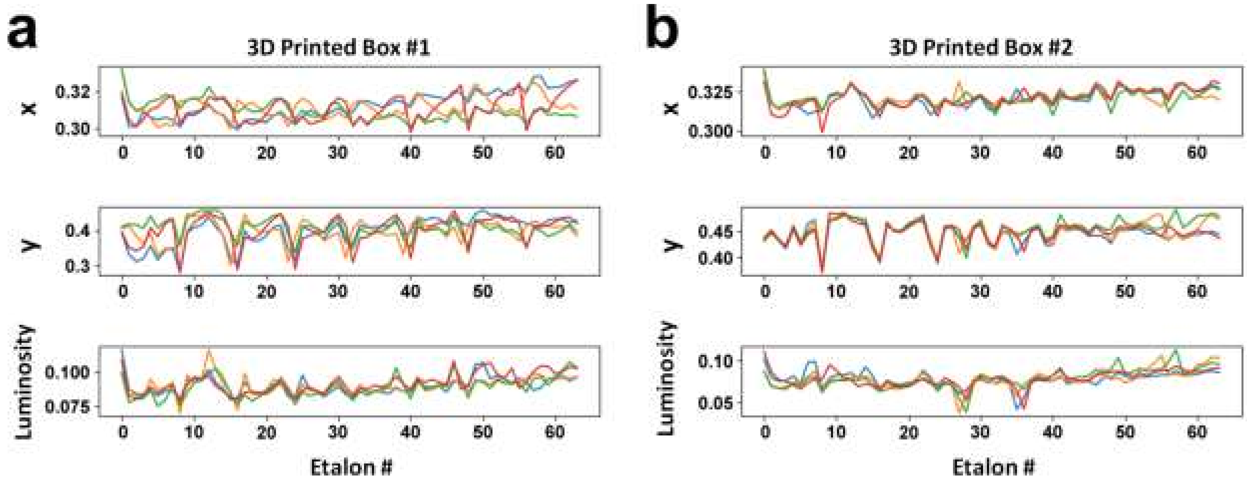

Figure 3.12 Chromaticity coordinates xy and luminosity values for 64 etalons one sensor array rotated at 90° for 4 times obtained using the 3D printed box #1 (a) and #2 (b). Each line represents xyY values at each rotation.

3.3.6 Colorimetric pH Measurements for pNIPAm-*co*-5%MAAc Microgel-Based Etalons in Complex Solutions

The color of the etalons composed of microgels containing 5% mol MAAc was characterized under different pH values. The etalon devices respond to solution pH by changing their color due to the protonation/deprotonation degree of the MAAc ionisable groups within the microgels that causes them to swell or shrink, changing the distance between the two reflective Au layers and leading to a color change. The amount of color change can be characterized by monitoring the shift in the reflectance spectrum peaks. However, the instrumentation is bulky, relatively costly and not suitable for field use. Thus, colorimetric measurements based on digital images seem to be the starting point to bring this technology to the next level. Here, 6 sensor arrays containing 64 etalons of 4 mm^2 were prepared following the Doctor blade technique discussed in Chapter 2, yielding a total of 384 etalon devices. Moreover, pNIPAm-*co*-5%MAAc microgels were chosen as their color change to pH was gradual and covered the full range of pH tested. The fabricated etalons were hydrated overnight with DI water and were exposed to solutions with pH varying from 4 to 8. The pH solutions were prepared by adjusting the pH of 300 ppm $CaCl_2$ solution with either NaOH or HCl. $CaCl_2$ was used as Ca^{2+} is always present and its concentration in drinking water is higher than the other cations such as Mg^{2+}, Na^{+}, and K^{+}. In addition, 300 ppm concentration was used considering the total dissolved solids (TDS) of drinking water, which can be as high as 400 ppm, after which the test of the water is compromised. Next, the digital images were cropped and their RGB values converted to XYZ tristimulus values. Again, the etalons were classified into 5 groups using *k*-mean clustering algorithm. Grouping was determined by their chromaticity coordinates at pH 4 and 8, given by their vector (pH4x; pH4y; pH8x; pH8y). The results of the grouping is shown in **Figure 3.13(a,b)** and as we can see, each etalon is assigned to one specific group and each group is clustered (centered) for both pH 4 and 8. Following, the etalons in each group were randomly divided into two groups, a training group with $n_{etalons}$ = 278 (80%) to generate the reference models and a validation group with $n_{etalons}$ = 69 (20%) to independently test the reference models. The chromaticity coordinates as a function of pH for the two most populated groups are shown in **Figure 3.13(c,d)**. The solution pH for each group was predicted using a linear regression of the chromaticity coordinates, a + bx + cy, where each group had its own model. The results can be found in **Table 3.1**. The mean absolute error (MAE) was calculated for the model, which is the average of the differences between the measured pH and the predicted pH for the etalons used in the training. In addition, the MAE was calculated for the validation group, which in this case is the average of the differences between the predicted pH for the etalons in the validation group (not used for the training) and the measured pH. Furthermore, the etalons in the validation group was shuffled 100 times (20% of the etalons were randomly selected 100 times) to obtained a closer approximation of the true MAE. As shown, the MAEs for the etalons used in the training were slightly lower than the MAE for the etalons in the testing group. The lowest value of the MAE was 0.24 pH units while the maximum value was 0.31 pH units between the 3 most populated groups.

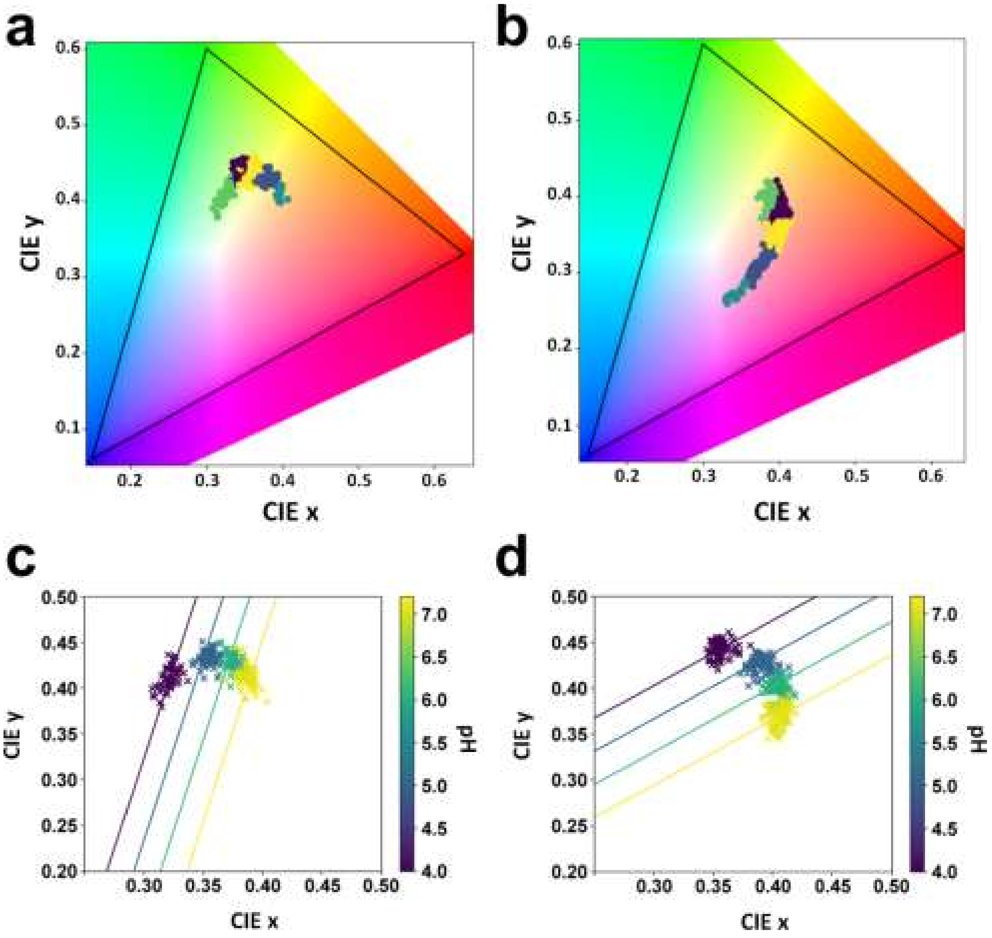

Figure 3.13 CIE xyY color space showing the xy chromaticity coordinates for the pNIPAm-*co*-5%MAAc microgel-based etalons at pH 4 (a) and 8 (b) that were classified into 5 groups represented by different colors and the pH responses for the green (c) and yellow (d) groups presented in (a) and (b).

Table 3.1 Frequency of etalons in each group and their mean absolute errors

	f_{training} (%)	MAE$_{\text{training}}$	f_{test} (%)	MAE$_{\text{test}}$
Group 1	34	0.27	22	0.31
Group 2	5	0.28	4	0.29
Group 3	20	0.26	26	0.26
Group 4	15	0.24	16	0.35
Group 5	26	0.23	32	0.24

We further investigated the concentration range where the reference models created at 300 ppm $CaCl_2$ could still be used to predict the solution pH with minimal effect on the accuracy of the measurements. For this, 6 sensor arrays were exposed to pH 4 and 8 solutions with the concentration of $CaCl_2$ varying from 50 to 600 ppm. For simplicity, the results for one sensor array are displayed in **Figure 3.14**. At low pH (**Figure 3.14(a)**), the color of the etalons showed more variations due to the changes in the IS than at high pH. For 50 and 600 ppm, the data starts deviating from center where most of it is concentrated. At high pH, there is an overlap of the chromaticity coordinates for the etalons under different $CaCl_2$ concentration. However, it does not imply that the microgels are not responding to variations in the solution ionic strength but the responses are not sufficiently high to produce a chromatic color change. For more details of the etalons responses to solution ionic strength, reflectance spectrum measurements should be carried but it is not relevant to this investigation as our intention is to perform colorimetric measurements of the etalons. The results here suggest that the reference models generated at 300 ppm of $CaCl_2$ concentration could be applied to predict the solution pH for water samples with TDS ranging from 50 to 600 ppm as they did not show significant variation in their chromaticity coordinates in this concentration range.

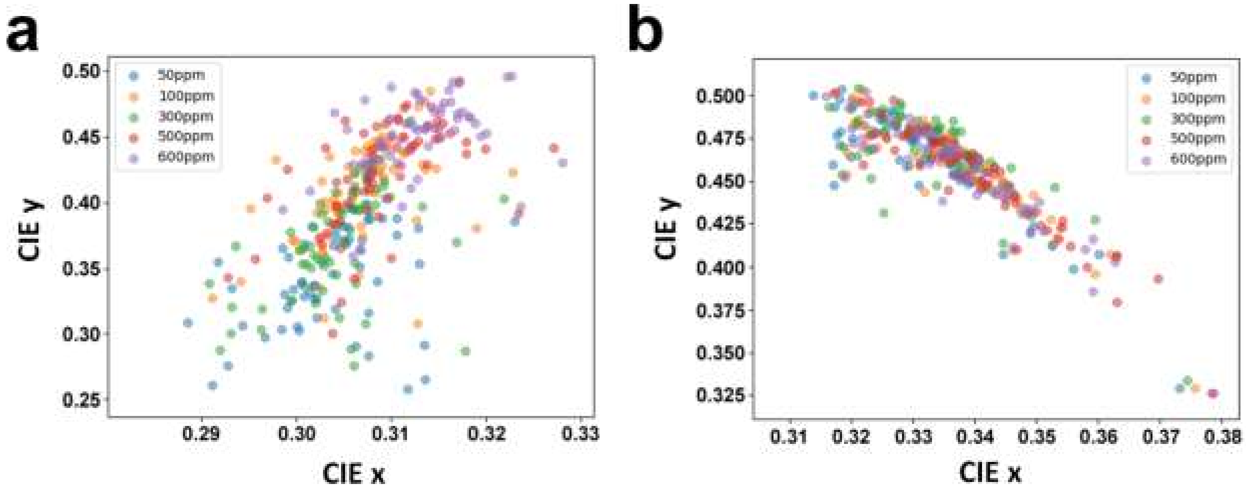

Figure 3.14 Chromaticity coordinates for pNIPAm-*co*-5%MAAc microgel-based etalons at pH 4 (a) and pH 8 (b) under different $CaCl_2$ concentrations. Each concentration is represented by 64 etalon devices.

Next, we investigated how the nature of the cation affects the accuracy of our measurements. For that, 6 sensor arrays were also exposed to pH solutions varying from 4 to 8 with the ionic strength adjusted to 900 ppm using NaCl, considering that the reference models were generated in solutions with ionic strength of 900 ppm adjusted with $CaCl_2$. Furthermore, we acknowledge that drinking water composition varies from place to place and in most cases, the concentration of bicarbonates (HCO_3^-) is higher than the concentration for cations. Nevertheless, we believe that cations have a greater impact on anionic microgel's response to pH than anions due to the negatively charged units in the microgels when the solution pH > pK_a of the ionisable groups. The digital images were processed following the same procedure as described above and the comparison of the xy chromaticity coordinates for 347 etalons at pH 4 and 8 with the IS of the solutions adjusted using NaCl or $CaCl_2$ is shown in **Figure 3.15**. At low pH, the color of the etalons did not vary significantly when using NaCl or $CaCl_2$ while at high pH, there was visible changes in their chromaticity coordinates. In this case, $CaCl_2$ resulted in higher xy values than NaCl.

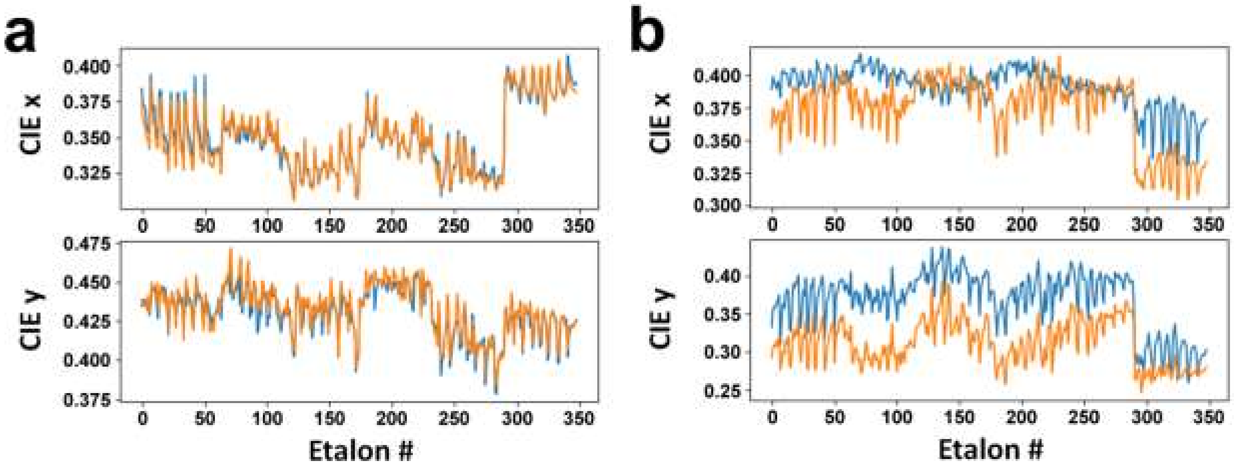

Figure 3.15 Comparison of the chromaticity coordinates for etalons composed of pNIPAm-*co*-5%MAAc microgels in pH 4 (a) and 8 (b) where the IS of the solutions was adjusted to 900 ppm using NaCl (orange) and $CaCl_2$ (blue).

To further investigate how this variation affects the accuracy of the pH measurements, we applied the reference models generated in the presence of $CaCl_2$ at 20 ^{o}C to predict the pH of the solutions where the IS was adjusted using NaCl. Again, 6 sensor arrays and 4 pH solutions (4, 5, 7, and 8) were used for the calculations. The MAE for the measurements can be found in **Table 3.2**. As is apparent, the MAE in each group almost doubled for the pH measurements in solutions containing NaCl compared with the MAE for the pH measurements done in solutions containing $CaCl_2$. Although this is an extreme case where the concentration of NaCl is relatively high, it suggests that the accuracy of the measurements can decrease by half when dealing with more complex solutions.

Table 3.2 Comparison of the MAE for the predicted pH of solutions containing NaCl and $CaCl_2$

	MAE_{NaCl}	MAE_{CaCl_2}
Group 1	0.65	0.31
Group 2	0.60	0.29
Group 3	0.39	0.26
Group 4	0.47	0.35
Group 5	0.46	0.24

Following, as pNIPAm-based microgels are inherently thermoresponsive, we further investigated the effect of temperature variations on the pH measurements. Here, 4 sensor arrays were incubated in pH 4 and 8 solutions at ~5, 15, 20, 25, and 35 °C for 20 min and digital images were obtained using the 3D printed box #2. In addition, the pH solutions were prepared with 300 ppm $CaCl_2$ concentration. The results are displayed in **Figure 3.16**. As we can see, the etalons showed significant color changes within the temperature range studied. At low pH (**Figure 3.16(a)**), the temperature-induced color change was significantly higher than at high pH and the responses closed a complete circle in the CIE xyY color space. However, at high pH, the color change was not as abrupt but still significant. The reason for this larger color change at low pH is due to the ionization of the MAAc groups that are protonated at pH 4. At this pH, the undissociated carboxylic groups have little effect on the thermoresponsive properties of pNIPAm.[156] At high pH, however, the temperature-induced conformational change of the microgels is affected by the Coulombic repulsion of the localized negatively charged groups in the microgels network and the increase in osmotic pressure inside of the microgels, making them swollen and shifting their LCST to higher temperatures. This phenomenon has already been documented by others when studying the thermoresponsive properties of anionic microgels under high and low pH.[76, 118, 156] Nevertheless, the etalons also showed significant color change in response to variations in temperature at high pH, which is attributed to the ionic strength of the solution. Compared with salt-free solutions where the charge density of the microgels increases with pH, increasing the ionic strength to ~900 ppm using $CaCl_2$ decreases the Debye screening length due to the screening of the negative charges by the ions in solution, reducing the repulsive electrostatic forces between the negatively charged carboxylic groups within the microgel network.[77] As a result, the microgels are freer to collapse/swell as the temperature is increased or decreased which is translated as color changes when the microgels are assembled into an etalon structure.

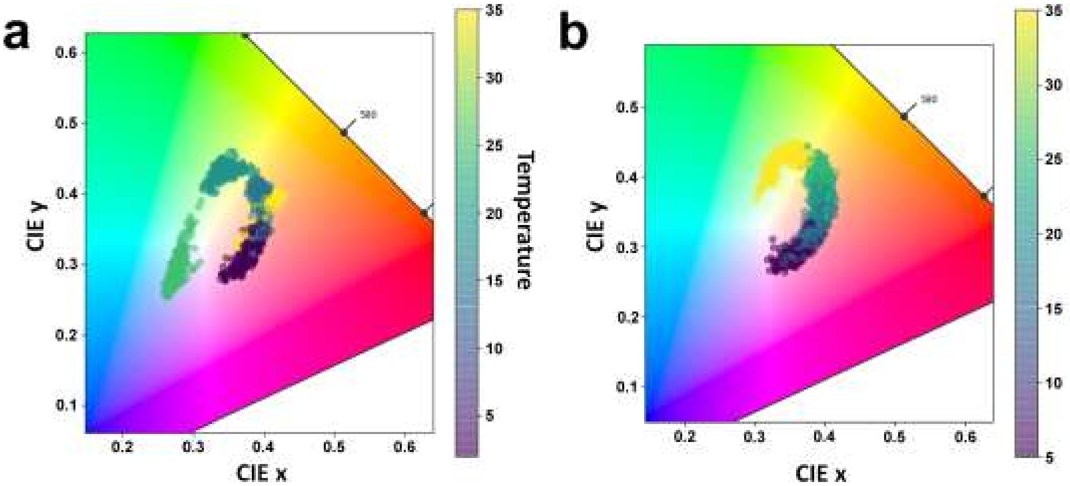

Figure 3.16 Temperature responses for etalons fabricated with pNIPAm-*co*-5%MAAc microgels at pH 4 (a) and 8 (b).

The reference models obtained in 300 ppm $CaCl_2$ concentration at 20 °C were again tested to predict the pH of the solutions at 15 and 25 °C. The results are shown in **Table 3.3**. As we can see, the MAEs for both temperatures are significantly high, suggesting that for optimal pH measurement, the solution temperature should be maintained at around 20 °C. Interestingly, the MAE for the predicted pH 8 at 15 °C is significant slower compared with the other MAEs, especially for group 2 and 3, presumably due to the temperature that is considerably below pNIPAm's LCST where the microgels are highly soluble and swollen. At this low temperature, the electrostatic repulsion of the carboxylic groups when the pH is increased, even though highly screened, seems to dictate the swollen state of the microgels, suggesting that the etalons are able to predict the solution pH at low temperatures when the solution pH is higher than the pK_a of the MAAc groups. Moreover, the temperature response displayed in **Figure 3.16(b)** indicates that solution temperature could be predicted if the solution pH is known.

Table 3.3 MAE for predicted pHs at 15 and 25 °C using the linear regression models obtained in 300 ppm $CaCl_2$ at 20 °C

	T = 15 °C		T = 25 °C	
	pH 4	pH 8	pH 4	pH 8
Group 1	2.2	0.81	2.1	2.6
Group 2	2.5	0.35	2.5	2.3
Group 3	2.7	0.37	1.1	2.1
Group 4	2.8	0.50	0.6	1.9
Group 5	1.8	1.6	0.8	2.6

Finally, the reference models for each group were used to predict the pH of drinking water samples. The sensor arrays were exposed to 3 different drinking water samples for 20 minutes and digital images were obtained using the 3D printed box #2 coupled with white LEDs. The water sample 1 was collected from the public water system and the water sample 2 and 3 were from store bought bottled water. The pH values measured with a pH meter for the water sample 1, 2 and 3 were 7.6, 5.7, and 7.0 respectively while their TDS values were 184, 18, and 290 ppm respectively as measured using a conductivity meter. In respect to their conductivity, they showed to be 375, 36, 591 µS/cm respectively. The MAE for each group and for each sample can be found in **Table 3.4**. The MAEs for the water sample 1 were similar to the MAE calculated for the etalons in the testing group (see **Table 3.1**) while the MAE for the water sample 2 and 3 were significant high. The water distributed to the city of Edmonton comes from the North Saskatchewan River and is moderately hard, containing around 165 mg/L of $CaCO_3$ and a yearly average pH of 7.8 with a average conductivity of 350 µS/cm. This information was collected from EPCOR's website (www.epcor.com) under Edmonton Water Quality Reports, accessed on 2020-03-06. This explains the low MAE in the predicted pH for the water sample 1 as the water composition is mainly composed of Ca^{2+} and bicarbonates ions with the concentration in the range of 50 to 600 ppm. However, the water sample 2 and 3 showed significantly high MAE which is attributed to the significant low TDS of the water sample 1, which is out of the concentration range that the reference models can be used, and the relative low Ca^{2+} concentration in the water sample 2.

Table 3.4 MAE for the drinking water samples using the reference models

	$MAE_{Sample\ 1}$	$MAE_{Sample\ 2}$	$MAE_{Sample\ 3}$
Group 1	0.39	0.80	0.71
Group 2	0.26	0.90	0.90
Group 3	0.15	0.97	0.66
Group 4	0.34	1.0	1.1
Group 5	0.30	0.72	0.67

3.4 Conclusions

In this chapter, we explored the possibility of using the etalon devices as portable pH sensors. The ability of the etalons to detect solution pH based on colorimetric measurements was investigated and the limits of the technology were explored. We found that the angle of the camera was extremely important for precise and accurate measurements. Furthermore, the optimal sample exposure time was found to be between 20 to 40 min as the color of the etalons were not completely uniform before 20 minutes and their color drastically changed after 60 minutes. Moreover, we observed that the etalons response to pH in very low IS solutions were significantly different when ions were present in the system. Thus, the color changes in response to pH for 4 sets of etalons were characterized at 20 ^oC in solutions containing 300 ppm of $CaCl_2$ concentration. Among those, the etalons composed of pNIPAm-*co*-5%MAAc microgels showed promising results and was chosen for further investigations. The impact of the experimental set up on the color of the etalons was also explored. We found that the 3D printed box with the camera set at 0^o showed minimal effect on their color. In addition, using white LEDs to capture pictures gave a larger range for the color change. Following, reference models were generated at 20 ^oC, 300 ppm of $CaCl_2$ concentration in a pH range of 4 to 8. The models were validated against 20% of the etalons that were not used to create the curves and the MAE of the pH measurements was found to be around 0.3 pH units. Next, we investigated how variations in salt concentration, the nature of the cations, and variations in temperature impacted the pH measurements. We observed that the models could be applied to a concentration range of 50 to 600 ppm and that exchanging $CaCl_2$ to NaCl, the MAE was increased to 0.4-0.6 pH units depending on the group of etalons. Furthermore, the temperature was also an important parameter affecting the color of the etalons and should be kept near 20 ^oC for optimal pH measurements. Finally, we applied the reference models to predict the pH of drinking water samples which gave a MAE of 0.15 and 0.4 pH units for the most populated groups.

Chapter 4

Detecting Changes in Solution Ionic Strength using pNIPAm-*co*-10%AAc Microgel-Based Etalon Optical Devices – In Collaboration with SolarDew International

4.1 Introduction

Access to safe drinking water is a basic human right and essential to maintain good health, productive lives and hence, crucial for economic growth and development of a country. The United Nations (UN) has declared that access to safe drinking water is a fundamental step towards improving living standards globally and included it as one target of the Sustainable Development Goals (SDGs) to be achieved by 2030. Despite considerable effort over the past years, 785 million people still lack access to basic drinking water services and 2.2 billion people lack access to safely managed water services according to World Health Organization (WHO).[157] The goal to provide universal access to safely managed drinking-water services has proven to be elusive and slow. Contaminated drinking water is estimated to cause 829 000 deaths each year and it is linked to the transmission of preventable diseases such as diarrhoea, cholera, dysentery, and hepatitis A.[157] With population growth, climate change, and urbanization, it is estimated that half of the world's population will be living in water scarce areas by 2025.[157] Water covers around 70% of the Earth's surface, but most (97.2%) of it is saline and undrinkable. For many, the only available water is contaminated, saline, or both. Therefore, there is a need for a simple and inexpensive means of creating safe drinking water from diverse water sources. SolarDew International is developing a new solar-based water purification technology that can desalinate and purify saline water. The technology uses solar energy as a power source and purifies seawater through a process called pervaporation using non-porous membranes. Briefly, the water inside of the SolarDew panels is heated by the sun and evaporates, passing through the patented membranes, and leaving behind various contaminants, e.g., bacteria, viruses, heavy metals, and salts. The clean water condenses on one side of the membrane and is collected as distilled water with pH 9 and conductivity of < 10 μS/cm. The purified water is then re-mineralized with a combination of calcium and magnesium to improve taste and meet water quality standards. After the purified distilled water is extracted from the system, concentrated brine drains automatically from the panel. The quality of the membranes is key to this process working efficiently, and if a membrane fails by cracking, this can lead to the drinking water being contaminated. Importantly, when a membrane fails, the drinking water will increase in conductivity/ionic strength, which can potentially be detected. While the change in water ionic strength will be too low to taste, analytical tools need to be used to detect the increase in ionic strength in a continuous fashion such that failed membranes can be replaced quickly. The two main types of water conductivity sensors are commercially available, i.e., toroidal (inductive) conductivity sensors.[158-159] Contacting conductive sensors measure the conductivity of the water using two metal electrodes, where an alternating voltage is applied between the two electrodes immersed in the water sample and the resulting ionic current is measured. The resistance is then measured based on the measured ionic current and related to the solution conductance. Toroidal conductivity sensors use two wire-wound metal toroids encapsulated in a corrosion-resistant plastic case. An alternating voltage is applied to one of the toroid which causes an ionic current in the solution that is sensed by the second toroid as a magnetic field, inducing a current in the second toroid that is directly proportional to the solution conductance. Even though these conductive sensors are portable, practical, have a wide measurement range, and measure the conductivity with high accuracy, they require calibration steps, are powered by batteries, can be hard to integrate into other systems and cannot be used to measure the conductivity of solutions in real-time. Furthermore, for some applications, there is no need for such accuracy and complexity. The SolarDew panels are intended to be used in remote areas where electricity may not be available thus the technology requires no electricity to operate and the introduction of batteries is seen as potential hazard to the environment and an additional cost. In addition, the desalination technology is intended to be used by anyone with or without scientific background so colorimetric sensors are preferred where the color change should occur between two contrasting colours as it should be easy for the user to identify. Therefore, there is a need to develop a low cost sensor to measure the ionic strength or conductivity of the product water that undergoes a visual color change at a specific value that does not require calibration steps and the changes in the conductivity can be easily interpreted. In doing so, it can confirm the quality of the water and thus reassure the user that the water being produced is safe to drink. The technology must be robust, low cost and have no electrical parts in order to perform optimally.

Stimuli-responsive hydrogel particles (microgels) undergo changes in physical and/or chemical properties in response to stimuli such as pH, ionic strength, light, and temperature.[160-161] Poly (*N*-isopropylacrylamide) (pNIPAm)-based microgels have been extensively studied due to their inherent thermoresponsive properties.[56] Microgels composed of pNIPAm are known to expel > 90% of their solvating water by collapsing at temperatures >32 °C and reswelling when the temperature is decreased to <32 °C. This transition is reversible over many cycles and the temperature at which it occurs is commonly referred to as the lower critical solution temperature (LCST). PNIPAm-based microgels can be synthesized with various sizes depending on the sysnthesis conditions and can be easily modified (chemically) to respond to other stimuli by incorporating functional comonomers into them at the time of synthesis.[58, 66, 69, 162-163] For instance, microgels that are temperature and pH responsive can be prepared by incorporation of a weak acid or base into pNIPAm-based microgels. A common comonomer used to add pH responsivity to pNIPAm microgels is acrylic acid (AAc), which has a pK_a of ~4.25.[107, 130] These microgels show pH responsive properties due to the ionization of the carboxylic groups that causes the polymer to swell due to the charge-charge repulsion. In addition, when pNIPAm-*co*-AAc microgels are in a solution with pH > pKa of the AAc, the localized negative charges increase their osmotic pressure, causing them to further swell and easily attract positively charged ions.

The Serpe Group has fabricated microgel-based etalon devices by placing a monolayer of pNIPAm-based microgels between two thin reflective Au layers.[79] The group has done extensive studies on these devices since we first reported them in 2011.[74, 78, 80, 109] PNIPAm microgel-based etalons can be fabricated by doctor blade technique (see Chapter 2) where a concentrated solution of pNIPAm-based microgels is spread on the surface of a Au coated (typically 15 nm) glass substrate and allowed to air-dry. Following, the excess microgels that are not directly bound to the Au surface is removed by extensively washing the substrates with deionized (DI) water and dried with N_2 gas before depositing a second layer of Au with a thickness of 5-25 nm. The structure of these optical devices is illustrated in **Figure 4.1**. The devices exhibit visual color, which is a direct result of light interference within its structure. Here, the microgel layer acts as a dielectric layer, and the Au layers act as reflective mirrors. When light impinges on the device, some of the light is reflected and some passes to the cavity (microgel layer) where it resonates and undergoes constructive and destructive interference, resulting in a reflectance spectra with a reflectance peak/or peaks at specific wavelengths (λ) that can be predicted from Equation (4.1):

$$\lambda m = 2d\eta cos\theta \qquad (4.1)$$

Where m is the peak order (an integer), η is the refractive index of the microgels, d is the distance between the two Au mirrors, and θ is angle of incident light. As a result, the position of the reflectance peaks (and the device color) depends on the distance between the two Au mirrors, which in turn is controlled by the hydration state of the microgel layer. When in water, the microgels in the etalons exchange solvent molecules and ions with the external solution from the side and through the porous top Au layer, similar to Donnan membrane equilibrium.[73] Changes in the external solution ionic strength would cause changes in the osmotic pressure inside and outside of the microgels, causing them to shrink or swell.[164-166] In addition, the presence of cations can screen the negative charges of anionic microgels, reducing their electrostatic repulsion and causing them to shrink.

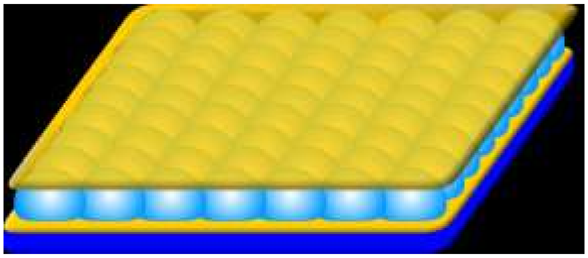

Figure 4.1 Illustration of the pNIPAm-based etalon structure, which consists of a monolayer of highly packed microgels (blue particles) placed between two reflective Au layers (yellow) fabricated on a glass substrate (dark blue bottom).

In this research project, the etalons were used to monitor and detect small changes in the ionic strength of purified water (pH 9 and conductivity of < 10 µS/cm) being produced by the SolarDew panels. The etalons seemed to be a great candidate for this as the technology does not require any electrical parts and the color change can be easily visualized by the naked eye. For this, we evaluated the performance of etalons composed of pNIPAm-*co*-10%AAc microgels to detect small variations in solution ionic strength. In addition, a 5 nm Au-top layer was used instead of the 15 nm top Au layer commonly used to achieve faster response times. This is because the thin Au is more porous than thick Au, allowing the solution and the etalon to reach equilibrium quickly. Increasing the porosity of the top Au layer increases the number of sites where the exchange between solvent molecules and ions occurs, resulting in faster responses. We characterized the color change of the etalons upon NaCl exposure using a reflectance probe over a range of 0.9 to 200 mM. The sensor initially showed a green color in pH 9 and turned red upon exposure to small amounts of NaCl. Its color continued to be red up to 50.5 mM (3500 ppm) and then goes back to the green color initially observed. In addition, the usability of the sensors was demonstrated by measuring their intra-day and inter-day precisions. The sensor showed to be highly stable over many cycles of NaCl exposure. The temperature range at which the sensors showed to be green was found to be 17 – 35 ^{o}C and the resetting time was decreased by exposing the sensors to pH 3 solution.

4.2 Experimental Section

4.2.1 Materials

N-isopropylacrylamide (NIPAm) was obtained from TCI (Portland, Oregon) and purified by recrystallization in hexane (ACS reagent grade, EMD, Gibbstown, NJ) before use. N,N’-

methylenebisacrylamide (BIS) (99%), acrylic acid (AAc) (99%), ammonium persulfate (APS) (≥98%), sodium chloride (NaCl), sodium hydroxide (NaOH) were purchased from Sigma-Aldrich (Oakville, Ontario) and were used as received. Whatman #1 paper filters were obtained from GE Healthcare (U.K.). Deionized (DI) water with resistivity of 18.2 MΩ·cm was obtained from a Milli-Q Plus system and was used for all experiments. A pH meter (JENCO 6173, San Diego, CA) coupled with ROSS micro pH electrode (Thermo Scientific, Markham, ON) was used to adjust the pH of the solutions. Glass substrates (25 x 25 mm) with thickness of 0.13 – 0.17 mm was obtained from Fisher (Ottawa, Ontario). Cr flakes (99.999%) and Au (99.99%) were purchased from ESPI (Ashland, OR) and MRCS Canada (Edmonton, AB), respectively.

4.2.2 Synthesis of pNIPAm-*co*-10%AAc Microgels

PNIPAm-*co*-10%AAc microgels were synthesized via free radical precipitation polymerization following a previously published procedure. In short, 59.5 mmol of NIPAm and 3.515 mmol of BIS were dissolved in 495 mL of DI water in a 1 L beaker. The mixture was stirred for 30 min and filtered through a 0.2 μm syringe filter into a 1 L 3-neck round bottom flask which was fitted with a reflux condenser, nitrogen gas inlet, thermometer, and stir bar. The solution was purged with N_2 gas while heating to 75 °C over ~1 h, after which 7.15 mmol of AAc was directly added using a micropipette. The reaction was then initiated by injecting in one aliquot of a solution of ammonium persulfate (APS) (1 mmol). The reaction was allowed to proceed for 4 h at 75 °C, under N_2 atmosphere. Following, the resulting microgel suspension was allowed to cool down overnight at room temperature and then filtered through a Whatman #1 paper filter to remove large aggregates formed during the polymerization reaction. Next, the microgels were purified via centrifugation and resuspension process in DI water 6 times. In the last centrifugation, the supernatant was removed and a highly concentrated microgel solution was obtained. Finally, its concentration was adjusted by transferring 100 μL of the microgel solution to a microscope glass slide as a single droplet, quickly positioning it vertically at 130° and recording the distance that it slid for 1 min. DI water was added or removed until it reached 0.15 to 0.3 inches in 1 min.

4.2.3 Etalon Fabrication

Etalons of 9 mm^2 were fabricated by following the doctor blade method described in details in Chapter 2. Briefly, cover glasses (625 mm^2) were cleaned with etalon and DI water using an ultrasonic cleaner (Fisher Scientific, FS20). Following, the glass substrates were coated with 2 nm Cr and 15 nm Au using a thermal evaporator system (Torr International Inc., New Windsor, NY). The deposition rates were 0.19 Å s^{-1} and 0.17 Å s^{-1} for Cr and Au respectively and Cr was used as adhesion layer. In addition, a metal mask containing 25 squares of 9 mm^2 was placed in front of the cover glasses to obtain 25 etalons of 9 mm^2. Next, the Cr/Au coated glass substrates were placed in the substrate holders of a custom-built painting platform (see **Figure 2.2**, Chapter 2) and the microgel solution was spread on their surface with the assistance of a microscope glass slide (see **Scheme 2.1**, Chapter 2). The glass substrates were transferred to a hot plate set at 35 °C and the microgel solution was allowed to air-dry for 1 h. The excess of microgel was then removed by extensively rinsing the glass substrates with DI water. Following, the glass substrates were incubated in DI water overnight before being rinsed and dry with N_2 gas. The dried glass substrates were placed inside the thermal evaporator and a second (top) layer of 2 nm Cr and 5 nm Au were deposited. Again, a metal mask was placed in front of the glass substrates before the depositions. It is important to mention that the deposition rate for Cr an Au was kept constant for all depositions to obtain reproducible films. Finally, etalons of 9 mm^2 were obtained after the second Cr/Au layer and were incubated overnight in DI water before being used. Furthermore, a quality of control was performed where only those etalons that reached a green color at pH 9 were used for the experiments.

4.2.4 Reflectance Spectra Measurements

Reflectance measurements for the etalons in response to increasing concentrations of NaCl were done using a Red Tide USB650 spectrometer (detection range of 360 to 1100 nm), a LS-1 tungsten light source (spectral range of 360 to 20000 nm), and a reflectance probe obtained from Ocean Optics (Dunedin, FL). A solvent blank solution was prepared by adjusting the pH of DI water to 9 using NaOH (0.1 M) and a pH meter, which was then used to prepare a solution of 1 M NaCl. The etalons were incubated overnight in the blank solution and only those that showed a uniform green color were selected to be tested. For the measurements, an etalon was transferred into a custom-built temperature controlled chamber containing 13 mL of the blank solution and a small stir bar. Following, the chamber was closed, the temperature was set to 25 ^{o}C and the reflectance probe was inserted into the chamber through a small aperture located on top of the chamber's lid. The probe was then immersed in the blank solution and its distance from the etalon was adjusted for optimal signal. Reflectance spectra were collected using Ocean Optics Spectra Suite Spectroscopy Software over a wavelength range of 450-950 nm. After stabilization, e.g. the spectrum was no longer shifting after 15 minutes, increasing volumes of the 1 M NaCl solution was successively added using a micropipette. We ensured that the reflectance spectrum was stable (no longer shifting after 15 min) before each successive addition and they were recorded only after stabilization. This procedure was repeated for 4 times using 4 different etalon devices. Temperature control experiments were done using the same custom-built temperature controlled chamber as described above, but instead of adding NaCl, the temperature was increased from 2 to 35 °C.

For the reusability experiments (intraday and interday), a closed flowing system was built to mimic the real system where the sensors will be placed and it is depicted in **Scheme 4.1**. Here, the etalon was inserted into a closed chamber fitted with an inlet and outlet tubes and the reflectance probe. Two peristaltic pumps were used with the same flow rate to add (peristaltic pump A) and remove (peristaltic pump B) the solutions, creating a continuous flow over the etalon device. The etalon was first stabilized with the blank solution using the closed system. After stabilization, the reflectance spectrum was recorded and a fixed amount of NaCl was added to the centrifuge tube. After stabilization with the NaCl solution, another spectrum was recorded and the NaCl solution in the centrifuge tube was replaced with the blank solution. The etalon was again allowed to stabilize in the blank solution before recording the reflectance spectrum. This process was repeated 10 times in one day and 30 times during 30 days, being exposed to NaCl once every day.

The reflectance spectra were analyzed by assessing the change of the peak position centered at ~508 nm. For this, a Gaussian was fit to the reflectance spectra and the center of the peak Gaussian was recorded to obtain an objective measure of the peak position.

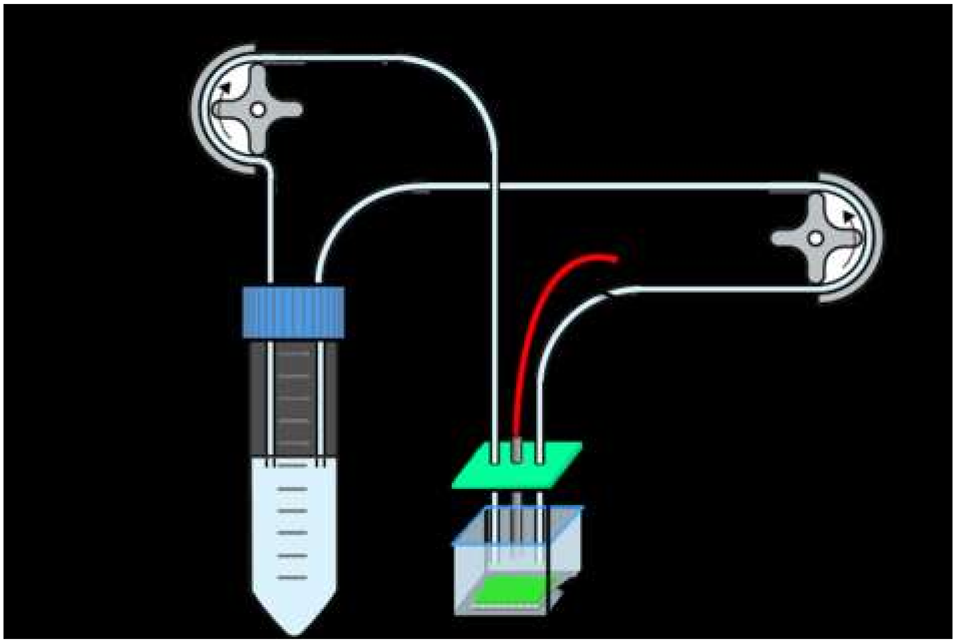

Scheme 4.1 Illustration of the closed flowing system used for the intra-day and day-to-day reusability tests.

4.3 Results and Discussion

pNIPAm-*co*-10%AAc microgels were chosen to fabricate the etalon devices in this work due to their higher sensitivity towards small changes in solution ionic strength, which we will discuss in detail in the next Chapter, and due to their green appearance in pH 9 solution. When using colorimetric devices for sensing applications that will be used by untrained personnel, it is important to consider the psychology of the colors. Whether obvious or not, humans tend to associate colors with emotions.[167-168] For instance, red is a primary color often associated with love, passion, and can stimulate people to make quick decisions. However, it can also signify danger or warning. On the contrary, green is a secondary color and often associated with nature, healing, hope, and is usually used to indicate safety. As we intend to use the etalon devices for water quality control, the use of a red-related colored etalon to indicate that the water being produced in safe to drink would go against these conceptions and associations. Thus, the use of a green-related color to indicate safety is one important parameter to be considered. PNIPAm-*co*-10%AAc microgels were synthesized via free radial precipitation polymerization and showed a hydrodynamic diameter of 919 ± 18 nm in DI water as measured by DLS. Furthermore, they showed to be highly dispersible in water and spherical as shown in **Figure 4.2(a)**. From these microgels, etalons of 9 mm^2 were fabricated on 625 mm^2 cover glasses using a metal mask that yielded 25 etalons per substrate as shown in **Figure 4.2(b)**. After the fabrication process, the etalons were subjected to a quality control criterion where only those that showed a uniform green color in the blank solution (pH 9) were selected for further testing.

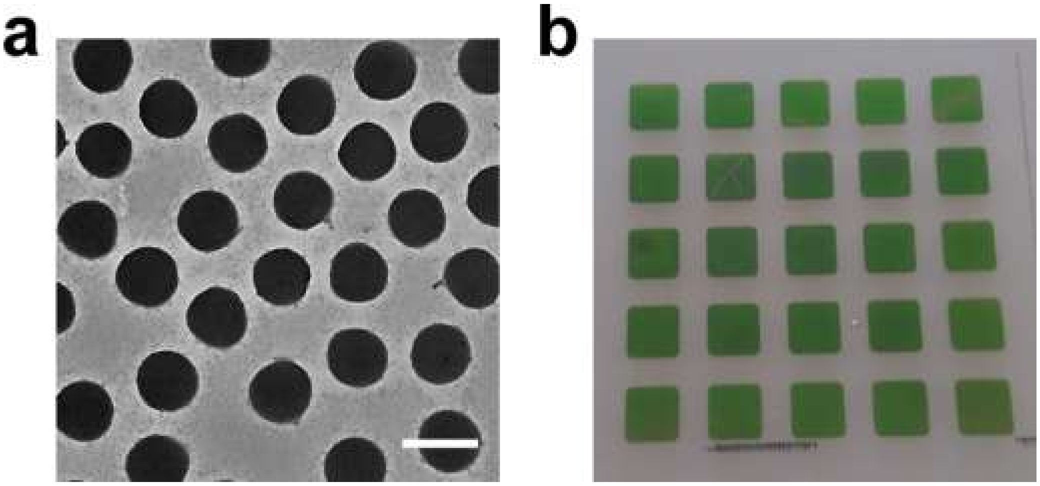

Figure 4.2 (a) TEM images of the pNIPAm-*co*-10%AAc microgels in the dried state and (b) the resulting etalons of 9 mm^2 constructed from them in the blank solution. Scale bar in panel (a) represents 0.5 μm.

The glass substrate was cut into 25 pieces to obtain individual etalon devices and their reflectance spectrum in the blank solution showed two distinct peaks at ~508 and ~760 nm as shown in **Figure 4.3(a)**. They were then individually exposed to increased concentrations of NaCl, from 0.9 to 200 mM, and the peak at ~508 was chosen to track their color change. The exchange of solvent molecules and ions with the microgels is believed to occur through the porous top Au layer and from the sides of the etalons. As can be seen from **Figure 4.3(b)**, the sensors are initially green and upon exposure to very small amount of NaCl (0.9 mM), their color quickly changed to red and a red shift (shifting to higher wavelengths) of the peaks in the reflectance spectrum was observed. The red shift is caused by the swelling of the microgel layer, increasing the distance between the two reflective Au layers. Interestingly, the microgels are expected to shrink when the solution IS is increased. However, the microgels continued to swell up to 3.4 mM of NaCl, after which no significant change was observed up to 5 mM. Following, at concentrations > 5 mM, a continuous blue shift (shifting to lower wavelengths) was observed which is caused by the microgels shrinking. Moreover, its color continued to be red up to 50.5 mM of NaCl and then turned back to the green color initially observed as the peak monitored enters the green region of the electromagnetic spectrum.

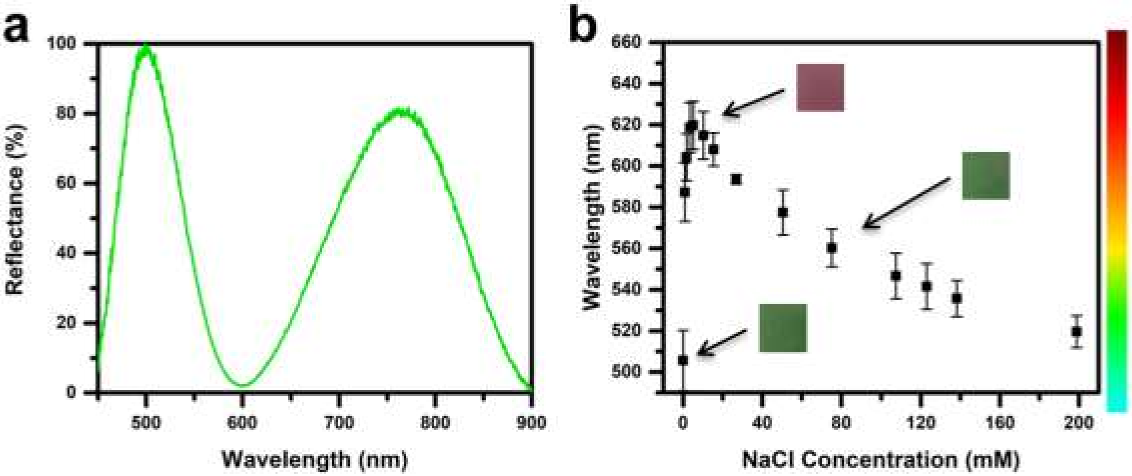

Figure 4.3 (a) Characteristic reflectance spectrum for pNIPAm-*co*-10%AAc microgel-based etalon devices in pH 9 solution and (b) their response to increasing concentrations of NaCl. The data point represents the average of 5 measurements and the error bars are their standard deviations. The insets are the corresponding color of the etalons at specific NaCl concentration. Initially, the sensors are green and showed red color at concentrations of 0.9 – 50.5 mM, after which they return to their initial green color.

The initial swelling behaviour of the microgels at low NaCl concentration (< 3.4 mM), characterized by a red shift in the reflectance spectrum, can be explained by the Donnan equilibrium theory. The exchange of mobile ions and solvent water molecules between the swollen anionic microgels in the etalon and its surrounding is represented in **Scheme 4.2**. The etalons are initially equilibrated with a solution of pH 9 (adjusted with NaOH) and as demonstrated in **Scheme 4.2**, the microgels in equilibrium with its surroundings bear a strong resemblance with Gibbs-Donnan equilibrium that is used to describe the equilibrium existent between two solutions that are separated by a semi-permeable membrane. In fact, the swollen anionic microgel is a solution and acts as its own membrane preventing the fixed negative charges randomly distributed through the microgels from diffusing into the external solution, creating a swelling force commonly referred as the swelling pressure. In this low salt concentration regime, the concentration of mobile ions is greater in the microgels than in the external solution due to the attracting power of the fixed negative charges and to satisfy the condition of electroneutrality. Consequently, the osmotic pressure of the solution inside of the microgels will be greater than that of the external solution. Due to this osmotic pressure difference, water molecules are driven into the microgels from a less concentrated external solution, causing them to swell. In addition, increasing the concentration of cations inside the microgels decreases the Debye screening length of the negatively charges groups and although they can approximate each other closer, the osmotic pressure inside on the microgels maintain them in a swollen state. Further increasing the concentration of NaCl up to 3.4 mM will decrease this concentration difference, yet existent and causing the microgels to continue swell but now decreasing its swelling capacity. At a concentration of 3.4 – 5 mM, it seems that equilibrium was reached, where the osmotic pressure inside and outside of the microgels are similar, thus the microgels neither swells nor shrink. We believe that this concentration is highly dependent on the % (mole) of AAc in the microgels and will be a focus of future investigations. At NaCl concentrations > 5 mM, the concentration difference between the mobile ions inside and outside the microgels increases again but now the osmotic pressure outside of the microgels will exceed that of inside, driving water molecules into the external solution and causing them to shrink. In addition, with a reduced osmotic pressure inside of the microgels and increased in Na$^+$ concentration, the electrostatic repulsion between the localized negative charges is tremendously reduced and the charges can get closer to each other, contributing even more to their shrinking behaviour. At high salt concentrations (> 100 mM), Hofmeister effects (salting-in/out) start impacting the microgels swelling behaviour, which we will be discussed in the next Chapter.

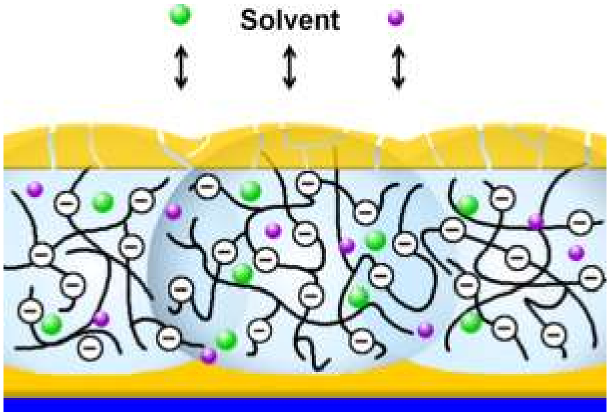

Scheme 4.2 Illustration of the etalon device showing the swollen anionic microgels in equilibrium with the NaCl solution. Fixed charges are resented by ⊖, sodium ions (Na$^+$) by 🟢, and chloride ions (Cl$^-$) by 🟣.

The reusability of the etalons was further demonstrated by determining their intra-day and inter-day precisions. The intra-day precision was determined by exposing a etalon device to solutions of ~1.5 mM NaCl 10 times over 2 days. Here, a closed flowing cycle was built to mimic the real system where the etalons would be placed and it is depicted in **Scheme 4.1**. The etalon was placed in such way that a continuous water stream flowed over the device and a fixed volume of NaCl solution was added to the centrifuge tube and stirred. We noted that the etalon's response was very quick, taking ~ 10 s to completely reach a red color after exposure to the NaCl and ~10 minutes for the reflectance spectrum to be stable (peaks no longer shifting). After stabilization, the solution inside the centrifuge tube was replaced with the blank solution 3 times to assure that the NaCl was completely removed from the system. Following, once the peak had moved back to its initial position, the etalon was exposed again to the NaCl solution. It is important to point out that the time scale for the peak to return to its initial position was significantly higher than the response time, taking approximately 40 min. This phenomenon is referred to as hysteresis and has been already documented in our previous publication when studying the etalons response to pH.[74] In our case, when the external solution is exchanged with the blank solution, the ions inside of the microgels will migrate from the microgels to the external solution, from their high concentration on the microgels to their lower concentration in the external solution. Nevertheless, due to the localized negative charges in the microgels, Na^+ and Cl^- ions will still be present inside of the microgels and their migration to the external solution will be significantly slow. The process of exposing the etalons to NaCl solution and resetting them with the blank solution was repeated 10 times between two days, 5 times for each day. Inter-day precision (day-to-day) was determined following the same procedure described above but exposing the etalon to NaCl solution once a day for 30 days. The results can be found in **Figure 4.4**. The averages and standard deviations for the initial peak and the response were 561 ± 8 and 620 ± 3 nm for intra-day and 523 ± 8 and 615 ± 8 nm for inter-day tests respectively. As demonstrated, the standard deviation of the measurements did not increase after 10 and 30 cycles compared with the standard deviations for the individual tests, which were 505 ± 14 nm for initial peak and 604 ± 11 nm in response to 1.7 mM. In fact, the variance among the etalons was slightly higher than the variance of their individual responses. The ability of the etalons to return to their initial color after been exposed to solution ionic strength changes for many cycles is very important from an economic point of view as the devices do not need to be replaced every time they detect a failure of the desalination system. Furthermore, its reusability is also of upmost importance from an environmental point of view as less waste is generated from the disposal of the sensors. However, the time required for the sensors to be reset is still not ideal. To decrease the reset time, we exposed the devices to a pH 3 solution for 10 minutes. We believe that exposing the etalons to pH 3 solution (DI water adjusted with HCl) causes the protonation of the carboxylic groups, neutralizing the negative charges of the microgels and breaking the ionic interactions. This would facilitate the diffusion of Na^+ and Cl^- ions from the microgels to the external solution. Here, we used round-shape etalons with a diameter of 5 mm that were prepared using a metal mask. After exposing them to a very high NaCl concentration (35 g/L, similar to sea water concentration), the etalons were rinsed with DI water for 30 sec, then exposed to a pH 3 solution (DI water adjusted with HCl) for 10 minutes while stirring, rinsed again with DI water and re-exposed to the blank solution, taking 10 - 15 min for its color to be uniformly green. The color of the etalon devices in each solution used is shown in **Figure 4.5**. Following this procedure, the etalon devices could be completely reset in 20 - 25 minutes.

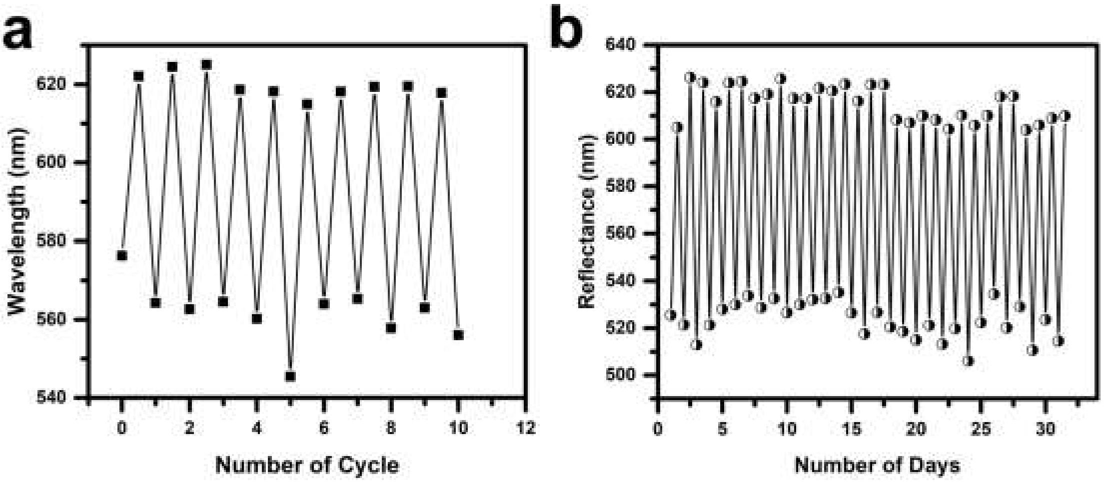

Figure 4.4 The repeatability of pNIPAm-*co*-10%AAc microgel-based etalons to varying ionic strength for (a) intra-day and (b) inter-day tests.

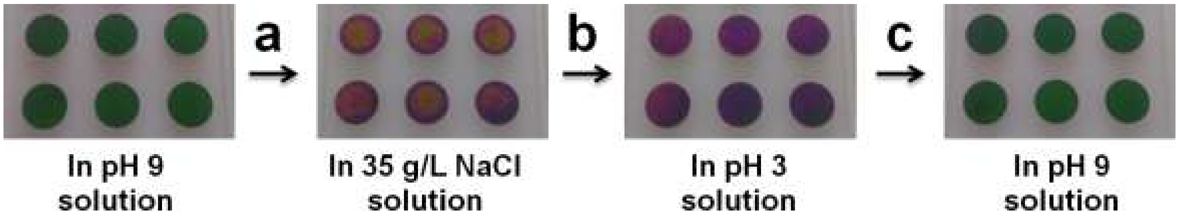

Figure 4.5 Etalons composed of pNIPAm-*co*-10%AAc microgels under different solutions used for their resetting after salt exposure. The etalons are initially green at pH 9 solution and once they are exposed to (a) NaCl solution, their color change to a mixture of violet and orange. After rinsing with DI water and (b) incubating them in pH 3 solution, their color turned to violet and finally returned to its initial green color after (c) incubating in pH 9 solution.

Finally, as the temperature of the water being produced from the desalination technology can be as high as 80 ^oC, we investigated the working temperature range where the etalons show a green color. The etalons were subjected to temperature changes from 2 to 35 ^oC inside of the temperature controlled chamber containing 13 mL of pH 9 solution. As shown in **Figure 4.6**, the microgels shrink as the temperature increases, leading to a blue shift in the reflectance spectra. Furthermore, the shift is more significant at temperatures > 25 ^oC. When fitting the data points from 2 to 25 ^{o}C and from 25 to 35 ^{o}C into a linear regression model, the slopes were -1.7 and -3.6 respectively. PNIPAm homopolymer microgels suspension show a sharp phase transition at ~32 ^{o}C, where the microgels undergo from a swollen to collapse state. Upon incorporation of AAc groups, the temperature swelling/deswelling behaviour of these microgels is highly dependent on the acrylic acid content, their charge density (solution pH), and solution ionic strength.[77, 107, 169] The LCST of these microgels is shifted to temperatures > 32 ^{o}C when the solution pH > pK_a due to the charge-charge repulsions between the negatively charged groups, the hydrophilic nature of the comonomer AAc, the lower NIPAm content, and the osmotic swelling.[76] However, when increasing the pH to 9, the ionic strength of the solution is increased due to the addition of Na^+ and OH^- ions, which decreases the Debye screening length and the repulsive electrostatic forces, causing the microgels to shrink at lower temperatures. This explains the broader and larger shift in the reflectance spectra at temperatures > 25 ^{o}C. Moreover, the etalons showed to be visually green at temperatures 17 – 35 ^{o}C and red color at T < 15 ^{o}C. Thus, the temperature of water being produced should be decreased to 17 – 35 ^{o}C before bring exposed to the sensors. This can be easily achieved by allowing the water that is coming out of the desalination system to flow through a length of tubing where it can exchange heat with the environment.

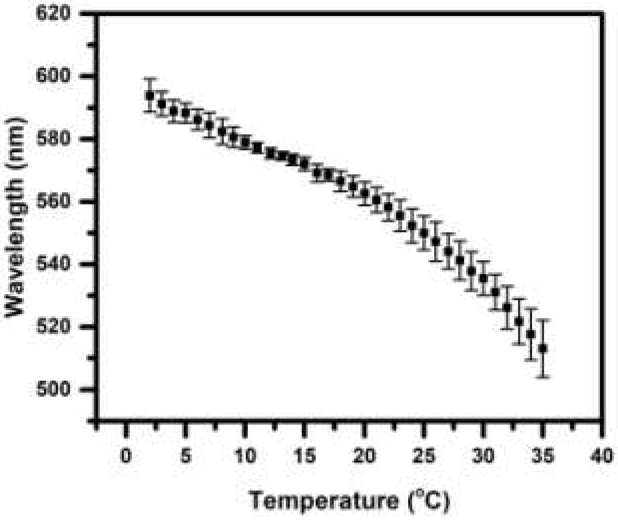

Figure 4.6 Temperature response for the etalons composed of pNIPAm-*co*-10%AAc microgels. Each data point represents the average of 3 measurements and the error bars are their respective standard deviation.

4.4 Conclusions

We have prepared etalon devices composed of pNIPAm-*co*-10%AAc microgels and investigated their performance to detect small changes in solution ionic strength. We found that these etalons are uniformly green when in equilibrium with pH 9 solution and their color quickly turned to red when exposed to 0.9 mM of NaCl. Their color continues to be red up to 50.5 mM of NaCl although shifts in the reflectance spectrum could be observed in this concentration range. It implies that the etalon devices can be used to detect early leakage in the desalination system as long as the ionic strength does not exceed 2,951 ppm, which is not expected at early stages of the system's failure. Furthermore, the etalons response to NaCl at different concentrations could be explained by the Gibbs-Donnan equilibrium theory. The devices showed to be highly reusable as demonstrated by their intra-day and inter-day precisions with a working temperature range of 17 °C to 35 °C. We also demonstrated that the etalon devices could be easily reset by exposing the devices to a pH 3 solution. The results presented in this chapter clearly demonstrate the potential of the etalons to be used in other systems where monitoring changes in chemical composition of known systems is desired.

Chapter 5

Probing the Dynamics of Hofmeister Series Ion Interactions with Poly (*N*-Isopropylacrylamide) Microgels-Based Etalons

5.1 Introduction

In 1888, Franz Hofmeister first reported on the effect various salts had on hen egg protein solubility in water.[170] From these studies, the Hofmeister series was established, which qualitatively ranks ions by their ability to precipitate/solubilize proteins or macromolecules in aqueous solution. The order of the ions relevant for this work in the Hofmeister series are shown in Figure 1**.** Ions to the left of chloride and sodium are referred as kosmotropes ("order-makers") and those to the right are referred to as chaotropes ("disorder-makers"). At first it was thought that kosmotropic and chaotropic ions affect the solubility of proteins or macromolecules by changing the water bulk structure.[171] However, more recent studies demonstrated that the interaction of ions with polymer chains have the highest impact on their physical behaviour rather than the change in the bulk water structure.[172-176] Substantial attention has been paid to Hofmeister phenomena due to their relevance in biological studies such as enzymatic activity,[177] protein stability,[178] channel-facilitated membrane transport,[179] bacterial growth,[180] and germination.[181] Not only limited to biological systems, the Hofmeister series plays an important role on the selectivity and response of ion sensing devices.[182-184]

Figure 5.1 Cations and anions of the Hofmeister series relevant to this work.

Stimuli responsive polymers that undergo chemical or physical changes in response to their environment have been widely used in a variety of applications such as drug delivery, artificial muscles, sensing and biosensing.[185-186] Due to its thermoresponsive properties, poly(N-isopropylacrylamide) (pNIPAm) has been a focus of many investigations since it was first reported by Heskins and Guillet in 1968.[39] Specifically, linear pNIPAm exists as a random coil (and is solvated) in water below the lower critical solution temperature (LCST) of 32 ^{o}C, while it exists as a globule (and is relatively desolvated) when T > LCST.[3, 187-188] Like linear pNIPAm, pNIPAm-based microgels are hydrophilic and fully water-soluble/swollen at T < LCST, while they are relatively hydrophobic and collapse (expelling their solvating water) at T > LCST; this transition is reversible over many cycles.[56, 58] Furthermore, pNIPAm-based microgels can be easily modified with other functional groups to render them responsive to a variety of external stimuli such as pH,[107, 189] ionic strength,[190] and light,[191]. One of the most common chemical modifications used is acrylic acid (AAc) that can render the microgels pH responsive.[189-190, 192] Specifically, when pNIPAm-*co*-AAc microgels are in a medium where the pH > pKa of AAc (~4.25), the carboxylic acid groups are mostly deprotonated (and negatively charged) and the microgels swell due to Coulombic repulsion between the negatively charged groups. In addition, increasing the internal charge repulsions as the pH is increased leads to an increase of the osmotic pressure exerted by the mobile ions screening the fixed charges, causing the microgel to further swell. However, when they are in a medium that has a pH < pKa, the carboxylic acid groups are protonated (neutralized) and the microgels adopt a smaller volume as a consequence of the reduced electrostatic repulsion. Moreover, it is not surprising that the swelling state of these microgels is affected by cations in solution as they can influence the Debye screening length of the charged groups. Increasing the solution ionic strength can lead to more screening of the charges, which reduces the charge-charge repulsions within the microgel and additionally cause them to decrease in diameter.

As pNIPAm contains both hydrophilic (amide) and hydrophobic (isopropyl) groups, it has been used as a model system to understand the ionic interactions in aqueous protein solutions that are responsible for the Hofmeister ranking of salts.[127, 193-194] It has been suggested that kosmotropic anions can polarize adjacent water molecules that are hydrogen bonded to the oxygen and nitrogen of pNIPAm's amide groups, thereby destabilizing their interaction and affecting pNIPAm's LCST.[127, 173] Thus, high charge density anions that form hydrate complexes (highly hydrated), which are located on the left side of Hofmeister series, have a greater impact on pNIPAm's LCST than less hydrated anions as they are able to easily polarize and disrupt interactions between water molecules and the amide groups. In addition, highly hydrated anions decrease the number of water molecules that are available to form hydrogen bond with the polymer, decreasing its hydration. Furthermore, the addition of ions to the solution increases the surface tension of the water/polymer hydrophobic interfaces, which increases the free energy cost to form cavities to accommodate the hydrophobic isopropyl groups and the polymer backbone.[127, 172-173] These effects, well known as the salting-out effect, decreases protein/macromolecule solubility and increases their stability via the formation of aggregates followed by a phase separation. On the contrary, the salting-in effect, which is better described as the direct interaction of weakly hydrated ions of low charge density with the polymer, can increase macromolecule solubility and decrease its stability.[195-197] In molecular dynamics studies of pNIPAm by Qian and coworkers, they showed that the cations interact more strongly with the carbonyl oxygen of the amide groups than the anions and that the strength of this interaction highly depends on the cation-anion contact pair association constant.[193] The weaker the ion-pairing interaction is, the stronger the cation interacts with the carbonyl oxygen, which makes the salting-out effect less pronounced. Their results indicated that anions do not interact directly with the carbonyl oxygen and its weak interaction is mediated via a positively charged cation. Rather, anions have a relatively strong interaction with the isopropyl group of pNIPAm with the least hydrated anions having the stronger binding. However, recent studies reported by Cremer and coworkers revealed that weakly hydrated anions, such as SCN^-, interact with the amide nitrogen and the adjacent α-carbon of a pentameric peptide (VPGVG) and these interactions, along with ion pairing, dictates the Hofmeister series.[197] The polarizability and hydration properties of specific ions seems to play an important role in the Hofmeister series and recently, Bruce *et al.*[198] reported that the degree of hydration of a weakly hydrated anion (chaotropic) could be modulated by another strongly hydrated anion (kosmotropic). Their studies revealed that in a mixture of salts, the combined effect of a weakly and strongly hydrated anion, such as in NaI and Na_2SO_4 respectively, is nonadditive and the ion hydration and ion-polymer interaction could be modulated by the presence and concentration of another kosmotropic/chaotropic anion. While significant progress has been made in understanding the Hofmeister effects on polymers, its microscopic origin is still not yet completely understood.

We have reported on the fabrication and use of Fabry-Pérot etalon or simply "etalon" for many applications, which are constructed by sandwiching pNIPAm-based microgels between two thin Au layers as illustrated in **Figure 5.2(a)**.[185, 199-200] The devices exhibit unique optical properties (i.e., multipeak reflectance spectra and color) that are a result of constructive and destructive interference of light entering the etalon and resonating in the microgel cavity. The optical properties can be predicted by Equation 5.1

$$\lambda = 2nd\cos\theta\,/m \tag{5.1}$$

where λ is the maximum wavelength being reflected, n is the refractive index of the dielectric (microgel) layer, d is the distance between the two Au mirrors, θ is the angle of incidence light, and m is the order of the reflected peak (e.g., 1, 2, 3,...). Since the microgels are temperature responsive materials, the optical properties can be tuned as a function of water temperature. We point out that at constant θ, the optical properties of the microgel-based etalons are dominated by the distance between the two Au layers as the change of the refractive index of the microgel layer as a function of solvation state is small compared to the thickness change. Important for this submission, exposing the etalons to salting-out inducing ions, the microgels' solubility decreases and they collapse, decreasing the distance between the two Au layers and resulting in a blue-shift in the peaks observed in reflectance spectra as shown in **Figure 5.2(b)**.

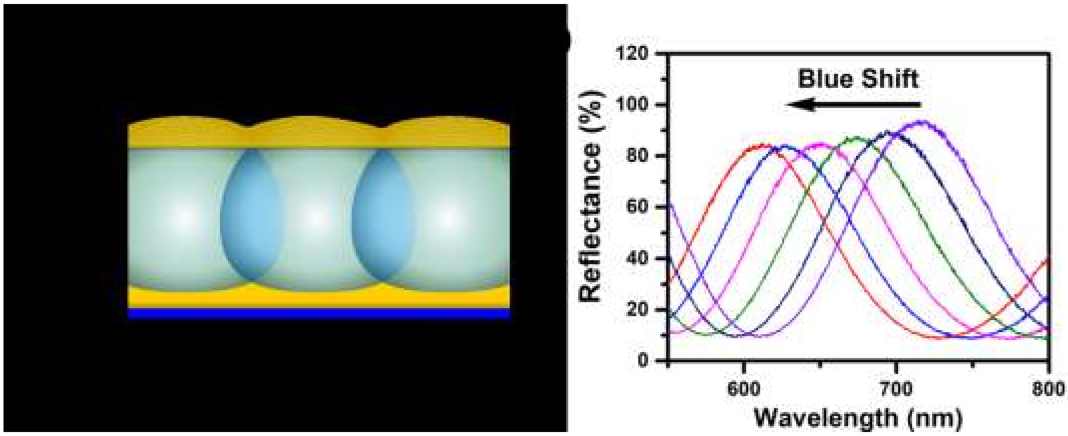

Figure 5.2 (a) The basic structure of pNIPAm microgel-based etalon composed of a microgel layer (II) sandwiched between two Au layers (I and III) on a support glass substrate (IV) (b) Representative reflectance spectra showing a blue shift upon exposure to a salt solution or increase in the temperature.

In this Chapter we explored the microgels' responsivity to aqueous solutions composed of specific salts in the Hofmeister series, i.e., NaCl, CH_3COONa, KCl, $MgCl_2$, $CaCl_2$, $MgSO_4$, $NaSO_4$, $(NH_4)_2SO_4$ by exploiting the etalon structure. Etalons composed of pNIPAm-based microgels with and without AAc were fabricated and their optical properties studied using reflectance spectroscopy. The position of the reflectance peak, and how the position changed with addition of the ions above, was used as an indicator of how the microgels themselves responded to the specific ions. This is the first attempt to study how specific ions in the Hofmeister series affect the hydration state of microgels in a confined space. The results revealed that the etalons responded to the salts in a manner that could be predicted from the Hofmeister series. In addition, a detailed analysis of the response process was performed in real-time, which allowed us to track details of the response that could not be seen in steady state measurements. Serpe and coworkers have demonstrated that it is possible to monitor the deswelling of the microgels in real-time but detail analysis of the kinetic response and how it can be correlated with the species in solution was never attempted.[118] By monitoring the peak shift over time in response to salt ions, it was revealed that the etalons respond to a combination of osmotic and salting effects. Furthermore, etalons prepared with non-ionic microgels (containing no AAc) showed higher sensitivity at higher salt concentrations due to the lack of charge repulsion inherently present in anionic microgels that prevents further deswelling of the microgels.

The results presented here are of great interest for our future ion sensing systems, and can lead to a more comprehensive understanding of the Hofmeister series, and how ions interact with both natural and synthetic polymers. Importantly, etalons uniquely allow us to directly probe the effect that specific ions have on the microgel hydration state in real time and account for osmotic pressure and Hofmeister effects, which is extremely hard (or impossible) to probe using other commonly used techniques, e.g., dynamic light scattering.[201] The dynamics of the salt response process can be used for ion sensing applications due to their unique response patterns, such as the response shapes, e.g., the time that the etalon response reaches its maximum, the magnitude of the response, and the time required to reach equilibrium. Finally, this system allows us to investigate fundamental properties of ion exchange, i.e., etalons allow us to probe ion exchange kinetics, and study how kosmotropic and chaotropic ions can affect each other during the exchange process. All of this together allows us to access ion exchange dynamic data that is not possible using any other approach.

5.2 Experimental Section

5.2.1 Materials

N-isopropylacrylamide (NIPAm) was obtained from TCI (Portland, Oregon) and purified by recrystallization from hexane (ACS reagent grade, EMD, Gibbstown, NJ) prior to use. N,N'-methylenebisacrylamide (BIS) (~99%), acrylic acid (AAc) (~99%), ammonium persulfate (APS) (~98%), sodium hydroxide (NaOH), ammonium sulfate ($(NH_4)_2SO_4$), magnesium chloride ($MgCl_2$), and sodium chloride (NaCl) were purchased from Sigma-Aldrich (Oakville, Ontario) and were used as received. Glass substrates (25 mm x 25 mm) and calcium chloride ($CaCl_2$) were obtained from Fisher (Ottawa, Ontario). Potassium chloride (KCl) was purchased from EMD (Mississauga, Ontario). Sodium nitrate ($NaNO_3$), sodium sulphate (Na_2SO_4), magnesium sulphate, hydrochloric acid (HCl) and sodium acetate ($NaCH_3COO$) were obtained from Caledon Lab. (Georgetown, Ontario). Deionized (DI) water, with resistivity of 18.2 MΩ·cm, was obtained from a Millipore Milli-Q-Plus system (Billerica, MA). Cr (99.999%) and Au (99.99%)

were obtained from ESPI Company and MRCS Canada (Edmonton), respectively. Whatman #1 paper filters were purchased from GE Healthcare (U.K.).

5.2.2 Synthesis of pNIPAm-Based Microgels

PNIPAm-based microgels containing 10% AAc (pNIPAm-*co*-10%AAc) were prepared by free radical precipitation polymerization of the monomer NIPAm with BIS as the crosslinker and AAc as a comonomer following a previously published procedure.[202] In short, NIPAm (11.9 mmol) and BIS crosslinker (0.703 mmol) were dissolved in 99 mL of deionized water in a beaker. The resulting mixture was filtered using a 20 mL syringe affixed with a 0.2 μL filter and transferred into a 3-neck round bottom flask which was fitted with a reflux condenser, nitrogen gas inlet, thermometer, and stir bar. The solution was allowed to heat to 70 °C over ~1 h, after which AAc (1.43 mmol) was directly added using a micropipette. The reaction was then initiated by transferring a solution of ammonium persulfate (APS) (0.2 mmol in 1 mL of DI) into the reaction mixture. The reaction was allowed to proceed for 4 h at 70 °C, under N_2 atmosphere. The resulting microgel solution was allowed to cool overnight at room temperature, and then filtered using a Whatman #1 paper filter to remove large aggregates that might have formed during the polymerization reaction. Finally, the microgels were purified via centrifugation and resuspension in water 6 times and the concentrated microgel solution was collected. The same procedure described above was used to synthesize microgels composed of NIPAm (13.33 mmol) and BIS (0.703 mmol) without the addition of AAc.

5.2.3 Microgel Characterization

Dynamic light scattering (DLS) was used to measure the microgel hydrodynamic diameter in DI water using a commercial Zetasizer Nano ZS – Malvern Instrument (Westborough, MA, USA) equipped with a 633 nm light source at 25 ^{o}C. Differential interference contrast (DIC) microscopy images of the microgels in the dried state were obtained using an inverted microscope (Olympus IX71) equipped with a iXon electron multiplying CCD camera (Andor Technology) at 100x magnification and is displayed in **Figure 5.3**.

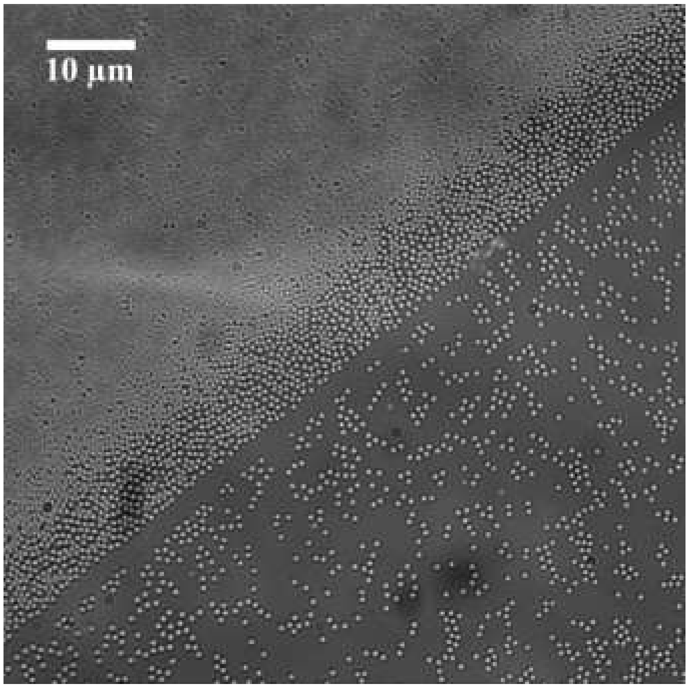

Figure 5.3 Microscopic image of microgels based on pNIPAm-*co*-10%AAc in the dried state with average diameter size of 0.67 ± 0.04 µm. A drop of concentrated solution was placed on a glass substrate coated with 15 nm Au and allowed to dry at 35 ^{o}C. Following, the excess of microgels was rinsed off and the substrate was incubated in DI water overnight. The substrate was then rinsed with DI water, dried over N_2 and used for image. The highly dense part in the image corresponds to where the drop of concentrated microgel solution was added.

5.2.4 Etalon Fabrication and Surface Characterization

Etalons were prepared following a previous reported "paint-on" protocol.[203] Briefly, a concentrated solution of microgels was used to create a homogenous, monolithic coating on a 15 nm Au-coated glass substrate (1 inch^2) after which another 15 nm Au layer was deposited using a thermal evaporation system (Torr International Inc., New Windsor, NY). It is important to note that 2 nm Cr was always deposited before the Au layer to facilitate the strong adhesion of the Au to the glass. 1 cm^2 etalons were obtained using a metal mask that yielded 4 etalons/glass substrate as shown in **Figure 5.4(a)**. After the etalons were fabricated, they were immersed in a freshly prepared aqueous solution with a pH 7 (adjusted with NaOH), and 100 mM IS (adjusted with addition of NaCl) for at least 3 h before being used for the salt response experiments. We refer to this solution as our "standard solution". For experiments at the various solution pHs, etalons were immersed in a solution containing the desired pH with the IS constant (100 mM). Scanning electron microscopic (SEM) images of the etalon's surface were collected using a LEO 1430 SEM (Carl Zeiss SMT AG, formerly LEO Electron Microscopy Ltd., Oberkochen, Germany) and is shown in **Figure 5.4(b,c)**.

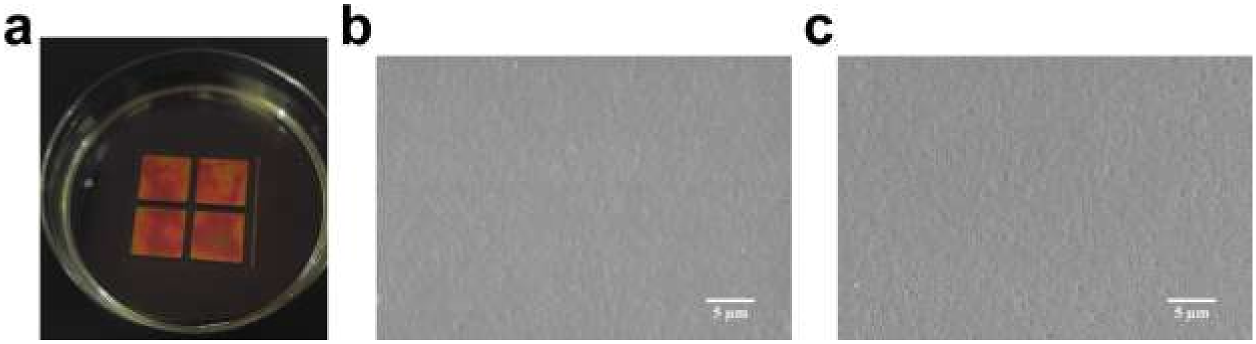

Figure 5.4 (a) Photograph of 4 etalons with size of 1 cm^2 obtained using a shadow mask in DI water. The glass substrate was cut into 4 pieces using a tungsten scribing pen to obtain 4 individual etalons. Representative SEM images of the etalons surface composed of pNIPAm-co-10%AAc microgels (b) before and (c) after the salt exposure experiments. The etalons was 30^o angled relative to the source.

5.2.5 Salt Response Measurements and Reflectance Characterization

The standard solution (pH 7, 100 mM IS adjusted with NaCl) was used to prepare 1 M solution of each salt (NaCl, CH_3COONa, KCl, $MgCl_2$, $CaCl_2$, $MgSO_4$, $NaSO_4$, $(NH_4)_2SO_4$, $NaNO_3$) and also to stabilize the etalons before the salt response experiments. Etalons soaked in the pH 7 standard solution for at least 3h were quickly transferred to a small Petri dish and fixed in place with adhesive tape. The Petri dish was then placed on a hot plate set at 25 ^oC, after which 600 μL of the standard solution was transferred to the center of the device. The R400-7 VIS-NIR optical reflectance probe, which was purchased from Ocean Optics (Dunedin, FL), was inserted into this solution such that the light was striking the normal of the etalon. Spectra were recorded using Ocean Optics Spectra Suite Spectroscopy Software over a wavelength range of 450-950 nm and spectra were only collected once the signal was stable, for example, the peak position was no longer changing after 15 minutes. To the 600 μL of standard solution on the etalon, varying amounts (38.4, 47.7, 114.2, 160 and 240 μL) of a given 1 M salt solution was successively added using a micropipette. Before each successive addition, we ensured that the reflectance spectrum was stable. For the kinetics measurements, the experimental conditions were the same as described above, but the reflectance spectrum was collected every 3 seconds rather than after stabilization.

For all experiments, the resultant reflectance spectra were analyzed by assessing the change of the position of the reflectance peak centered at ~770 nm. A Gaussian was fit to the reflectance spectra to obtain an objective measure of the peak position. In all cases, the experiments were repeated at least three times.

5.3 Results and Discussion

DLS was used to measure the diameter of the pNIPAm-*co*-10%AAc microgels in DI water, which showed a hydrodynamic diameter of 1.1 ± 0.1 μm. Etalons were constructed from microgels and their surface characterized by SEM before and after exposure to the salt solutions. As can be seen in the images in **Figure 5.4(b, c)**, exposure of the etalons to the salt solutions doesn't appear to impact the etalon structure. The etalon response to a variety of salt solutions such as NaCl, CH_3COONa, KCl, $MgCl_2$, $CaCl_2$, $MgSO_4$, $NaSO_4$, $(NH_4)_2SO_4$ was assessed by monitoring the position of the reflectance peak. As shown in **Figure 5.5**, the etalons were responsive to all the salts used, meaning that the salt ions can affect the physical conformation (i.e., hydration state) of the microgels sandwiched between the two Au layers, causing a peak shift in the reflectance spectrum. Furthermore, we observed that the response increased as the salt concentration increased. Specifically, **Figure 5.5(a)** shows the etalon response to monovalent and divalent chlorides. As can be seen, Ca^{2+} and Mg^{2+} yielded enhanced responses compared to Na^+ and K^+. In addition, K^+ showed a more substantial response than Na^+, especially at higher concentrations, but the etalon's response to Ca^{2+} and Mg^{2+} appeared similar over a broad range of concentrations. Following the Hofmeister series, we were expecting larger responses for K^+ and Na^+ are expected to yield a larger response compared to Mg^{2+} and Ca^{2+} as they contribute to salting-out effect. However, the opposite was observed here. This can be attributed to the composition of the microgels used to prepare the etalons, which contain carboxylic acid groups that are deprotonated at pH 7. Mg^{2+} and Ca^{2+} are both divalent ions and can decrease more significantly the Debye screening length of the negatively charged carboxylic groups than K^+ and Na^+, considerably reducing the electrostatic repulsion and leading to larger responses. Therefore, in these systems, the strength of the salting-out effect needs to be considered along with the magnitude of the charge of the cations. This is consistent with earlier observations reported by Basser and coworkers[164] when studying the swelling behavior of sodium polyacrylate gels in aqueous solutions of NaCl, KCl, and $CaCl_2$. The authors found that as the concentration of salts was increased, the swelling degree of the gels gradually decreased, which was attributed to the reduction in the difference between the concentration of ions inside and outside of the gel as the concentration of ions outside of the gels increased. Furthermore, they observed that the effect of the ions on the swelling equilibrium of the gels followed the Hofmeister series for monovalent cations, such as Na^+ and K^+, and the concentration of divalent cations were shown to have a greater impact on the deswelling of the gels compared to the monovalent cations. Moreover, Mg^{2+} and Ca^{2+} are both chaotropic ions and do not contribute to the salting-out phenomena like Na^+ and K^+, which explains the larger response of K^+ (more pronounced salting-out effect) over Na^+ and similar response for Ca^{2+} and Mg^{2+}. Thus, for anionic pNIPAm-based microgels, the ability of cations to screen the negatively charged groups and reduce the charge-charge repulsions in the microgels needs to be taken into account along with the Hofmeister effects.

Figure 5.5(b, c) shows the etalons' response to different anions and cations, respectively. In **Figure 5.5(b)** (salts contain the same cation and different anions), we observed that the etalons responded to SO_4^{2-} > CH_3COO^- > Cl^-. As is evident from the Hofmeister series, the strongest salting-out anion SO_4^{2-}, and is expected to have the largest response while Cl^- should be the smallest. This is consistent with our observations and can be attributed to the fact that the anions will not contribute to charge screening within the microgels. Rather, their response will be manifested as a salting-out effect, which is currently used to explain the Hofmeister ranking of ions. Nonetheless, we attribute the significantly larger response for Na_2SO_4 to the fact that in addition to the strong salting-out effect contribution from sulphate ions, there are two Na^+ ions present which can highly decrease the Debye screening length and allow closer proximity of the negatively charged carboxylic groups. This is in agreement with our early observations (**Figure 5.5(a)**) where the cations had a greater impact on the deswelling state of anionic microgels. In **Figure 5.5(c)** (salts contain the different cations and the same anion), we observed that the etalons responded to NH_4^+ > Na^+ > Mg^{2+} with some minor deviations from the sequence at low salt concentration. SO_4^{2-} and NH_4^+ are kosmotropic and highly contribute to salting-out effect. Both of them are located on the extreme left side of Hofmeister series due to their greater ability to precipitate proteins.[204] Furthermore, in $(NH_4)_2SO_4$ there are three kosmotropic ions available for interaction. Not surprisingly, $(NH_4)_2SO_4$ was shown to yield the largest overall etalon response out of all the sulphates tested as predicted from Hofmeister series. It is noteworthy that the responses for sulfates the $MgSO_4$, $NaSO_4$, $(NH_4)_2SO_4$, which are known to form ion-pairing in solution, showed a linear behavior with increasing electrolyte concentration. However, the response for NaCl, KCl, CH_3COONa, $MgCl_2$, and $CaCl_2$ adopted a non-liner behavior. The effect of salts in solution has been demonstrated to be non-linear in some cases as shown by

Sadowski and coworkers when studying amino-acid solubilities in solution, osmotic coefficients of complex electrolyte systems, and activities of univalent cations and anions in aqueous solution.[205-207]

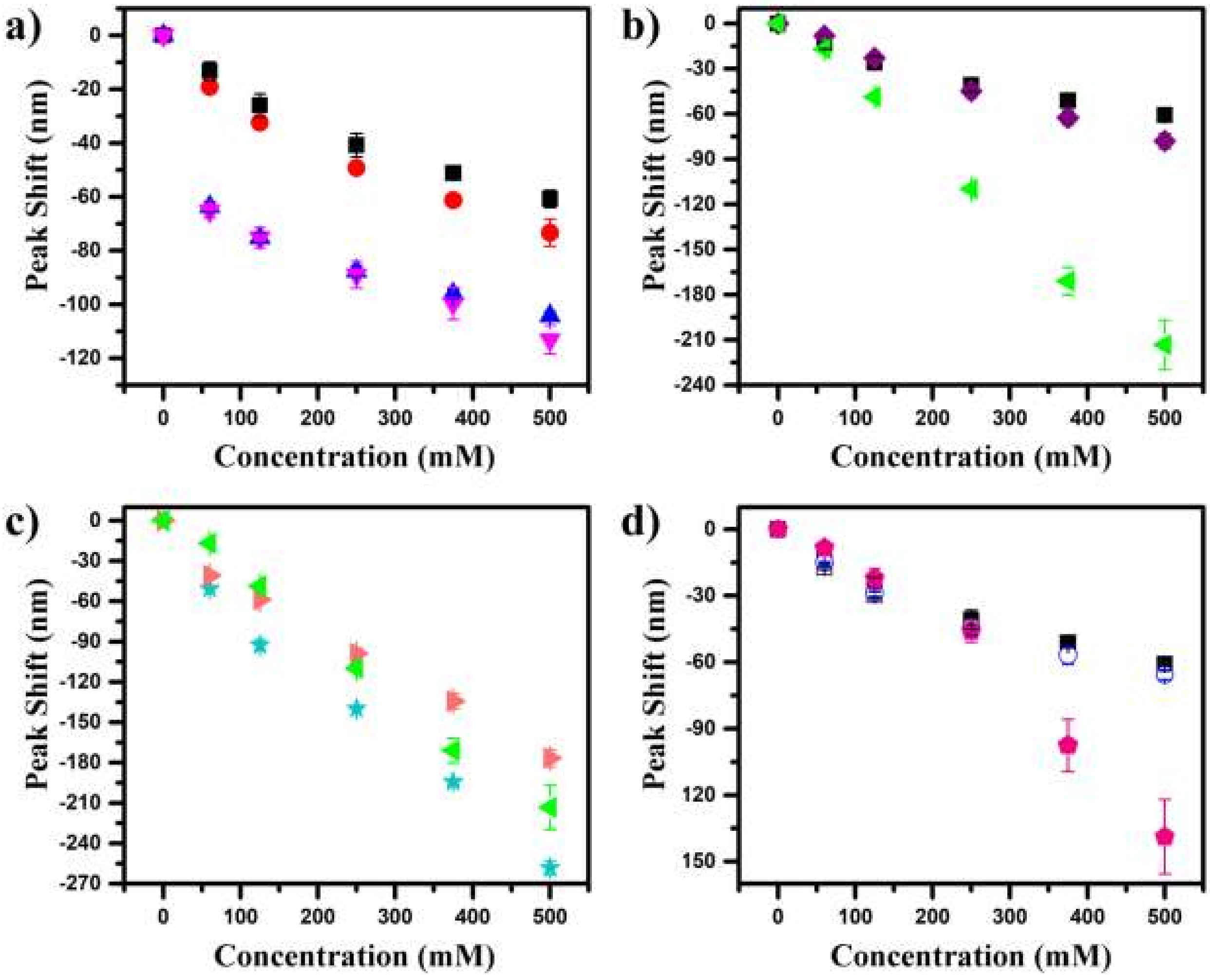

Figure 5.5 Cumulative wavelength shift of pNIPAm-co-10%AAc etalons in pH 7 standard solution for (a) monovalent ((■) NaCl, (●) KCl) and divalent ((▲) MgCl$_2$, (▼) CaCl$_2$) chloride salts; (b) sodium derivative salts ((■) NaCl, (◆) NaCH$_3$COO, and (◀) Na$_2$SO$_4$); (c) sulphates ((◀) Na$_2$SO$_4$, (▶) MgSO$_4$, and (★) (NH$_4$)$_2$SO$_4$) and (d) NaCl response at different pH values: (⬟) pH 3, (○) pH 5, (■) pH 7, and (□) pH 9. The ionic strength was kept constant (100 mM) for each solution. Each data point represents the average of three independent experiments and the error bars are the standard deviation for each measurement.

We further investigated the etalon's response to NaCl at different solution pH as some of the salts used for this investigation generated solutions with pH varying from 5.6 ($MgCl_2$) to 9.6 ($CaCl_2$). In this range of pH the degree of protonation of the carboxylic groups varies,[190] which may influence the etalon's response to the salt solutions. For this, pH 3.0, 5.0, 7.0, and 9.0 solutions were prepared and the ionic strength adjusted to 100 mM using NaCl and finally 1 M NaCl solutions were made at these pHs. The etalon response to NaCl at the different pHs is shown in **Figure 5.5(d)**. As can be seen, the response of the etalons to NaCl was statistically similar for solutions with pH ≥ 5. Therefore, we can conclude that the pH variation for $MgCl_2$ and $CaCl_2$ did not significantly affect the etalon response, and the observed responses are a result of the interactions between the specific ion and the polymer itself.

It is important to note that we observed a blue shift of the peaks in the reflectance spectra for all the salts used in this investigation, which is a result of microgel collapse, regardless of if the salt ion is classified as kosmotropic or chaotropic. We hypothesize that this final blue shift is due to the presence of cations screening the negatively charged carboxylic groups, causing the anionic microgels to shrink. However, the degree of deswelling depends on the charge of the ion and its position in the Hofmeister series (salting-in/out effect) as previously discussed. In addition, the total blue shift observed is also attributed to the etalons response as a result of osmosis. A schematic illustration for the proposed response mechanism is shown in **Scheme 5.1**. When the salt solution was initially injected, its concentration is higher in the external solution than inside of the etalon, which ultimately drives water molecules from the microgels to the external solution where the salt concentration is higher, causing the microgels to deswell as a result of osmosis. In parallel, as the ions diffuse across the solution due to the concentration gradient and start entering the microgels the negatively charged carboxylic groups are screened by the cations and a concurrent salting-in/out effect that also impacts the hydration state of the anionic microgels, according to their ranking in the Hofmeister series. An eventual equilibrium in microgel diameter (and microgel layer thickness) is reached that is a combined result of osmosis, Hofmeister effects, and the extent of charge screening in the microgels. As the salt concentration in the external solution increases with further addition of salt solution, more water molecules are driven by osmosis from the microgels to the external solution, causing them to further shrink and a further blue shift is observed in the reflectance spectra. For kosmotropic ions, which are known to cause the polymer to collapse, their response is additive to the collapse induced by the osmotic effect and the magnitude of charge screening as both cause the microgels to collapse while for chaotropic ions, which are known to cause the polymer to swell, their response is non-additive and is subtracted from the response caused by the osmotic effect and reduced in charge-charge repulsion. Therefore, if the degree of swelling caused by the salting-in effect is smaller than the degree of deswelling caused by the osmotic effect and reduced charge-charge repulsion, a final blue shift is observed. This implies that the degree of swelling for all chaotropic ions studied here did not overcome the degree of deswelling caused by the osmotic effect and reduced in charge-charge repulsion. However, the degree of swelling indeed depends on type of chaotropic ions as they showed different responses as can be seen in **Figure 5.5(c)** ($NH_4^+ > Na^+ > Mg^{2+}$). To visualize the etalon response to osmotic and salting-in/out effects, we monitored the etalon response over time upon exposure to 60 mM of $(NH_4)_2SO_4$, NaCl, and $MgCl_2$. These three salts were chosen because they are located in different positions along the Hofmeister series. By monitoring the peak shift kinetics, we are able to probe the real-time responses of pNIPAm to the addition of salt, which is a very unique aspect of utilizing the etalon structure to probe Hofmeister effects. As can be seen in **Figure 5.6**, we divided the response kinetics into 3 phases. In phase 1, a fast blue shift was observed in the first minute for all the salt ions, which we attribute to the microgel's osmotic response, as previous discussed. At this point, we assume that the microgels have no direct interaction with the ions, and only respond to the solution ionic strength via osmosis. This is similar to observations reported by Sivanantham *et al.* when characterizing the swelling kinetics of water-swollen polyacrylamide hydrogels when exposed to various concentration of NaCl.[208] The hydrogel underwent deswelling at short times as the ionic solution pulled the water molecules from the hydrogel due to the osmosis effect. In phase 2, ions start entering the microgel as osmosis proceeds, bringing water molecules back and resulting in a red shift. The transition from phase 1 to phase 2 is faster for $(NH_4)_2SO_4$ and $MgCl_2$ (around 0.5 and 0.2 s respectively) than for NaCl (around 1 min), which we attribute to their higher ionic strength difference that causes their diffusion rate to be higher. In phase 3, the Hofmeister effects start to impact the microgels response to the ions in solution, ultimately dominating the final response. Here, a continuous blue shift was observed for $MgCl_2$ and kosmotropic $(NH_4)_2SO_4$. The continuous blue shift observed for $MgCl_2$ is due to the charge of Mg^{2+} that needs to be considered when using etalons prepared with anionic microgels. For non-kosmotropic NaCl, a continuous red shift was observed and the transition from phase 2 to the Hofmeister effect could not be distinguished, leaving NaCl with only two phases.

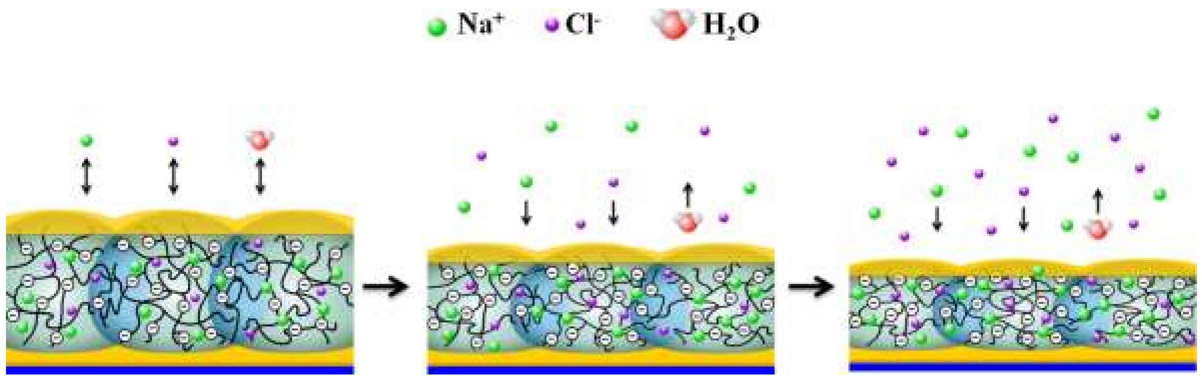

Scheme 5.1 Schematic illustration of pNIPAm-*co*-AAc microgels-based etalon response to salt ions. Initially, the etalons are in equilibrium with the standard solution (100 mM IS adjusted with NaCl). After addition of salt, in this case NaCl, the concentration of Na^+ and Cl^- ions in the external solution increases, increasing the difference in concentrations inside and outside of the microgels, driving water molecules out of the microgels into the external solution and causing them to shrink. Following, the ions diffuse to the anionic microgel layer where charges are being screened and salting-in/out effect take place. Further addition of salt increases the concentration of the ions in the external solution, causing the microgels to further shrink and further decrease in the Debye screening length, which is observed as a further blue shift.

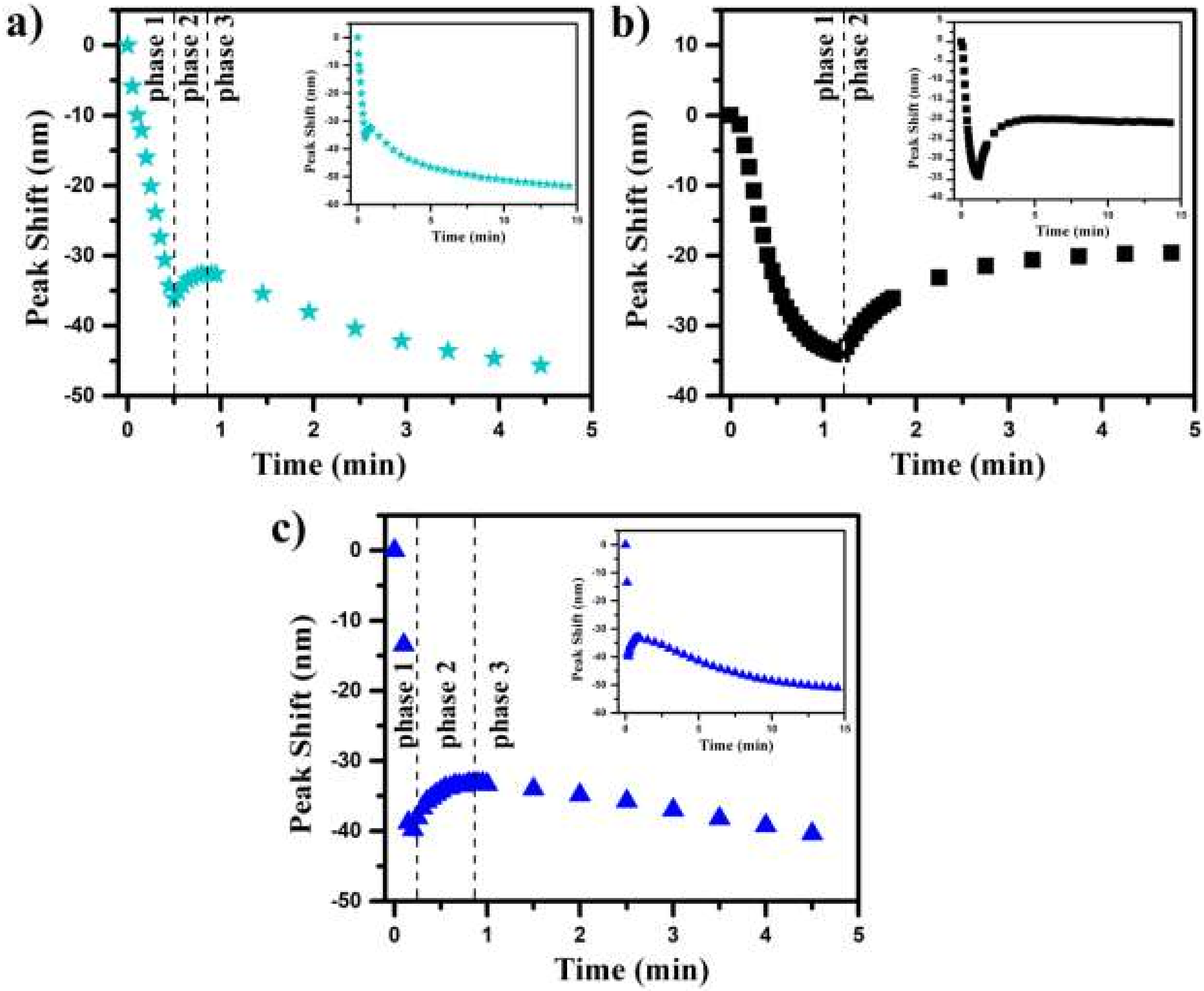

Figure 5.6 Kinetics of the etalon response to 60 mM of (a) $(NH_4)_2SO_4$, (b) NaCl, and (c) $MgCl_2$. Etalons were constructed using p(NIPAm)-co-10%AAc microgels. The salt solution was quickly added to the solution that the etalon was immersed and then mixed to ensure homogeneity. The insets show the corresponding response kinetics up to 15 minutes. The dashed lines indicate the 3 defined stages of response kinetics as explained in the text.

Furthermore, we investigated how etalons prepared with non-ionic microgels responded to the salts. For these experiments, pNIPAm microgels were used that did not contain AAc, but keeping the total number of moles of monomer and crosslinker constant (14.0 mmol). The hydrodynamic diameter of the microgels measured by DLS was 0.78 ± 0.17 μm in DI water, smaller than the microgels containing AAc due to the lack of charge repulsion. The response of the resultant etalons to NaCl and $(NH_4)_2SO_4$ was assessed, as shown in **Figure 5.7(a, b)**. As can be seen, the etalons also exhibit a concentration dependent response, and the response of etalons composed of non-ionic pNIPAm microgels to NaCl and $(NH_4)_2SO_4$ was greatly enhanced compared to etalons composed of anionic microgels. This can be explained by considering that the swelling forces are remarkably increased as a result of the localization of negative charges present in pNIPAm-*co*-AAc microgels compared to non-ionic pNIPAm-based microgels.[209] **Scheme 5.2** schematically depicts the effect of localized charges on the deswelling power of the microgels. When the carboxyl groups are deprotonated, such as in pH > 5, the negatively charged carboxyl groups on the polymer chains leads to electrostatic repulsion that expands the network. When exposed to salt solutions, the microgels collapse by a mechanism previously discussed, although the remaining localized charges still cause the microgels to be swollen. On the other hand, microgels prepared with no AAc show a higher volume change when they are exposed to salts because of the lack of charge repulsion in the microgel network, effectively making the salt ions more effective at causing the microgel to collapse. We could also observe this phenomenon when analyzing the effect of pH on the salt response (**Figure 5.5(d)**). The response to NaCl was significant enhanced when the pH of the solution was 3 (below the pKa of AAc). Finally, we investigated how the etalons composed of non-ionic pNIPAm-based microgels respond to NaCl, $CaCl_2$, and $NaNO_3$. Here, we explored how cations and anions of the Hofmeister series influence the etalon's response. The results found in **Figure 5.7(c)** shows that the response for these salt ions follow the Hofmeister series, i.e., NaCl gave larger responses compared to $NaNO_3$. The same order in the sequence was reported by Lopez-Leon *et al.*[210] when characterizing the effect of electrolyte type and concentration on the hydrodynamic diameter of cationic and anionic pNIPAm microgels. The authors found that the minimum salt concentration needed to induce the collapse of the microgels follows the sequence: $Cl^- < NO_3^- < SCN^-$. Thus, Cl^- ions would yield larger responses from the etalons as the microgels start to collapse at lower concentrations. In the case of cations, Na^+ gave larger responses compared to Ca^{2+}, although these differences are not as significant as those observed for the anions. The difference in the maximum peak shift for Na^+ and Ca^{2+} was around 11 nm while Cl^- and NO_3^- was 36 nm. This larger difference in response for the anions compared with the cations is primarily due to the fact that anions are polarizable and their hydration is stronger than that for cations.[211-213] The stronger hydration of anions is attributed to the possibility of intrashell hydrogen bond formation of the anion with the hydrogen atom of water molecules and charge transfer between the anion and the water molecules as it is easier for the oxygen atom of the water molecule, which is very electronegative, to accept negative charge from anions than positive charge from cations.[171, 212, 214] Therefore, anions can contribute to a stronger salting effect than cations and thus their responses are more pronounced. We also noticed that for chaotropes ions, such as Ca^{2+}, the total peak shift for etalons made with anionic microgels is significant larger compared to the peak shift for etalons based on non-ionic microgels. Based on that, anions were shown to have a significant influence in the etalon's response compare to cations when using non-ionic microgels while cations influence strongly in the etalons response when using anionic microgels.

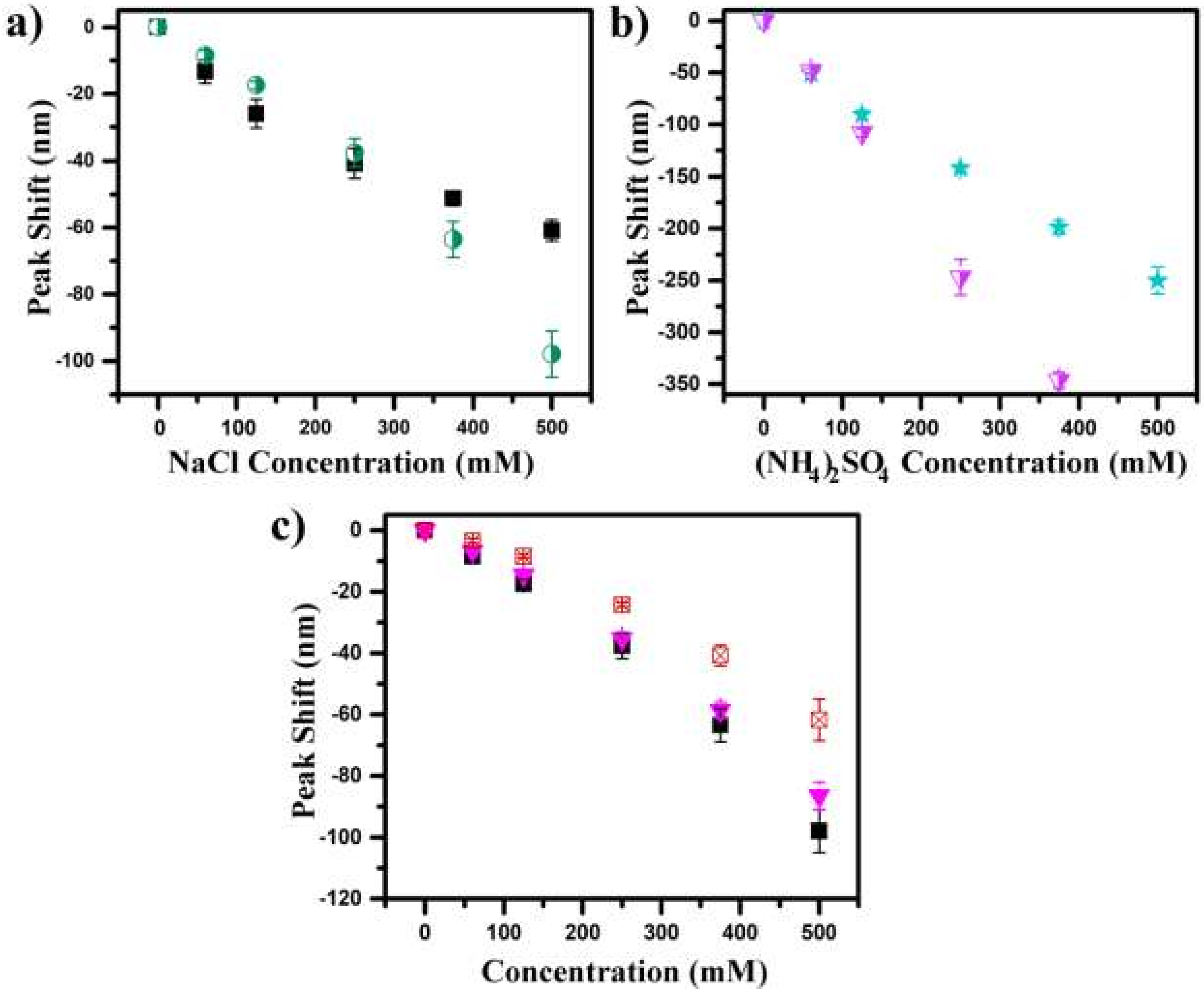

Figure 5.7 (a) Etalon response to NaCl prepared using (■) anionic and (◑) non-ionic pNIPAm microgels. (b) Etalon response to $(NH_4)_2SO_4$ prepared using (★) anionic and (▽) non-ionic pNIPAm microgels. (c) Etalon response to (■) NaCl, (▼) $CaCl_2$ and (⊠) $NaNO_3$ prepared using pNIPAm microgels (no AAc). Each data point represents the average of three measurements and the error bars are the standard deviation for each value.

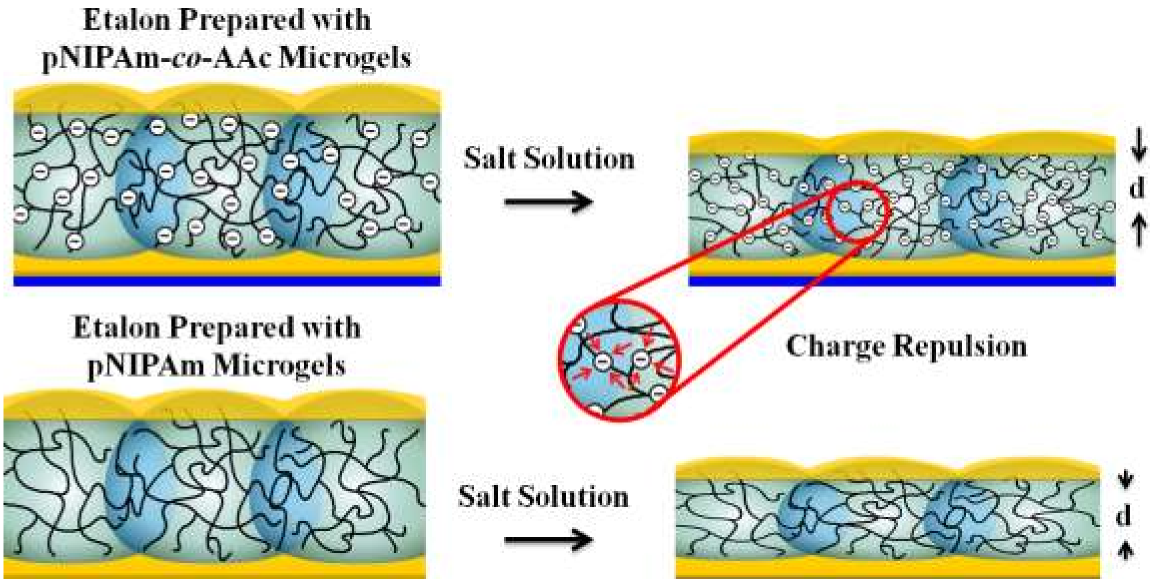

Scheme 5.2 Schematic illustration of the effect of ionic (top) and non-ionic (bottom) microgels on the response magnitude of the etalons. For etalons prepared with pNIPAm-*co*-AAc microgels, as the microgels shrink, the relative distance from one charged carboxyl group to another decreases, increasing the electrostatic repulsion. Even though the charges have been screened by counterions in solution, represented by the red arrows and smaller charge in the scheme, further deswelling is not favorable. On the contrary, non-ionic microgels undergo a larger volume change due to the lack of fixed charges along the polymer chain that would prevent it from further deswelling.

We further investigated the etalons' response to a mixture of salts and if we could predict the total shift based on theoretical calculations. Here, the etalons were exposed to increasing concentrations of a mixture of 1:1 NaCl and $(NH_4)_2SO_4$ and the accumulative peak shift is shown in **Figure 5.8**. The theoretical values were calculated from their individual peak shift and considering that they were addictive of equal intensity. As we can see from **Figure 5.8**, the theoretical values are very similar to the measured peak shift. This suggests that the detection of specific ions in solution and their concentration might be possible using the etalon devices. However, more studies need to be done to determine if the contributions to the total peak shift for a mixture of kosmotropic and chaotropic ions are additive, non-additive, and how the intensity of their contributions varies with concentration and type of ions.

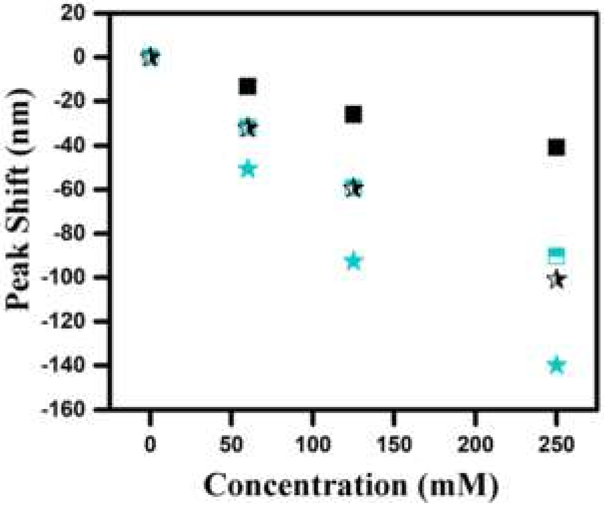

Figure 5.8 Comparison of peak shifts for a mixture of 1:1 (★) NaCl and $(NH_4)_2SO_4$ with (🟦) theoretical calculations based on the individual peak shifts for (■) NaCl and (★) $(NH_4)_2SO_4$. The theoretical calculations were done considering that their contributions to the total peak shift was additive with equal intensity.

Finally, we explored the reusability of the etalons after salt exposure and the results can be seen in **Figure 5.9**. For this experiment, the device was first exposed to the NaCl solution, washed three times with DI water and incubated for 30 min in DI water before again being exposed to a solution of NaCl with the same concentration. Finally, the etalon was rinsed and again exposed to the NaCl solution. As can be seen in Figure 8, the position of the reflectance peaks were very similar (as can be seen from the small standard deviations in the peak position) after multiple exposure and rinsing cycles. Thus, the optical devices were used at least three times before being discarded.

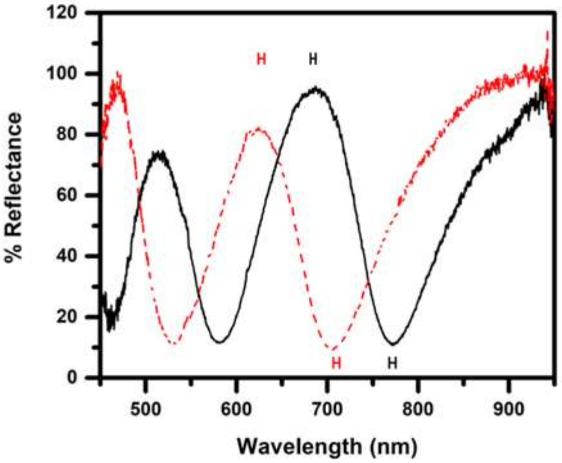

Figure 5.9 Reflectance spectrum for etalons (solid line) before and (dashed line) after exposure to 500 mM of NaCl. The x-axis error bars located above and below the peaks correspond to their standard deviation.

5.4 Conclusions

In this study, we investigated the dynamics of pNIPAm-based microgel interactions with various Hofmeister series salts (e.g., NaCl, CH_3COONa, KCl, $MgCl_2$, $CaCl_2$, $MgSO_4$, $NaSO_4$, $(NH_4)_2SO_4)$ by exploiting the optical properties of microgel-based etalons. Two sets of etalons were prepared with pNIPAm-*co*-10%AAc and pNIPAm microgels. We found that kosmotropic ions produced larger responses than chaotropic ions, with exception of Ca^{2+} and Mg^{2+} for etalons composed of pNIPAm-*co*-10%AAc microgels, as the salts contribute to both the salting-out effect and can also minimize the Coulombic repulsion within the microgels. Interestingly, by monitoring the response of the etalons over time, we could conclude that the etalons respond to osmosis in addition to the salting effects as all the salts generated a blue shift in the reflectance spectra. Furthermore, etalons fabricated with microgels without AAc showed higher sensitivity toward salt exposure compared to etalons composed of pNIPAm-*co*-10%AAc microgels. We attribute this to the lack of charge repulsion in the pNIPAm microgel-based devices that enhances their ability to respond to salts. The results here make clear that the microgel response to salt is very complex, although using etalons to probe the dynamics of the salt response, we were able to understand the relative importance of osmosis and "Hofmeister effects" on the microgel hydration state. This is a unique aspect of the work here compared to other studies that utilize measurements at equilibrium conditions to probe these salt interactions. Thus, this system represents a platform to understand many more important processes that define and control polymer hydration state.

Chapter 6

Conclusions and Future Outlook

This thesis was focus on scaling up the etalon fabrication process, and addressing color uniformity and reproducibility issues. Moreover, we explored the ability of the etalons to be used as portable sensors where, for the first time, their color change was characterized using average RGB values. Chapter 2 of this dissertation was focused on fabricating etalons of high color purity and uniformity using doctor blade technique. We compared the uniformity of the etalons prepared using the proposed doctor blade technique with our previous paint-on protocol and investigated the impact of the etalon quality on their pH response measurements. It was observed that doctor blade technique yielded more uniform colored etalons and their color was more consistent from etalon to etalon as demonstrated by their smaller standard deviations on the measured reflectance spectra. Furthermore, it has been shown that the thickness of the top gold layer does not affect the color uniformity and the precision of the pH response measurements for etalons prepared using doctor blade technique were greatly enhanced due to the reproducibility of the fabrication process. However, variations on the microgel diameter prepared in different reaction batches demonstrated to affect the reproducibility of the fabricated etalons. We finally demonstrated that the quality of the fabricated etalons by different individuals had minimal variation. In future, the microgels could be synthesized using free radical precipitation polymerization in the presence of surfactant (SDS) as it can result in more reproducible microgel. Furthermore, the reaction temperature should also be carefully controlled and the reaction scale kept constant. In future, it would be interesting to attach heating blocks to the painting platform so the microgels could be spread on the surface at 35 ^{o}C instead of room temperature and evaluate the quality of the resultant etalon devices.

Subsequently, we used the doctor blade technique to prepare pH responsive etalons and evaluated their ability to be used as portable sensors. For this, we choose to use the etalons to detect the pH of drinking water as it seemed to be the simplest system and also serves as a foundation for future application where we will be using the etalons to detect and quantify other analyte. This was the focus of the Chapter 3 of this thesis. Here, the color change of the etalons in response to pH was characterized using their average RGB values obtained from digital images instead of measuring their reflectance spectra usually performed in our lab. This is an important step to move the technology towards commercialization. Etalons composed of microgels containing different pH responsive comonomers was tested. We found that etalons composed of pNIPAm-*co*-MAAc showed to be more promising as portable sensors for pH measurements as their color change as a function of pH was more gradual using CIE xyY color space. Furthermore, the angle at which the pictures were obtained was extremely important and therefore should be kept constant. Therefore, a 3D printed box was fabricated and the conditions of the experimental set up such as the camera angle and type of LEDs were tested to obtain minimal affect on the RGB values of the digital photos. A quality control was also performed where the etalons were classified in different groups based on their x and y coordinates at pH 4 and 8. Using optimal conditions, the etalons could predict the pH of solution with a MAE as low as 0.2 and as high as 0.6 pH units for complex solutions over a range of pH and ionic strength of 4 – 8 and 150 to 1800 ppm, respectively. In fact, when predicting the pH of real water samples, for the groups with highest frequency, the MAE varied from 0.15 to 0.4 pH units. Furthermore, it was shown that variations in temperature significantly affected in accuracy of the pH measurements. In future, the effect of bicarbonates on the accuracy of pH measurements should be investigated. Also, etalons composed of pNIPAm-*co*-10%AAc showed large response range on the CIE xyY color space. It is worthwhile to decrease the % of AAc and investigate again the performance of these new etalons to predict solution pH. The same applies for VAAc. Furthermore, experiments should be carried out to evaluate the ability to predict the solution temperature and ionic strength using etalons composed of pNIPAm (no pH responsive comonomers) and anionic microgels. Finally, the effect of the gamma correction and demosaicing on the accuracy and precision of the measurements should also be investigated. In this case, the images should be saved as raw Bayer file and the results compared with the previous results where the images were saved as JPG format.

In Chapter 4, we evaluate the performance of the etalons to predict changes in water composition. This project was in collaboration with SolarDew international. Preliminary results performed in their laboratory demonstrated that the etalons can be used to detect changes in the water's ionic strength but further evaluation in field is required to determine the life expectancy of the sensors when submit to rough environmental conditions.

In Chapter 5, the etalons' response to a variety of salt was investigated using reflectance measurements. It was demonstrated that the etalons response could be predicted based on the Hofmeister series and analysis of the response kinetics suggested that osmotic effects could be decoupled from the Hofmeister effects. Furthermore, the details of the response kinetics could be related to the specific ion in solution. In future, the response kinetics for specific salt at different concentration should be obtained. Moreover, it would be interesting to analyse the details of the response kinetics for a mixture of salts and investigate how ion exchange with the polymer occurs. For instance, having the etalons equilibrated with chaotropic ion in solution and monitor the reflectance spectra after the addition of kosmotropic ions.

As we demonstrated that the etalons can be used as portable sensors, future directions include the development of a universal water sensor composed of etalon arrays where each etalon is responsive to a specific stimuli/analyte, such as temperature, ionic strength, pH, heavy metals, phosphates, etc. This can be achieved by changing the chemistry of the microgels and their size as well as changing the chemistry of the etalon's top-Au layer and its thickness. Even though it can be difficult to fabricate an etalon that exclusively respond to one specific stimulus, deconvolution of their responses can be achieved by looking at the individual responses from different sets of etalons to specific parameter/analyte and quantifying the contribution in the total response from the background. For instance, etalons composed of pNIPAm microgels can be used to detect the temperature of aqueous media as the microgels are very sensitive to changes in temperature. However, pNIPAm microgels can also respond to the ionic strength of the medium although with a very low sensitivity, which can compromise the accuracy of the sensors. In this case, when measuring the temperature using pNIPAm microgels, the total response corresponds to the sum of the response to temperature and ionic strength, where the response to temperature is much higher than the response to ionic strength. The ionic strength of the medium can therefore be predicted using etalons composed of anionic microgels as they are more sensitive to the solution ionic strength than temperature. Thus, by knowing the ionic strength, we can subtract its contribution to the total response from the etalons composed of pNIPAm microgels and the temperature can be predicted with higher accuracy. Furthermore, deconvolution of the responses might be also achieved by multidimensional analysis where the right calibration curve for temperature is used for that specific range of ionic strength instead of subtracting the contribution from the ionic strength in the total response.

References

1. Urban, M. W., *Handbook of stimuli-responsive materials*. John Wiley & Sons: 2011.
2. Wei, M.; Gao, Y.; Li, X.; Serpe, M. J. Stimuli-responsive polymers and their applications. *Polymer Chemistry* **2017,** *8* (1), 127-143.
3. Schild, H. G. Poly (N-isopropylacrylamide): experiment, theory and application. *Progress in Polymer Science* **1992,** *17* (2), 163-249.
4. Hoffman, A. S. "Intelligent" polymers in medicine and biotechnology. *Artificial Organs* **1995,** *19* (5), 458-467.
5. Amador-Vargas, S.; Dominguez, M.; León, G.; Maldonado, B.; Murillo, J.; Vides, G. L. Leaf-folding response of a sensitive plant shows context-dependent behavioral plasticity. *Plant Ecology* **2014,** *215* (12), 1445-1454.
6. Teyssier, J.; Saenko, S. V.; Van Der Marel, D.; Milinkovitch, M. C. Photonic crystals cause active colour change in chameleons. *Nature Communications* **2015,** *6*, 6368.
7. Forterre, Y.; Skotheim, J. M.; Dumais, J.; Mahadevan, L. How the Venus flytrap snaps. *Nature* **2005,** *433* (7024), 421-425.
8. Atamian, H. S.; Creux, N. M.; Brown, E. A.; Garner, A. G.; Blackman, B. K.; Harmer, S. L. Circadian regulation of sunflower heliotropism, floral orientation, and pollinator visits. *Science* **2016,** *353* (6299), 587-590.
9. Kocak, G.; Tuncer, C.; Bütün, V. pH-Responsive polymers. *Polymer Chemistry* **2017,** *8* (1), 144-176.
10. Dai, S.; Ravi, P.; Tam, K. C. pH-Responsive polymers: synthesis, properties and applications. *Soft Matter* **2008,** *4* (3), 435-449.
11. Zhang, R.; Tang, M.; Bowyer, A.; Eisenthal, R.; Hubble, J. A novel pH-and ionic-strength-sensitive carboxy methyl dextran hydrogel. *Biomaterials* **2005,** *26* (22), 4677-4683.
12. Karg, M.; Pastoriza-Santos, I.; Rodriguez-Gonzalez, B.; von Klitzing, R.; Wellert, S.; Hellweg, T. Temperature, pH, and ionic strength induced changes of the swelling behavior of PNIPAM− poly (allylacetic acid) copolymer microgels. *Langmuir* **2008,** *24* (12), 6300-6306.
13. Cui, J.; Del Campo, A. Photo-responsive polymers: properties, synthesis and applications. *Smart polymers and their applications* **2014**, 93-133.
14. Irie, M. Photoresponsive polymers. *New Polymer Materials* **1990**, 27-67.

15. Yan, Q.; Han, D.; Zhao, Y. Main-chain photoresponsive polymers with controlled location of light-cleavable units: from synthetic strategies to structural engineering. *Polymer Chemistry* **2013,** *4* (19), 5026-5037.

16. Shan, X.-C.; Zhang, H.-B.; Chen, L.; Wu, M.-Y.; Jiang, F.-L.; Hong, M.-C. Multistimuli-responsive luminescent material reversible switching colors via temperature and mechanical force. *Crystal Growth & Design* **2013,** *13* (4), 1377-1381.

17. Caruso, M. M.; Davis, D. A.; Shen, Q.; Odom, S. A.; Sottos, N. R.; White, S. R.; Moore, J. S. Mechanically-induced chemical changes in polymeric materials. *Chemical Reviews* **2009,** *109* (11), 5755-5798.

18. Wiggins, K. M.; Brantley, J. N.; Bielawski, C. W. Methods for activating and characterizing mechanically responsive polymers. *Chemical Society Reviews* **2013,** *42* (17), 7130-7147.

19. Davis, D. A.; Hamilton, A.; Yang, J.; Cremar, L. D.; Van Gough, D.; Potisek, S. L.; Ong, M. T.; Braun, P. V.; Martínez, T. J.; White, S. R. Force-induced activation of covalent bonds in mechanoresponsive polymeric materials. *Nature* **2009,** *459* (7243), 68-72.

20. Islam, M. R.; Serpe, M. J. Poly (N-isopropylacrylamide) microgel-based thin film actuators for humidity sensing. *RSC Advances* **2014,** *4* (60), 31937-31940.

21. de Haan, L. T.; Verjans, J. M.; Broer, D. J.; Bastiaansen, C. W.; Schenning, A. P. Humidity-responsive liquid crystalline polymer actuators with an asymmetry in the molecular trigger that bend, fold, and curl. *Journal of the American Chemical Society* **2014,** *136* (30), 10585-10588.

22. Rajagopalan, M.; Jeon, J.-H.; Oh, I.-K. Electric-stimuli-responsive bending actuator based on sulfonated polyetherimide. *Sensors and Actuators B: Chemical* **2010,** *151* (1), 198-204.

23. Zrínyi, M. Magnetically responsive polymer gels and elastomers: properties, synthesis and applications. In *Smart Polymers and their Applications*, Elsevier: 2014; pp 134-165.

24. Tanaka, T.; Nishio, I.; Sun, S.-T.; Ueno-Nishio, S. Collapse of gels in an electric field. *Science* **1982,** *218* (4571), 467-469.

25. Kim, E.; Lee, J.; Kim, D.; Lee, K. E.; Han, S. S.; Lim, N.; Kang, J.; Park, C. G.; Kim, K. Solvent-responsive polymer nanocapsules with controlled permeability: encapsulation and release of a fluorescent dye by swelling and deswelling. *Chemical Communications* **2009,** (12), 1472-1474.

26. Dong, J.; Zhou, J. Solvent-responsive behavior of polymer-brush-modified amphiphilic gold nanoparticles. *Macromolecular Theory and Simulations* **2013,** *22* (3), 174-186.

27. Zelzer, M.; Ulijn, R. Enzyme-responsive polymers: properties, synthesis and applications. *Smart Polymers and their Applications* **2014**, 166-203.

28. Colson, Y. L.; Grinstaff, M. W. Biologically responsive polymeric nanoparticles for drug delivery. *Advanced Materials* **2012,** *24* (28), 3878-3886.

29. Duarte, A. R. C.; Mano, J. F.; Reis, R. L. Thermosensitive polymeric matrices for three-dimensional cell culture strategies. *Acta Biomaterialia* **2011,** *7* (2), 526-529.

30. Chang, K.; Rubright, N. C.; Lowery, P. D.; Taite, L. J. Structural optimization of highly branched thermally responsive polymers as a means of controlling transition temperature. *Journal of Polymer Science Part A: Polymer Chemistry* **2013,** *51* (9), 2068-2078.

31. Roy, D.; Brooks, W. L.; Sumerlin, B. S. New directions in thermoresponsive polymers. *Chemical Society Reviews* **2013,** *42* (17), 7214-7243.

32. Zhu, Y.; Batchelor, R.; Lowe, A. B.; Roth, P. J. Design of thermoresponsive polymers with aqueous lcst, ucst, or both: Modification of a reactive poly (2-vinyl-4, 4-dimethylazlactone) scaffold. *Macromolecules* **2016,** *49* (2), 672-680.

33. Seuring, J.; Agarwal, S. Polymers with upper critical solution temperature in aqueous solution. *Macromolecular Rapid Communications* **2012,** *33* (22), 1898-1920.

34. Seuring, J.; Agarwal, S. Polymers with upper critical solution temperature in aqueous solution: unexpected properties from known building blocks. *ACS Macro Letters* **2013**, 597-600.

35. Hoogenboom, R. Temperature-Responsive Polymers: Properties, Synthesis, and Applications. *Smart Polymers and their Applications* **2019**, 13-44.

36. Kudaibergenov, S.; Jaeger, W.; Laschewsky, A. Polymeric betaines: synthesis, characterization, and application. *Supramolecular Polymers Polymeric Betains Oligomers* **2006**, 157-224.

37. Seuring, J.; Agarwal, S. First example of a universal and cost-effective approach: Polymers with tunable upper critical solution temperature in water and electrolyte solution. *Macromolecules* **2012,** *45* (9), 3910-3918.

38. Glatzel, S.; Badi, N.; Päch, M.; Laschewsky, A.; Lutz, J.-F. Well-defined synthetic polymers with a protein-like gelation behavior in water. *Chemical Communications* **2010,** *46* (25), 4517-4519.

39. Heskins, M.; Guillet, J. E. Solution properties of poly (N-isopropylacrylamide). *Journal of Macromolecular Science—Chemistry* **1968,** *2* (8), 1441-1455.

40. Maeda, Y.; Higuchi, T.; Ikeda, I. Change in hydration state during the coil− globule transition of aqueous solutions of poly (N-isopropylacrylamide) as evidenced by FTIR spectroscopy. *Langmuir* **2000,** *16* (19), 7503-7509.

41. Gorelov, A.; Du Chesne, A.; Dawson, K. Phase separation in dilute solutions of poly (N-isopropylacrylamide). *Physica A: Statistical Mechanics and its Applications* **1997,** *240* (3-4), 443-452.

42. Dawson, K.; Gorelov, A.; Timoshenko, E.; Kuznetsov, Y. A.; Du Chesne, A. Formation of mesoglobules from phase separation in dilute polymer solutions: a study in experiment, theory, and applications. *Physica A: Statistical Mechanics and its Applications* **1997,** *244* (1-4), 68-80.

43. Chan, K.; Pelton, R.; Zhang, J. On the formation of colloidally dispersed phase-separated poly (N-isopropylacrylamide). *Langmuir* **1999,** *15* (11), 4018-4020.

44. Kujawa, P.; Aseyev, V.; Tenhu, H.; Winnik, F. M. Temperature-sensitive properties of poly (N-isopropylacrylamide) mesoglobules formed in dilute aqueous solutions heated above their demixing point. *Macromolecules* **2006,** *39* (22), 7686-7693.

45. Yoshida, R.; Sakai, K.; Okano, T.; Sakurai, Y. Modulating the phase transition temperature and thermosensitivity in N-isopropylacrylamide copolymer gels. *Journal of Biomaterials Science, Polymer Edition* **1995,** *6* (6), 585-598.

46. Jain, K.; Vedarajan, R.; Watanabe, M.; Ishikiriyama, M.; Matsumi, N. Tunable LCST behavior of poly (N-isopropylacrylamide/ionic liquid) copolymers. *Polymer Chemistry* **2015,** *6* (38), 6819-6825.

47. Liu, H.; Zhu, X. Lower critical solution temperatures of N-substituted acrylamide copolymers in aqueous solutions. *Polymer* **1999,** *40* (25), 6985-6990.

48. Chen, J.-K.; Chang, C.-J. Fabrications and applications of stimulus-responsive polymer films and patterns on surfaces: A review. *Materials* **2014,** *7* (2), 805-875.

49. Guan, Y.; Zhang, Y. PNIPAM microgels for biomedical applications: from dispersed particles to 3D assemblies. *Soft Matter* **2011,** *7* (14), 6375-6384.

50. Rudin, A.; Choi, P. The elements of polymer science and engineering. *Academic press*: **2012**.

51. Kuckling, D.; Urban, M. W. Synthetic and physicochemical aspects of advanced stimuli-responsive polymers. *Handbook of Stimuli-Responsive Materials* **2011**, 1-26.

52. Matyjaszewski, K.; Gaynor, S.; Greszta, D.; Mardare, D.; Shigemoto, T. 'Living'and controlled radical polymerization. *Journal of Physical Organic Chemistry* **1995,** *8* (4), 306-315.

53. Kato, M.; Kamigaito, M.; Sawamoto, M.; Higashimura, T. Polymerization of methyl methacrylate with the carbon tetrachloride/dichlorotris-(triphenylphosphine) ruthenium (II)/methylaluminum bis (2, 6-di-tert-butylphenoxide) initiating system: possibility of living radical polymerization. *Macromolecules* **1995,** *28* (5), 1721-1723.

54. Otsu, T.; Matsumoto, A.; Tazaki, T. Radical polymerization of methyl methacrylate with some 1, 2-disubstituted tetraphenylethanes as thermal iniferters. *Polymer Bulletin* **1987,** *17* (4), 323-330.

55. Convertine, A. J.; Ayres, N.; Scales, C. W.; Lowe, A. B.; McCormick, C. L. Facile, controlled, room-temperature RAFT polymerization of N-isopropylacrylamide. *Biomacromolecules* **2004,** *5* (4), 1177-1180.

56. Pelton, R. Temperature-sensitive aqueous microgels. *Advances in Colloid and Interface Science* **2000,** *85* (1), 1-33.

57. Park, T. G.; Hoffman, A. S. Preparation of large, uniform size temperature-sensitive hydrogel beads. *Journal of Polymer Science Part A: Polymer Chemistry* **1992,** *30* (3), 505-507.

58. Pelton, R.; Chibante, P. Preparation of aqueous latices with N-isopropylacrylamide. *Colloids and Surfaces* **1986,** *20* (3), 247-256.

59. Pelton, R.; Pelton, H.; Morphesis, A.; Rowell, R. Particle sizes and electrophoretic mobilities of poly (N-isopropylacrylamide) latex. *Langmuir* **1989,** *5* (3), 816-818.

60. Wu, X.; Pelton, R.; Hamielec, A.; Woods, D.; McPhee, W. The kinetics of poly (N-isopropylacrylamide) microgel latex formation. *Colloid and Polymer Science* **1994,** *272* (4), 467-477.

61. Nayak, S.; Lyon, L. A. Soft nanotechnology with soft nanoparticles. *Angewandte Chemie International Edition* **2005,** *44* (47), 7686-7708.

62. Pich, A.; Richtering, W. Microgels by precipitation polymerization: synthesis, characterization, and functionalization. *Chemical Design of Responsive Microgels* **2010**, 1-37.

63. Snowden, M.; Vincent, B. The temperature-controlled flocculation of crosslinked latex particles. *ACS Chemical Communications* **1992,** (16), 1103-1105.

64. Daly, E.; Saunders, B. R. A study of the effect of electrolyte on the swelling and stability of poly (N-isopropylacrylamide) microgel dispersions. *Langmuir* **2000,** *16* (13), 5546-5552.

65. Meng, Z.; Cho, J. K.; Debord, S.; Breedveld, V.; Lyon, L. A. Crystallization behavior of soft, attractive microgels. *The Journal of Physical Chemistry B* **2007,** *111* (25), 6992-6997.

66. Meng, Z.; Smith, M. H.; Lyon, L. A. Temperature-programmed synthesis of micron-sized multi-responsive microgels. *Colloid and Polymer Science* **2009,** *287* (3), 277-285.

67. Goodwin, J. W.; Ottewill, R. H.; Pelton, R.; Vianello, G.; Yates, D. E. Control of particle size in the formation of polymer latices. *British Polymer Journal* **1978,** *10* (3), 173-180.

68. Shimizu, H.; Wada, R.; Okabe, M. Preparation and characterization of micrometer-sized poly (N-isopropylacrylamide) hydrogel particles. *Polymer Journal* **2009,** *41* (9), 771-777.

69. McPhee, W.; Tam, K. C.; Pelton, R. Poly (N-isopropylacrylamide) latices prepared with sodium dodecyl sulfate. *Journal of Colloid and Interface Science* **1993,** *156* (1), 24-30.

70. Nolan, C. M.; Reyes, C. D.; Debord, J. D.; Garcia, A. J.; Lyon, L. A. Phase transition behavior, protein adsorption, and cell adhesion resistance of poly (ethylene glycol) cross-linked microgel particles. *Biomacromolecules* **2005,** *6* (4), 2032-2039.

71. Keerl, M.; Richtering, W. Synergistic depression of volume phase transition temperature in copolymer microgels. *Colloid and Polymer Science* **2007,** *285* (4), 471-474.

72. Keerl, M.; Smirnovas, V.; Winter, R.; Richtering, W. Copolymer microgels from mono- and disubstituted acrylamides: phase behavior and hydrogen bonds. *Macromolecules* **2008,** *41* (18), 6830-6836.

73. Flory, P. J. Principles of polymer chemistry. *Cornell University Press:* **1953**.

74. Hu, L.; Serpe, M. J. Controlling the response of color tunable poly (N-isopropylacrylamide) microgel-based etalons with hysteresis. *Chemical Communications* **2013,** *49* (26), 2649-2651.

75. Hirotsu, S.; Hirokawa, Y.; Tanaka, T. Volume-phase transitions of ionized N-isopropylacrylamide gels. *The Journal of Chemical Physics* **1987,** *87* (2), 1392-1395.

76. Snowden, M. J.; Chowdhry, B. Z.; Vincent, B.; Morris, G. E. Colloidal copolymer microgels of N-isopropylacrylamide and acrylic acid: pH, ionic strength and temperature effects. *Journal of the Chemical Society, Faraday Transactions* **1996,** *92* (24), 5013-5016.

77. Kratz, K.; Hellweg, T.; Eimer, W. Influence of charge density on the swelling of colloidal poly (N-isopropylacrylamide-co-acrylic acid) microgels. *Colloids and Surfaces A: Physicochemical and Engineering Aspects* **2000,** *170* (2-3), 137-149.

78. Sorrell, C. D.; Carter, M. C.; Serpe, M. J. Color Tunable Poly (N-Isopropylacrylamide)-co-Acrylic Acid Microgel–Au Hybrid Assemblies. *Advanced Functional Materials* **2011,** *21* (3), 425-433.

79. Sorrell, C. D.; Serpe, M. J. Reflection order selectivity of color-tunable poly (N-isopropylacrylamide) microgel based etalons. *Advanced Materials* **2011,** *23* (35), 4088-4092.

80. Zhang, Y.; Carvalho, W. S.; Fang, C.; Serpe, M. J. Volatile organic compound vapor detection with responsive microgel-based etalons. *Sensors and Actuators B: Chemical* **2019,** *290*, 520-526.

81. Wei, M.; Serpe, M. J. Temperature–Light Dual-Responsive Au@ PNIPAm Core-Shell Microgel-Based Optical Devices. *Particle & Particle Systems Characterization* **2019,** *36* (1), 1800326.

82. Shu, T.; Shen, Q.; Wan, Y.; Zhang, W.; Su, L.; Zhang, X.; Serpe, M. J. Silver nanoparticle-loaded microgel-based etalons for H_2O_2 sensing. *RSC Advances* **2018,** *8* (28), 15567-15574.

83. Jiang, Y.; Colazo, M. G.; Serpe, M. J. Poly (N-isopropylacrylamide) microgel-based etalons for the label-free quantitation of estradiol-17β in aqueous solutions and milk samples. *Analytical and Bioanalytical Chemistry* **2018,** *410* (18), 4397-4407.

84. Zhang, W.; Wei, M.; Carvalho, W. S.; Serpe, M. J. Enzyme-assisted polymer film degradation-enabled biomolecule sensing with poly (N-isopropylacrylamide)-based optical devices. *Analytica Chimica Acta* **2018,** *999*, 139-143.

85. Islam, M. R.; Serpe, M. J. A novel label-free colorimetric assay for DNA concentration in solution. *Analytica Chimica Acta* **2014,** *843*, 83-88.

86. Bonifacio, L. D.; Lotsch, B. V.; Puzzo, D. P.; Scotognella, F.; Ozin, G. A. Stacking the nanochemistry deck: structural and compositional diversity in one-dimensional photonic crystals. *Advanced Materials* **2009,** *21* (16), 1641-1646.

87. Liu, W.; Ma, H.; Walsh, A. Advance in photonic crystal solar cells. *Renewable and Sustainable Energy Reviews* **2019,** *116*, 109436.

88. Bermel, P.; Luo, C.; Zeng, L.; Kimerling, L. C.; Joannopoulos, J. D. Improving thin-film crystalline silicon solar cell efficiencies with photonic crystals. *Optics Express* **2007,** *15* (25), 16986-17000.

89. Chutinan, A.; Kherani, N. P.; Zukotynski, S. High-efficiency photonic crystal solar cell architecture. *Optics Express* **2009,** *17* (11), 8871-8878.

90. Xu, H.; Wu, P.; Zhu, C.; Elbaz, A.; Gu, Z. Z. Photonic crystal for gas sensing. *Journal of Materials Chemistry C* **2013,** *1* (38), 6087-6098.

91. Ge, J.; Yin, Y. Responsive photonic crystals. *Angewandte Chemie International Edition* **2011,** *50* (7), 1492-1522.

92. Xu, D.; Yu, H.; Xu, Q.; Xu, G.; Wang, K. Thermoresponsive Photonic Crystal: Synergistic Effect of Poly (N-isopropylacrylamide)-co-acrylic Acid and Morpho Butterfly Wing. *ACS Applied Materials & Interfaces* **2015,** *7* (16), 8750-8756.

93. Cunningham, B. T.; Zhang, M.; Zhuo, Y.; Kwon, L.; Race, C. Recent advances in biosensing with photonic crystal surfaces: a review. *IEEE Sensors Journal* **2015,** *16* (10), 3349-3366.

94. Wu, E. C.; Andrew, J. S.; Cheng, L.; Freeman, W. R.; Pearson, L.; Sailor, M. J. Real-time monitoring of sustained drug release using the optical properties of porous silicon photonic crystal particles. *Biomaterials* **2011,** *32* (7), 1957-1966.

95. Mekis, A.; Chen, J.; Kurland, I.; Fan, S.; Villeneuve, P. R.; Joannopoulos, J. High transmission through sharp bends in photonic crystal waveguides. *Physical Review Letters* **1996,** *77* (18), 3787.

96. McNab, S. J.; Moll, N.; Vlasov, Y. A. Ultra-low loss photonic integrated circuit with membrane-type photonic crystal waveguides. *Optics Express* **2003,** *11* (22), 2927-2939.

97. Arsenault, A. C.; Puzzo, D. P.; Manners, I.; Ozin, G. A. Photonic-crystal full-colour displays. *Nature Photonics* **2007,** *1* (8), 468-472.

98. Wiesmann, C.; Bergenek, K.; Linder, N.; Schwarz, U. T. Photonic crystal LEDs–designing light extraction. *Laser & Photonics Reviews* **2009,** *3* (3), 262-286.

99. Shen, H.; Wang, Z.; Wu, Y.; Yang, B. One-dimensional photonic crystals: fabrication, responsiveness and emerging applications in 3D construction. *RSC Advances* **2016,** *6* (6), 4505-4520.

100. Yoshino, T.; Kurosawa, K.; Itoh, K.; Ose, T. Fiber-optic Fabry-Perot interferometer and its sensor applications. *IEEE Transactions on Microwave Theory and Techniques* **1982,** *30* (10), 1612-1621.

101. Vaughan, M. The Fabry-Perot interferometer: history, theory, practice and applications. *Routledge:* **2017**.

102. Saunders, B. R. On the structure of poly (N-isopropylacrylamide) microgel particles. *Langmuir* **2004,** *20* (10), 3925-3932.

103. Zhou, S.; Chu, B. Synthesis and volume phase transition of poly (methacrylic acid-co-N-isopropylacrylamide) microgel particles in water. *The Journal of Physical Chemistry B* **1998,** *102* (8), 1364-1371.

104. Schmidt, S.; Hellweg, T.; von Klitzing, R. Packing density control in P (NIPAM-co-AAc) microgel monolayers: effect of surface charge, pH, and preparation technique. *Langmuir* **2008,** *24* (21), 12595-12602.

105. Pinkrah, V.; Snowden, M.; Mitchell, J.; Seidel, J.; Chowdhry, B.; Fern, G. Physicochemical properties of poly (N-isopropylacrylamide-co-4-vinylpyridine) cationic polyelectrolyte colloidal microgels. *Langmuir* **2003,** *19* (3), 585-590.

106. Garcia, A.; Marquez, M.; Cai, T.; Rosario, R.; Hu, Z.; Gust, D.; Hayes, M.; Vail, S. A.; Park, C.-D. Photo-, thermally, and pH-responsive microgels. *Langmuir* **2007,** *23* (1), 224-229.

107. Hoare, T.; Pelton, R. Highly pH and temperature responsive microgels functionalized with vinylacetic acid. *Macromolecules* **2004,** *37* (7), 2544-2550.

108. Sorrell, C. D.; Carter, M. C.; Serpe, M. J. A "paint-on" protocol for the facile assembly of uniform microgel coatings for color tunable etalon fabrication. *ACS Applied Materials and Interfaces* **2011,** *3* (4), 1140-1147.

109. Sorrell, C. D.; Serpe, M. J. Glucose sensitive poly (N-isopropylacrylamide) microgel based etalons. *Analytical and Bioanalytical Chemistry* **2012,** *402* (7), 2385-2393.

110. Islam, M. R.; Serpe, M. J. Label-free detection of low protein concentration in solution using a novel colorimetric assay. *Biosensors and Bioelectronics* **2013,** *49*, 133-138.

111. Gao, Y.; Zago, G. P.; Jia, Z.; Serpe, M. J. Controlled and triggered small molecule release from a confined polymer film. *ACS Applied Materials and Interfaces* **2013,** *5* (19), 9803-9808.

112. Guo, S.; Carvalho, W. S. P.; Wong, D.; Serpe, M. J. Alkanethiol Molecular Barriers for Controlling Small Molecule Release Kinetics from a Microgel-Based Reservoir Device. *ACS Applied Materials & Interfaces* **2019**.

113. Mistler, R. E.; Twiname, E. R. Tape casting: theory and practice. *American ceramic society*: **2000**.

114. Edgar, W. Doctor blade for paper coating apparatus. *Google Patents:* **1956**.

115. Grommek, S. Doctor blade control mechanism, particularly for use in printing presses. *Google Patents*: **1974**.

116. Berni, A.; Mennig, M.; Schmidt, H. Doctor Blade. *Sol-Gel Technologies for Glass Producers and Users* **2004**, 89-92.

117. Yang, H.; Jiang, P. Large-scale colloidal self-assembly by doctor blade coating. *Langmuir* **2010,** *26* (16), 13173-13182.

118. Ahiabu, A.; Serpe, M. J. Rapidly responding pH-and temperature-responsive poly (N-Isopropylacrylamide)-based microgels and assemblies. *ACS Omega* **2017,** *2* (5), 1769-1777.

119. Debord, J. D.; Lyon, L. A. Synthesis and characterization of pH-responsive copolymer microgels with tunable volume phase transition temperatures. *Langmuir* **2003,** *19* (18), 7662-7664.

120. Bales, G. S.; Bruinsma, R.; Eklund, E. A.; Karunasiri, R.; Rudnick, J.; Zangwill, A. Growth and erosion of thin solid films. *Science* **1990,** *249* (4966), 264-268.

121. Mura, S.; Nicolas, J.; Couvreur, P. Stimuli-responsive nanocarriers for drug delivery. *Nature Materials* **2013,** *12* (11), 991-1003.

122. Lupitskyy, R.; Roiter, Y.; Tsitsilianis, C.; Minko, S. From smart polymer molecules to responsive nanostructured surfaces. *Langmuir* **2005,** *21* (19), 8591-8593.

123. Stuart, M. A. C.; Huck, W. T.; Genzer, J.; Müller, M.; Ober, C.; Stamm, M.; Sukhorukov, G. B.; Szleifer, I.; Tsukruk, V. V.; Urban, M. Emerging applications of stimuli-responsive polymer materials. *Nature Materials* **2010,** *9* (2), 101-113.

124. Al-Manasir, N.; Zhu, K.; Kjøniksen, A.-L.; Knudsen, K. D.; Karlsson, G.; Nystrom, B. Effects of temperature and pH on the contraction and aggregation of microgels in aqueous suspensions. *The Journal of Physical Chemistry B* **2009,** *113* (32), 11115-11123.

125. Wu, C.; Zhou, S. Effects of surfactants on the phase transition of poly (N-isopropylacrylamide) in water. *Journal of Polymer Science Part B: Polymer Physics* **1996,** *34* (9), 1597-1604.

126. Kawasaki, H.; Sasaki, S.; Maeda, H. Effect of introduced electric charge on the volume phase transition of N-isopropylacrylamide gels. *The Journal of Physical Chemistry B* **1997,** *101* (21), 4184-4187.

127. Zhang, Y.; Furyk, S.; Bergbreiter, D. E.; Cremer, P. S. Specific ion effects on the water solubility of macromolecules: PNIPAM and the Hofmeister series. *Journal of the American Chemical Society* **2005,** *127* (41), 14505-14510.

128. Winnik, F. M.; Ringsdorf, H.; Venzmer, J. Methanol-water as a co-nonsolvent system for poly (N-isopropylacrylamide). *Macromolecules* **1990,** *23* (8), 2415-2416.

129. Zhang, H. F.; Zhong, H.; Zhang, L. L.; Chen, S. B.; Zhao, Y. J.; Zhu, Y. L.; Wang, J. T. Modulate the phase transition temperature of hydrogels with both thermosensitivity and biodegradability. *Carbohydrate Polymers* **2010,** *79* (1), 131-136.

130. Hoare, T.; Pelton, R. Functional group distributions in carboxylic acid containing poly (N-isopropylacrylamide) microgels. *Langmuir* **2004,** *20* (6), 2123-2133.

131. Islam, M. R.; Serpe, M. J. Polymer-based devices for the label-free detection of DNA in solution: low DNA concentrations yield large signals. *Analytical and Bioanalytical Chemistry* **2014,** *406* (19), 4777-4783.

132. Islam, M. R.; Serpe, M. J. Polyelectrolyte mediated intra and intermolecular crosslinking in microgel-based etalons for sensing protein concentration in solution. *Chemical Communications* **2013,** *49* (26), 2646-2648.

133. Zhang, Q. M.; Berg, D.; Duan, J.; Mugo, S. M.; Serpe, M. J. Optical devices constructed from ferrocene-modified microgels for H2O2 sensing. *ACS Applied Materials and Interfaces* **2016,** *8* (40), 27264-27269.

134. Zhang, Q. M.; Ahiabu, A.; Gao, Y.; Serpe, M. J. CO 2-switchable poly (N-isopropylacrylamide) microgel-based etalons. *Journal of Materials Chemistry C* **2015,** *3* (3), 495-498.

135. Zhang, Q. M.; Berg, D.; Mugo, S. M.; Serpe, M. J. Lipase-modified pH-responsive microgel-based optical device for triglyceride sensing. *Chemical Communications* **2015,** *51* (47), 9726-9728.

136. Jiang, Y.; Colazo, M. G.; Serpe, M. J. Poly (N-isopropylacrylamide) microgel-based sensor for progesterone in aqueous samples. *Colloid and Polymer Science* **2016,** *294* (11), 1733-1741.

137. Islam, M. R.; Xie, S.; Huang, D.; Smyth, K.; Serpe, M. J. Poly (N-Isopropylacrylamide) microgel-based optical devices for humidity sensing. *Analytica chimica acta* **2015,** *898*, 101-108.

138. Islam, M. R.; Serpe, M. J. Poly (N-isopropylacrylamide) microgel-based etalons and etalon arrays for determining the molecular weight of polymers in solution. *APL Materials* **2013,** *1* (5), 052108.

139. Islam, M. R.; Serpe, M. J. Penetration of polyelectrolytes into charged poly (N-isopropylacrylamide) microgel layers confined between two surfaces. *Macromolecules* **2013,** *46* (4), 1599-1606.

140. Ibraheem, N. A.; Hasan, M. M.; Khan, R. Z.; Mishra, P. K. Understanding color models: a review. *ARPN Journal of Science and Technology* **2012,** *2* (3), 265-275.

141. Süsstrunk, S.; Buckley, R.; Swen, S. Standard RGB color spaces. *Color and Imaging Conference, Society for Imaging Science and Technology* **1999**, 127-134.

142. Adams Jr, J. E. Interactions between color plane interpolation and other image processing functions in electronic photography. *Cameras and Systems for Electronic Photography and Scientific Imaging, International Society for Optics and Photonics* **1995**, 144-151.

143. Westland, S. Review of the CIE system of colorimetry and its use in dentistry. *Journal of Esthetic and Restorative Dentistry* **2003,** *15*, S5-S12.

144. Poynton, C. The CIE system of colorimetry. *Digital Video and HDTV: Algorithms and Interfaces* **2012**, 211-231.

145. Wyman, C.; Sloan, P.-P.; Shirley, P. Simple analytic approximations to the CIE XYZ color matching functions. *Journal of Computer Graphics Techniques* **2013,** *2* (2), 1-11.

146. Boynton, R. M. Human color perception. In *Science of Vision*, Springer: 1990; pp 211-253.

147. Judd, D. B. Ideal color space. *Color Eng* **1970,** *8* (2), 36-52.

148. Kerr, D. A. The CIE XYZ and xyY color spaces. *Colorimetry* **2010,** *1* (1), 1-16.

149. Pagnutti, M. A.; Ryan, R. E.; Cazenavette, G. J.; Gold, M. J.; Harlan, R.; Leggett, E.; Pagnutti, J. F. Laying the foundation to use Raspberry Pi 3 V2 camera module imagery for scientific and engineering purposes. *Journal of Electronic Imaging* **2017,** *26* (1), 013014.

150. MacQueen, J. Some methods for classification and analysis of multivariate observations. *Proceedings of the Fifth Berkeley Symposium on Mathematical Statistics and Probability* **1967**, 281-297.

151. Wagstaff, K.; Cardie, C.; Rogers, S.; Schrödl, S. Constrained k-means Clustering with Background Knowledge. *ICML* **2001**, 577-584.

152. Likas, A.; Vlassis, N.; Verbeek, J. J. The global k-means clustering algorithm. *Pattern Recognition* **2003,** *36* (2), 451-461.

153. Fernández-Nieves, A.; Fernández-Barbero, A.; Vincent, B.; De Las Nieves, F. Charge controlled swelling of microgel particles. *Macromolecules* **2000,** *33* (6), 2114-2118.

154. Bodnarchuk, M. S.; Doncom, K. E.; Wright, D. B.; Heyes, D. M.; Dini, D.; O'Reilly, R. K. Polyelectrolyte p K a from experiment and molecular dynamics simulation. *RSC Advances* **2017,** *7* (32), 20007-20014.

155. Colombani, O.; Lejeune, E.; Charbonneau, C. l.; Chassenieux, C.; Nicolai, T. Ionization of amphiphilic acidic block copolymers. *The Journal of Physical Chemistry B* **2012,** *116* (25), 7560-7565.

156. Kawasaki, H.; Sasaki, S.; Maeda, H. Effect of pH on the volume phase transition of copolymer gels of N-isopropylacrylamide and sodium acrylate. *The Journal of Physical Chemistry B* **1997,** *101* (26), 5089-5093.

157. Organization, W. H. Drinking-water. **2019**.

158. Sheppard, N. F.; Tucker, R. C.; Wu, C. Electrical conductivity measurements using microfabricated interdigitated electrodes. *Analytical Chemistry* **1993,** *65* (9), 1199-1202.

159. Ribeiro, A. L.; Ramos, H. M. G.; Ramos, P. M.; Pereira, J. Inductive conductivity cell for water salinity monitoring. *Proceedings of XVIII Imeko World Congress, Metrology for a Sustainable Development* **2006**, 0018-9464.

160. Dai, Z.; Ngai, T. Microgel particles: The structure-property relationships and their biomedical applications. *Journal of Polymer Science Part A: Polymer Chemistry* **2013,** *51* (14), 2995-3003.

161. Saunders, B. R.; Laajam, N.; Daly, E.; Teow, S.; Hu, X.; Stepto, R. Microgels: From responsive polymer colloids to biomaterials. *Advances in Colloid and Interface Science* **2009,** *147*, 251-262.

162. Blackburn, W. H.; Lyon, L. A. Size-controlled synthesis of monodisperse core/shell nanogels. *Colloid and Polymer Science* **2008,** *286* (5), 563-569.

163. Plamper, F. A.; Richtering, W. Functional microgels and microgel systems. *Accounts of Chemical Research* **2017,** *50* (2), 131-140.

164. Horkay, F.; Tasaki, I.; Basser, P. J. Osmotic swelling of polyacrylate hydrogels in physiological salt solutions. *Biomacromolecules* **2000,** *1* (1), 84-90.

165. Schroeder, R.; Rudov, A. A.; Lyon, L. A.; Richtering, W.; Pich, A.; Potemkin, I. I. Electrostatic interactions and osmotic pressure of counterions control the pH-dependent swelling and collapse of polyampholyte microgels with random distribution of ionizable groups. *Macromolecules* **2015,** *48* (16), 5914-5927.

166. Okay, O.; Sariişik, S. B.; Zor, S. D. Swelling behavior of anionic acrylamide-based hydrogels in aqueous salt solutions: Comparison of experiment with theory. *Journal of Applied Polymer Science* **1998,** *70* (3), 567-575.

167. Valdez, P.; Mehrabian, A. Effects of color on emotions. *Journal of Experimental psychology: General* **1994,** *123* (4), 394.

168. Wexner, L. B. The degree to which colors (hues) are associated with mood-tones. *Journal of Applied Psychology* **1954,** *38* (6), 432.

169. Jones, C. D.; Lyon, L. A. Synthesis and characterization of multiresponsive core− shell microgels. *Macromolecules* **2000,** *33* (22), 8301-8306.

170. Kunz, W.; Henle, J.; Ninham, B. W. 'Zur Lehre von der Wirkung der Salze' (about the science of the effect of salts): Franz Hofmeister's historical papers. *Current Opinion in Colloidoid and Interface Science* **2004,** *9* (1-2), 19-37.

171. Collins, K. D.; Washabaugh, M. W. The Hofmeister effect and the behaviour of water at interfaces. *Quarterly Reviews of Biophysics* **1985,** *18* (4), 323-422.

172. Gurau, M. C.; Lim, S.-M.; Castellana, E. T.; Albertorio, F.; Kataoka, S.; Cremer, P. S. On the mechanism of the Hofmeister effect. *Journal of the American Chemical Society* **2004,** *126* (34), 10522-10523.

173. Zhang, Y.; Cremer, P. S. Interactions between macromolecules and ions: the Hofmeister series. *Current Opinion in Chemical Biology* **2006,** *10* (6), 658-663.

174. Tadeo, X.; Lopez-Mendez, B.; Castano, D.; Trigueros, T.; Millet, O. Protein Stabilization and the Hofmeister Effect: The Role of Hydrophobic Solvation. *Biophysical Journal* **2009,** *97* (9), 2595-2603.

175. Yan, C. Y.; Mu, T. C. Molecular understanding of ion specificity at the peptide bond. *Physical Chemistry Chemical Physics* **2015,** *17* (5), 3241-3249.

176. Omta, A. W.; Kropman, M. F.; Woutersen, S.; Bakker, H. J. Negligible effect of ions on the hydrogen-bond structure in liquid water. *Science* **2003,** *301* (5631), 347-9.

177. Salis, A.; Bilanicova, D.; Ninham, B. W.; Monduzzi, M. Hofmeister effects in enzymatic activity: Weak and strong electrolyte influences on the activity of Candida rugosa lipase. *Journal of Physical Chemistry B* **2007,** *111* (5), 1149-1156.

178. Baldwin, R. L. How Hofmeister ion interactions affect protein stability. *Biophys J* **1996,** *71* (4), 2056-2063.

179. Gurnev, P. A.; Roark, T. C.; Petrache, H. I.; Sodt, A. J.; Bezrukov, S. M. Cation-Selective Channel Regulated by Anions According to Their Hofmeister Ranking. *Angewandte Chemie Internatinal Edition* **2017,** *56* (13), 3506-3509.

180. Lo Nostro, P.; Ninham, B. W.; Lo Nostro, A.; Pesavento, G.; Fratoni, L.; Baglioni, P. Specific ion effects on the growth rates of Staphylococcus aureus and Pseudomonas aeruginosa. *Physical Biology* **2005,** *2* (1), 1-7.

181. Nagler, K.; Moeller, R. Systematic investigation of germination responses of Bacillus subtilis spores in different high-salinity environments. *FEMS Microbiology Ecology* **2015,** *91* (5).

182. Antonisse, M. M. G.; Snellink-Ruel, B. H. M.; Yigit, I.; Engbersen, J. F. J.; Reinhoudt, D. N. Neutral anion receptors: Synthesis and evaluation as sensing molecules in chemically modified field effect transistors. *Journal of Organic Chemistry* **1997,** *62* (26), 9034-9038.

183. Gupta, V. K.; Ludwig, R.; Agarwal, S. Anion recognition through modified calixarenes: a highly selective sensor for monohydrogen phosphate. *Analytica Chimica Acta* **2005,** *538* (1-2), 213-218.

184. Schazmann, B.; Diamond, D. Improved nitrate sensing using ion selective electrodes based on urea-calixarene ionophores. *New Journal of Chemistry* **2007,** *31* (4), 587-592.

185. Wei, M. L.; Gao, Y. F.; Li, X.; Serpe, M. J. Stimuli-responsive polymers and their applications. *Polymer Chemistry* **2017,** *8* (1), 127-143.

186. Carvalho, W. S. P.; Wei, M. L.; Ikpo, N.; Gao, Y. F.; Serpe, M. J. Polymer-Based Technologies for Sensing Applications. *Analytical Chemistry* **2018,** *90* (1), 459-479.

187. Winnik, F. M. Phase transition of aqueous poly-(N-isopropylacrylamide) solutions: a study by non-radiative energy transfer. *Polymer* **1990,** *31* (11), 2125-2134.

188. Kujawa, P.; Winnik, F. M. Volumetric studies of aqueous polymer solutions using pressure perturbation calorimetry: A new look at the temperature-induced phase transition of poly (N-isopropylacrylamide) in water and D2O. *Macromolecules* **2001,** *34* (12), 4130-4135.

189. Gao, X. Y.; Cao, Y.; Song, X. F.; Zhang, Z.; Xiao, C. S.; He, C. L.; Chen, X. S. pH- and thermo-responsive poly(N-isopropylacrylamide-co-acrylic acid derivative) copolymers and hydrogels with LCST dependent on pH and alkyl side groups. *Jounal of Materials Chemistry B* **2013,** *1* (41), 5578-5587.

190. Farooqi, Z. H.; Khan, H. U.; Shah, S. M.; Siddiq, M. Stability of poly(N-isopropylacrylamide-co-acrylic acid) polymer microgels under various conditions of temperature, pH and salt concentration. *Arabian Journal of Chemistry* **2017,** *10* (3), 329-335.

191. Nayak, S.; Lyon, L. A. Photoinduced phase transitions in poly(N-isopropylacrylamide) microgels. *Chemistry of Materials* **2004,** *16* (13), 2623-2627.

192. Gao, Y. F.; Ahiabu, A.; Serpe, M. J. Controlled Drug Release from the Aggregation-Disaggregation Behavior of pH-Responsive Microgels. *ACS Applied Materials & Interfaces* **2014,** *6* (16), 13749-13756.

193. Du, H.; Wickramasinghe, R.; Qian, X. Effects of salt on the lower critical solution temperature of poly (N-isopropylacrylamide). *Journal of Physical Chemistry B* **2010,** *114* (49), 16594-604.

194. Freitag, R.; Garret-Flaudy, F. Salt effects on the thermoprecipitation of poly-(N-isopropylacrylamide) oligomers from aqueous solution. *Langmuir* **2002,** *18* (9), 3434-3440.

195. McAfee, M. S.; Annunziata, O. Effects of salting-in interactions on macromolecule diffusiophoresis and salt osmotic diffusion. *Langmuir* **2015,** *31* (4), 1353-61.

196. Sadeghi, R.; Jahani, F. Salting-in and salting-out of water-soluble polymers in aqueous salt solutions. *Journal of Physical Chemistry B* **2012,** *116* (17), 5234-41.

197. Rembert, K. B.; Paterova, J.; Heyda, J.; Hilty, C.; Jungwirth, P.; Cremer, P. S. Molecular mechanisms of ion-specific effects on proteins. *Journal of the American Chemical Society* **2012,** *134* (24), 10039-46.

198. Bruce, E. E.; Bui, P. T.; Rogers, B. A.; Cremer, P. S.; Van Der Vegt, N. F. Nonadditive Ion Effects Drive Both Collapse and Swelling of Thermoresponsive Polymers in Water. *Journal of the American Chemical Society* **2019,** *141* (16), 6609-6616.

199. Xu, W. W.; Gao, Y. F.; Serpe, M. J. Electrochemically color tunable poly(N-isopropylacrylamide) microgel-based etalons. *Journal of Materials Chemistry C* **2014,** *2* (20), 3873-3878.

200. Gao, Y. F.; Serpe, M. J. Light-Induced Color Changes of Microgel-Based Etalons. *ACS Applied Materials & Interfaces* **2014,** *6* (11), 8461-8466.

201. Fanaian, S.; Al-Manasir, N.; Zhu, K.; Kjøniksen, A.-L.; Nyström, B. Effects of Hofmeister anions on the flocculation behavior of temperature-responsive poly (N-isopropylacrylamide) microgels. *Colloid and Polymer Science* **2012,** *290* (16), 1609-1616.

202. Sorrell, C. D.; Serpe, M. J. Reflection order selectivity of color-tunable poly(N-isopropylacrylamide) microgel based etalons. *Advanced Materials* **2011,** *23* (35), 4088-92.

203. Sorrell, C. D.; Carter, M. C.; Serpe, M. J. A "paint-on" protocol for the facile assembly of uniform microgel coatings for color tunable etalon fabrication. *ACS Applied Materials & Interfaces* **2011,** *3* (4), 1140-7.

204. Duong-Ly, K. C.; Gabelli, S. B. Salting out of Proteins Using Ammonium Sulfate Precipitation. *Method Enzymol* **2014,** *541*, 85-94.

205. Held, C.; Cameretti, L. F.; Sadowski, G. Modeling aqueous electrolyte solutions: Part 1. Fully dissociated electrolytes. *Fluid Phase Equilibria* **2008,** *270* (1-2), 87-96.

206. Held, C.; Reschke, T.; Müller, R.; Kunz, W.; Sadowski, G. Measuring and modeling aqueous electrolyte/amino-acid solutions with ePC-SAFT. *The Journal of Chemical Thermodynamics* **2014,** *68*, 1-12.

207. Sadeghi, M.; Held, C.; Samieenasab, A.; Ghotbi, C.; Abdekhodaie, M. J.; Taghikhani, V.; Sadowski, G. Thermodynamic properties of aqueous salt containing urea solutions. *Fluid Phase Equilibria* **2012,** *325*, 71-79.

208. Sivanantham, M.; Tata, B. Swelling/deswelling of polyacrylamide gels in aqueous NaCl solution: Light scattering and macroscopic swelling study. *Pramana* **2012,** *79* (3), 457-469.

209. Flory, P. J. Principles of polymer chemistry. *Cornell University Press: Ithaca*, **1953**.

210. López-León, T.; Elaïssari, A.; Ortega-Vinuesa, J. L.; Bastos-González, D. Hofmeister effects on poly (NIPAM) microgel particles: macroscopic evidence of ion adsorption and changes in water structure. *ChemPhysChem* **2007,** *8* (1), 148-156.

211. Freire, M. G.; Carvalho, P. J.; Silva, A. M. S.; Santos, L. M. N. B. F.; Rebelo, L. P. N.; Marrucho, I. M.; Coutinho, J. A. P. Ion Specific Effects on the Mutual Solubilities of Water and Hydrophobic Ionic Liquids. *Journal of Physical Chemistry B* **2009,** *113* (1), 202-211.

212. Collins, K. D. Charge density-dependent strength of hydration and biological structure. *Biophysical Journal* **1997,** *72* (1), 65-76.

213. Grossfield, A. Dependence of ion hydration on the sign of the ion's charge. *The Journal of Chemical Physics* **2005,** *122* (2), 024506.

214. Combariza, J. E.; Kestner, N. R.; Jortner, J. Energy-structure relationships for microscopic solvation of anions in water clusters. *The Journal of Chemical Physics* **1994,** *100* (4), 2851-2864.

215. Mineur, Y. S.; Obayemi, A.; Wigestrand, M. B.; Fote, G. M.; Calarco, C. A.; Li, A. M.; Picciotto, M. R. Cholinergic signaling in the hippocampus regulates social stress resilience and anxiety-and depression-like behavior. *Proceedings of the National Academy of Sciences* **2013,** *110* (9), 3573-3578.

216. Higley, M. J.; Picciotto, M. R. Neuromodulation by acetylcholine: examples from schizophrenia and depression. *Current Opinion in Neurobiology* **2014,** *29*, 88-95.

217. Francis, P. T.; Palmer, A. M.; Snape, M.; Wilcock, G. K. The cholinergic hypothesis of Alzheimer's disease: a review of progress. *Journal of Neurology, Neurosurgery & Psychiatry* **1999,** *66* (2), 137-147.

218. Bohnen, N. I.; Albin, R. L. The cholinergic system and Parkinson disease. *Behavioural Brain Research* **2011,** *221* (2), 564-573.

219. Nirogi, R.; Mudigonda, K.; Kandikere, V.; Ponnamaneni, R. Quantification of acetylcholine, an essential neurotransmitter, in brain microdialysis samples by liquid chromatography mass spectrometry. *Biomedical Chromatography* **2010,** *24* (1), 39-48.

220. Persike, M.; Zimmermann, M.; Klein, J.; Karas, M. Quantitative determination of acetylcholine and choline in microdialysis samples by MALDI-TOF MS. *Analytical Chemistry* **2010,** *82* (3), 922-929.

221. Hestrin, S. The reaction of acetylcholine and other carboxylic acid derivatives with hydroxylamine, and its analytical application. *Journal of Biological Chemistry* **1949,** *180* (1), 249-261.

222. Vogt, N. Detecting acetylcholine. *Nature Methods* **2018,** *15* (9), 648-648.

223. Coutable, A. l.; Thibault, C.; Chalmeau, J. r. m.; François, J. M.; Vieu, C.; Noireaux, V.; Trévisiol, E. Preparation of tethered-lipid bilayers on gold surfaces for the incorporation of integral membrane proteins synthesized by cell-free expression. *Langmuir* **2014,** *30* (11), 3132-3141.

224. Wang, X.; Shindel, M. M.; Wang, S.-W.; Ragan, R. A facile approach for assembling lipid bilayer membranes on template-stripped gold. *Langmuir* **2010,** *26* (23), 18239-18245.

225. Zan, G. H.; Jackman, J. A.; Cho, N.-J. AH peptide-mediated formation of charged planar lipid bilayers. *The Journal of Physical Chemistry B* **2014,** *118* (13), 3616-3621.

226. Cho, N.-J.; Cho, S.-J.; Cheong, K. H.; Glenn, J. S.; Frank, C. W. Employing an amphipathic viral peptide to create a lipid bilayer on Au and TiO2. *Journal of the American Chemical Society* **2007,** *129* (33), 10050-10051.

227. Wu, W.; Zhang, J.; Zheng, M.; Zhong, Y.; Yang, J.; Zhao, Y.; Wu, W.; Ye, W.; Wen, J.; Wang, Q. An aptamer-based biosensor for colorimetric detection of Escherichia coli O157: H7. *PloS One* **2012,** *7* (11).

228. Yildirim, N.; Long, F.; Gu, A. Z. Aptamer based E-coli detection in waste waters by portable optical biosensor system. *40th Annual Northeast Bioengineering Conference (NEBEC)* **2014**, 1-3.

Appendix A: Preparation of Tethered-Phospholipid Bilayers on Microgel-Based Etalons for Sensing Application

A.1 Introduction

Acetylcholine is one of the most important neurotransmitter in the autonomic nervous system and functions as a neuromodulator (messenger) in both the central nervous system (CNS) and the peripheral nervous system (PNS). In the CNS, it plays crucial role in the processes related to behavioral activities and cognitive functions such as memory, attention, learning, language, and coordination while in the PNS, it activates muscle contraction. Metabolic abnormalities of acetylcholine (ACh) are associated with neuropsychiatric disorders and neurodegenerative diseases such as depression[215], schizophrenia[216], Alzheimer's disease[217], and Parkinson's disease[218]. Therefore, the detection and quantification of ACh in human fluids, such as blood and cerebrospinal fluid, is of great importance for diagnosis and monitoring the treatment progress of the above mentioned diseases. Common techniques used for quantifying ACh are liquid chromatography-mass spectrometry (LC-MS)[219], matrix-assisted laser desorption ionization time-of-flight mass spectrometry (MALDI-TOF-MS)[220], and colorimetric assays[221]. However, these methods are expensive and require highly trained personnel. Thus, a simple, inexpensive, fast, sensitive and selective method for detecting and quantifying ACh is highly needed.[222]

In this project, we intent to develop a biosensor for ACh utilizing nicotinic acetylcholine receptors (NAChR) embedded into a phospholipid bilayer immobilized on the surface of the etalon devices. NAChRs are ligand-gated ion channels permeable to ions such as sodium, potassium, and calcium, and capable of switching from a closed to an open state when acetylcholine binds to them, allowing ions to pass through in the open state. These ions would then react with the microgels located beneath the phospholipid bilayer, generating a color change in the device. Immobilization of the phospholipid bilayer and the detection procedure are illustrated in Scheme A1. We hypothesize that the shift in the reflectance spectrum from the etalons would be proportional to the concentration of acetylcholine in the biological sample because more NAChRs would be in an open state (and for longer periods) as the concentration of acetylcholine molecules increases, allowing more ions to flow through the ion channel and decreasing the charge-charge repulsions of the negatively charged carboxylic groups. Furthermore, this strategy allows the study of agonist and antagonist drugs on the activity of NAChRs, which is of great interest to study potential drugs for Alzheimer's and Parkinson's diseases.

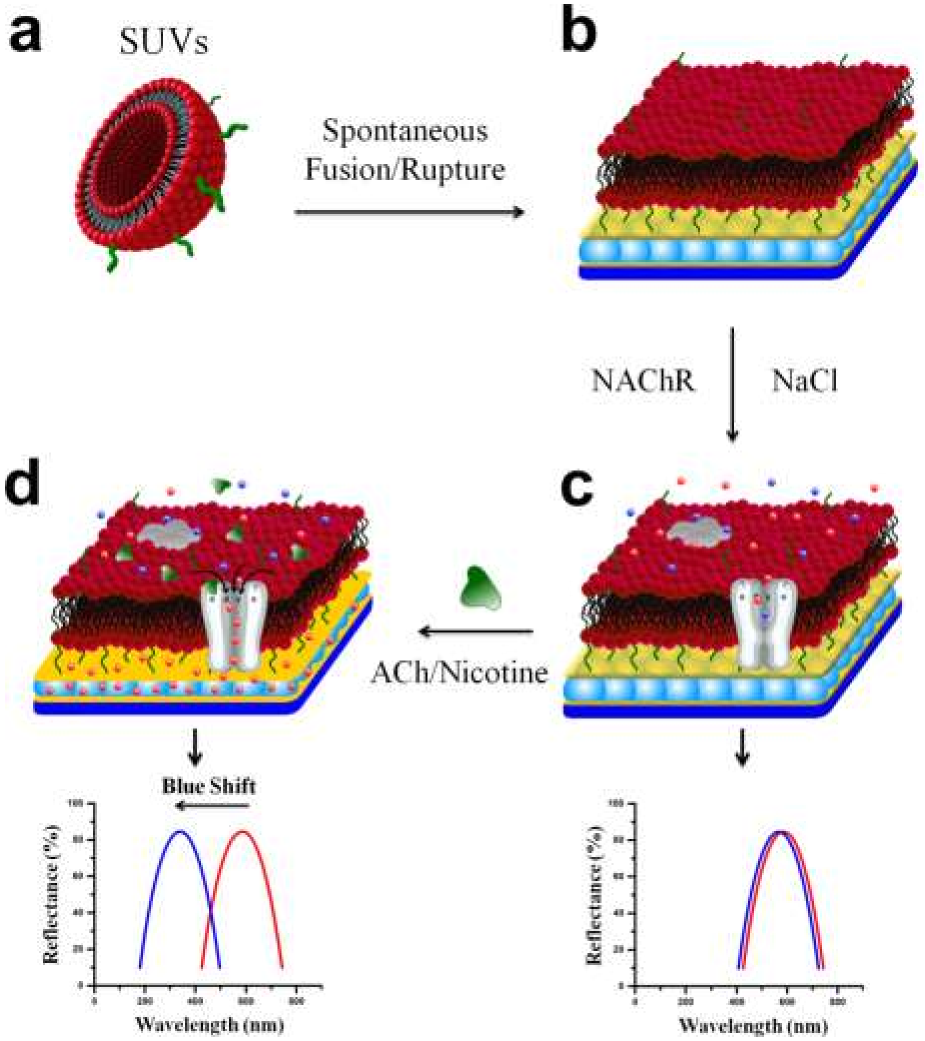

Scheme A.1 Illustration for the Ach/nicotine detection strategy. (a) Small unilamellar vesicles are prepared in PBS buffer containing disulfide groups to form Au-thiolate bond with the top Au layer of the etalon in order to facilitate vesicle rupture/fusion. (b) The unilamellar vesicle solution was slowly flushed on the surface of the etalons (625 mm^2) where they bind, rupture, and fuse, forming the supported lipid bilayer. (c) Once NAChRs are incorporated into the lipid bilayer, the addition of NaCl would not cause a shift in the reflectance spectra. (d) In the presence of Ach/nicotine, the NAChRs adopt an open conformation state that allows Na$^+$ ions to pass through and react with the microgel layer located beneath the bilayer, resulting in a shift in the reflectance spectrum.

A.2 Preliminary Experimental Results

The supported lipid bilayer (SLB) was prepared from the fusion and rupture of vesicles composed of 5% 1,2-distearoyl-*sn*-glycero-3-phosphoethanolamine-*N*-poly(ethylene glycol)-2000-*N*-[3-(2-pyridyldithio)propionate] (DSPE-PEG-PDP) and 95% 1-palmitoyl-2-oleoyl-*sn*-glycero-3-phosphocholine (POPC). The vesicles were prepared following a previously published protocol[223], but the vesicles were sizing by sonication instead of using an extruder. Vesicles composed of 100% POPC were used as a control experiment. DSPE-PEG-PDP contains a disulfide group that drives the adsorption and rupture of the vesicles into a bilayer. It has been reported that vesicles containing 2.5% of DSPE-PEG-PDP undergo spontaneous rupture and bilayer formation[224] and for lower DSPE-PEG-PDP contents, amphipathic a-helix (HA) peptide is crucial to induce vesicle rupture and the formation of the bilayer[223]. Furthermore, the PEG chains serve as a pillar to keep the bilayer about 10 nm from the support, providing the stability for these soft asymmetric films. DLS measurements showed that vesicle sizes for 5%DSPE-PEG-PDP/95%POPC and 100%POPC were 117.3 and 201 nm respectively. The smaller size for 5%DSPE-PEG-PDP/95%POPC is presumably due to the PEG chains that provide more stability for the vesicles, avoiding their further fusion. In addition, the size of 5%DSPE-PEG-PDP/95%POPC vesicles was higher than the one reported in the literature (around 60 nm), but we believed they were still small enough and could undergo vesicle rupture and bilayer formation. We first monitored the formation of the SLB on a glass substrate coated with 50 nm gold layer by real time surface plasmon resonance (SPR). The results are shown in **Figure A.1**. As we can see from Figure A.1(a), the vesicles composed of 5%DSPE-PEG-PDP/95%POPC first adsorb on the surface reaching a critical surface coverage (represented by the first slope) and then undergo rupture and bilayer formation (represented by a second slope) while vesicles composed of 100%POPC adsorb on the surface reaching a maximum surface coverage but does not rupture (represented by a single slope). DSPE-PEG-PDP contains a disulfide group that drives the adsorption/biding and rupture of the vesicles into a bilayer while POPC does not. This single slope observed in the real time SPR for vesicles containing 100% POPC indicates that there is no strong driving force for the formation of the bilayer and/or vesicles rupture due to the absence of the tethered group. In addition, we can see from the results that the rupture of the 5%DSPE-PEG-PDP/95%POPC vesicles occurs before reaching the maximum surface coverage. SPR curve measurements found in **Figure A.1(b)** show that the formed phospholipid bilayer continues to be stable after rinsing the system with PBS solution.

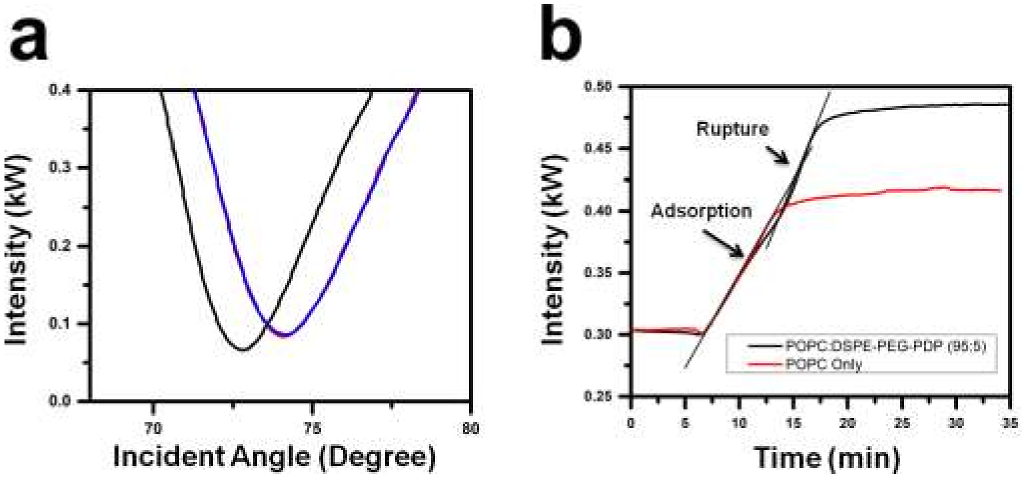

Figure A.1 (a) Real Time SPR curve monitoring the adsorption of vesicles composed of 100% POPC (black) and the adsorption and rupture of vesicles composed of 95%POPC/5%DSPE-PEG-PDP (red) to a 50 nm gold coated substrate. (b) SPR Curve measurement showing the stability of the bilayer after its formation.

Following, quartz crystal microbalance (QCM) was used to monitor the bilayer formation on bare gold and on an etalon. The results can be found in Figure A.2. 100%POPC based vesicles were used again as control and it was hypothesized that they would not rupture on the surface based on the real time SPE measurements. 5%DSPE-PEG-PDP/95%POPC vesicles were used as the bilayer forming vesicles as they can spontaneously rupture on the surface, supporting the observations obtained from SPR measurements. For the QCM experiments, a peristaltic pump was used to flow PBS (initial volume 10 mL) over the crystal/etalon. The crystal/etalon was equilibrated for 10 minutes before 1 mL of the desired vesicles (2 mM) was injected and allowed to flow in a cyclic mode. For QCM experiments on bare gold, bilayer formation was straightforward, and data was very reproducible. Again, as shown in **Figure A.2(a)**, vesicles composed of 100%POPC adsorb on the Au surface but don't undergo rupture as indicated by a fast decrease and plateaus in the frequency. In addition, the vesicles adsorb on the surface and stay on the surface even after rinsing. However, vesicles composed of 5%DSPE-PEG-PDP/95%POPC undergo vesicle rupture as indicated by an increase in the frequency after vesicle adsorption due to the loss of water trapped inside of the vesicles. These results are in agreement with previous reported QCM results.[223-225] To further confirm the formation of the bilayer, we introduced HA peptide after rinsing the system with PBS[225-226] (data not shown) and we could not observe any change, which indicates that the vesicles were already ruptured. Following, the formation of the bilayer was monitored using an etalon that was fabricated on the surface of the quartz crystal using pNIPAm-based microgels and 35 nm top gold layer (we could not observe the formation of the bilayer using 15 nm top gold layer). Due to the added complexity of the etalon-bilayer system, the results from these experiments were not very reproducible, but we could still see the formation of the bilayer characterized by a slightly increase in the frequency after injecting the solution of vesicles composed of 5%DSPE-PEG-PDP/95%POPC as shown in **Figure A.2(d)**. With the etalon system, we must consider multiple interfaces and simultaneous mass and liquid loading on the QCM sensor, which adds variability.

In the case of 100%POPC (**Figure A.2(c)**), QCM results showed that the vesicles first adsorb on the surface, indicated by a sharp decrease in the frequency, but they are gradually washed away as indicated by increase in the frequency, reaching almost the same initial frequency, which might be due to the absence of interaction between the gold and vesicles and the roughness of etalon surface roughness (around 10 nm measured by atomic force microscopy (AFM)).

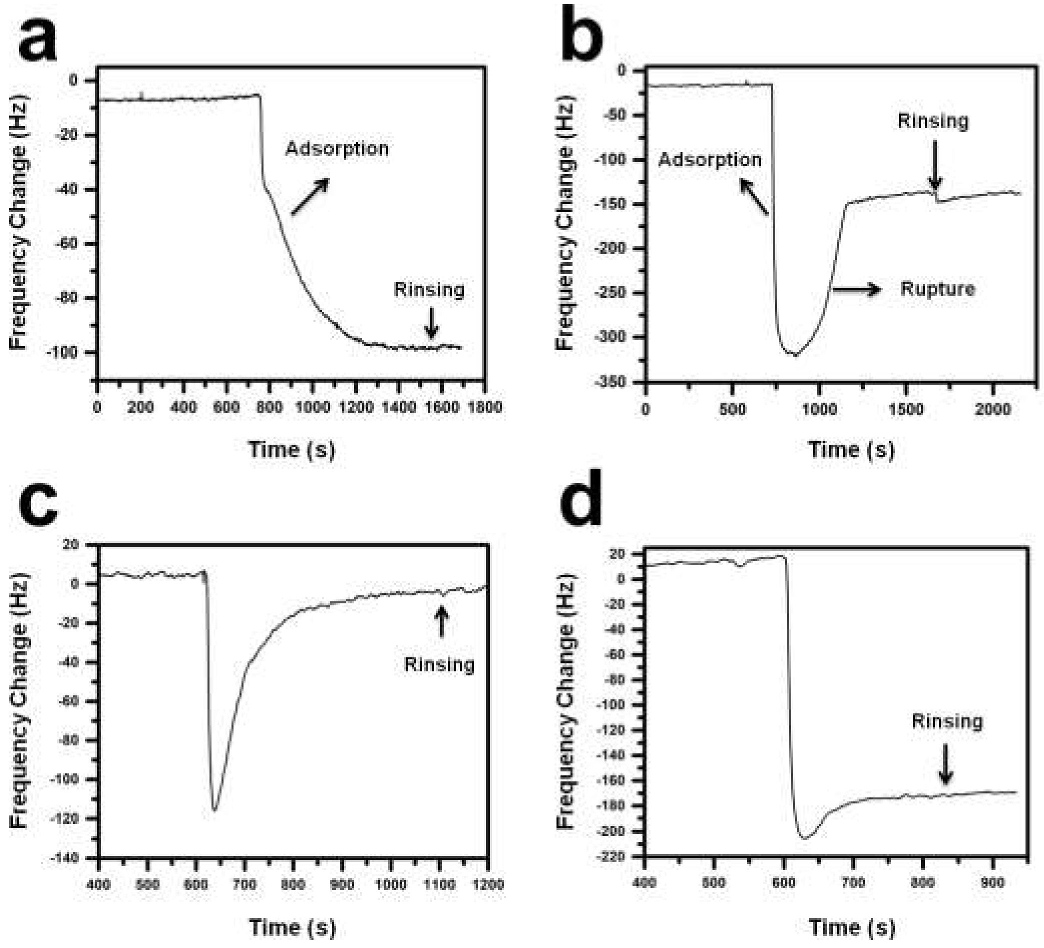

Figure A.2 Monitoring the frequency change using QCM for the vesicle adsorption/rupture process onto a gold surface (bare quartz crystal) for (a) 100% POPC vesicles and (b) 5%DSPE-PEG-PDP/95%POPC vesicles. Frequency change for vesicles composed of (c) 100% POPC and (d) 5%DSPE-PEG-PDP/95%POPC using an etalon device that was constructed on the surface of the quartz crystal.

Fluorescence microscopy measurements were also performed to visualize the phospholipid bilayer. Vesicles with fluorescent tagged lipid 1,2-dipalmitoyl-sn-glycero-3-phosphoethanolamine-N-(7-nitro-2-1,3-benzoxadiazol-4yl) (NBD-DPPE) were made and incubated on gold surfaces for 30 minutes. The composition of these vesicles was 5%DSPE-PEG-PDP/93%POPC/2%NBD-DPPE. The surfaces were viewed by fluorescence microscopy (500 nm laser). For these experiments, we were unable to get clear pictures but we could see that the region coated with gold was fluorescent and the glass portion was not as displayed in **Figure A.3**.

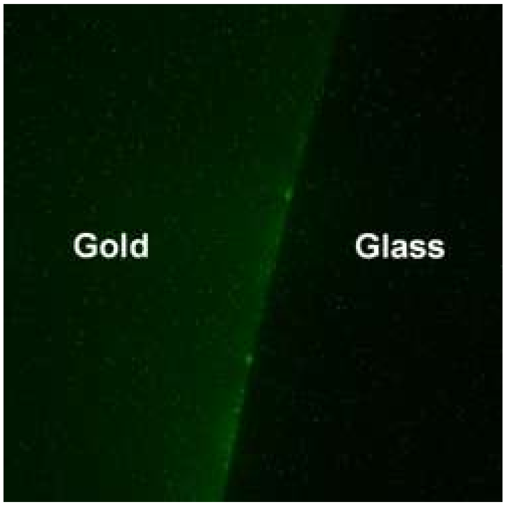

Figure A.3 Fluorescence microscopic images of the bilayer formed on the Au coated glass substrate.

We further performed reflectance spectrum measurements on etalons containing or not the SLB. For this, the surface of the etalon was washed with a solution of 5%DSPE-PEG-PDP/93%POPC vesicles, mimicking the QCM/SPR system. Again, the etalon size was 625 mm^2 with 35 nm top gold layer. The reflectance measurements is displayed in Figure A.4. The response to 0.1 M NaCl solution for etalons without the phospholipid bilayer was 12 ± 1 nm while for the etalon containing the bilayer, it was 1.2 ± 1.6 nm. As can be seen, the SLB can successfully block the flow of ions into the microgel layer as the shift observed in the reluctance spectrum upon addition of 0.1 M NaCl was not significant. Future steps would involve monitoring by QCM and SPR the insertion of alpha-hemolysin into the bilayer immobilized on a bare gold surface and also on the etalon and determine the concentration of alpha-hemolysin needed to get a response to 0.1 M NaCl from the etalons. Finally, alpha-hemolysin protein incorporation into the bilayer immobilized on the etalon was attempted and monitored by QCM, but no frequency shift was seen likely due to the QCM having a short penetration depth. Alpha-hemolysin was used a model transmembrane protein.

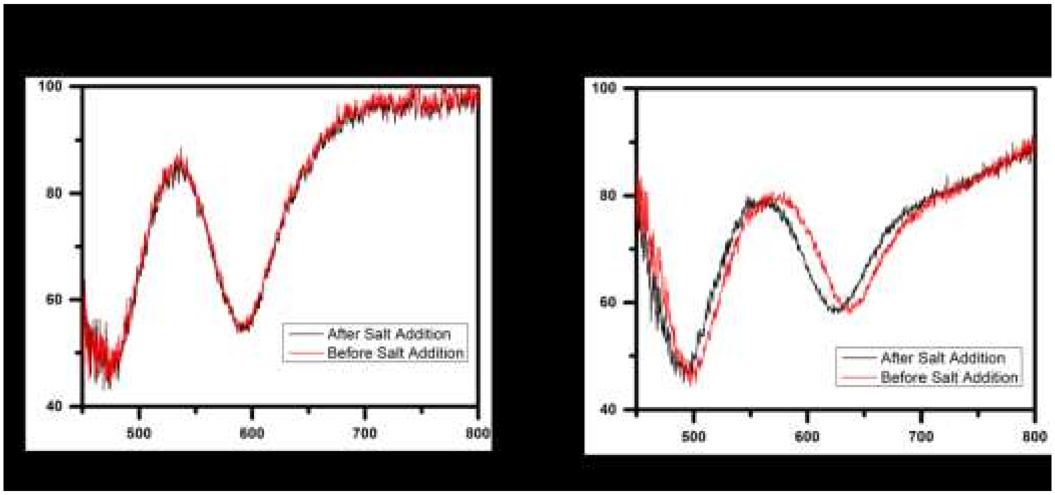

Figure A.4 Reflectance spectra from the etalons devices without a SLB (a) and containing a SLB (b) before (red) and after (black) the addition of 0.1 M NaCl solution. Due to the hydrophobic barrier provided by the SLB, ions cannot diffuse through the etalons top-Au layer and generate a peak shift. However, without the SLB, ions can diffuse to the microgels layer yielding a peak shift.

A.3 Conclusions and Future Outlooks

We have demonstrated using SPR and QCM that the formation of the bilayer occurs in two steps: adsorption and saturation of the vesicles on the surface followed by rupture. Furthermore, we have demonstrated that the SLB can effectively block the flow of salt, observed by no shift in the reflectance spectra. In future work, alpha-hemolysin could be used to evaluate the etalon response to salt. In this way, one could verify if the flow of cations through the membrane protein is enough to generate a shift in the reflectance spectra. Following, NAChRs could be incorporated into the vesicles and a calibration curve could be obtained by varying the concentration of ACh and keeping the concentration of NaCl (0.1 M).

Appendix B: Preparation of Micron-Sized Etalon Optical Devices for Detecting *E. coli* in Aqueous Solution

B.1 Introduction

Point-of-care (POC) diagnostics have become extremely important for disease diagnosis, especially in economically strained regions because they are often inexpensive, portable, simple to manufacture, requires no training to use and little to no sample preparation. Photonic materials belong to a class of optical materials that can interact with the incident light to produce color and have been extensively used for POC proposes. Several materials have been used to fabricate these devices. Among them, stimuli-responsive polymers have garnered significant interest over the last couple of decades. Our group fabricated optical devices called etalons by sandwiching pNIPAm-*co*-AAc microgels between two thin gold films that can respond to a number of external stimuli such as temperature, pH, and ionic strength. We have previously demonstrated that the Au overlayer of the etalon contains porous and the porosity can be controlled by varying its thickness. As the thickness of the top-layer increases, the porosity decreases, leading to slower response kinetics. This project involves the application of etalons for the detection of *Escherichia coli (E. coli)* in water sources by monitoring the kinetics of the color change. In this new approach, illustrated in **Scheme B.1**, the top Au layer of the etalons fabricated using pNIPAm-*co*-AAc microgels are modified with aptamers that can specifically bind to *E. coli*. When *E. coli* are captured and immobilized on the surface of the etalons, their response to salts, such as NaCl, is slowed down due to the blockage some porous on the top-layer, which is characterized by slower kinetic response. Our objective is to develop a portable, low-cost, rapid analysis time, and easy-to-handle device for detection of microbiological pathogens, such as *E. coli* O157:H7, in water while maintain high accuracy and a limit of detection down to a single *E. coli* cell.

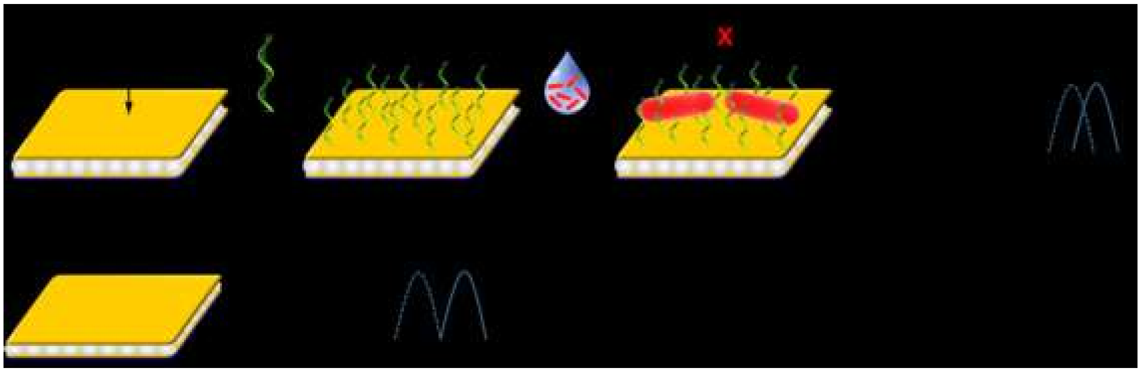

Scheme B.1 Detection strategy for *E. coli* in solution.

B.2 Preliminary Experimental Results

Our group has been working with 6.25 or 1.00 cm^2 etalons, however, for the detection of low bacteria concentration using large surface area etalons is difficult to capture any change in the response kinetics due to the blockage of a few porous. Thus, the fabrication of smaller size etalons is required for such application. In this project, we intent to develop micrometer sized etalons and evaluate their ability to detect *E. coli* in aqueous solutions. The micro etalons were fabricated by two step photolithography using two photomasks made of soda-lime glass chrome coated (~100 nm thickness) to create the features as shown in **Figure B.1**. The first photomask (Figure B31(a)) contained squares of 25, 100, and 400 μm^2 while the squares in the second photomask were 1 μm larger. In the first step of the photolithography process, squared glass substrates of 4 x 4 inch were cleaned with piranha solution (3:1 H_2SO_4/H_2O_2 for 15 minutes), washed with large amount of water, and dried with N_2 gas. Following, the glass substrates were baked to remove any adsorbed water on the surface and treated with 1,1,1,3,3,3-hexamethyldisilazane (HMDS) applied in gas form (vapor priming) to increase adhesion of the photoresist on the glass substrate and avoid further contamination with water. In the second step, the glass substrates were spin coated with two positive photoresists: LOR5B and HPR504. For this, around 5 mL of LOR5B was deposited on the center of the glass substrate, spin coated for 10 sec at 500 rpm and then 40 sec at 3000 rpm, baked at 145 ^{o}C for 5 min, and allowed to cool down for 10 min. Next, around 5 mL of HPR504 was deposited on the center of the glass substrate coated with LOR5B, spin coated for 10 sec at 500 rpm and then 40 sec at 3000 rpm, baked at 115 ^{o}C for 90 sec, and allowed to cool down for 10 minutes. Following, for the mask alignment and UV light exposure, the first photomask was placed on top the glass substrates, aligned and exposed of UV light for 2.5 sec in contact mode. The features were obtained by developing the top HPR504 photoresist layer using 354 positive photoresist developer for 20 seconds and the bottom LOR5B photoresist layer using MF 319 developer for 2 sec. The glass substrates were coated with 2 nm Cr and 15 nm Au using a thermal evaporation system. The substrates were placed on the hotplate set at 35 ^{o}C where a preconcentrated microgel solution was spread on the surface and allowed to dry for 2 hours. Following, the excess microgel was removed by washing the substrates with large amount of water and the photoresist was removed using Remover PG. Photographs of the resulting bottom Au layer coated with microgels can be found in **Figure B.2**. For the top Au layer, all the procedures from step 2 was repeated but using the second photomask. It was very difficult to obtain etalons of 25 and 100 μm^2 due to the alignment procedure. However, etalons of 400 μm^2 could be obtained as shown in **Figure**

B.3(a). Still, the alignment of the second photomask was difficult an resulted on etalon partially covered as shown in **Figure B.3(a)**.

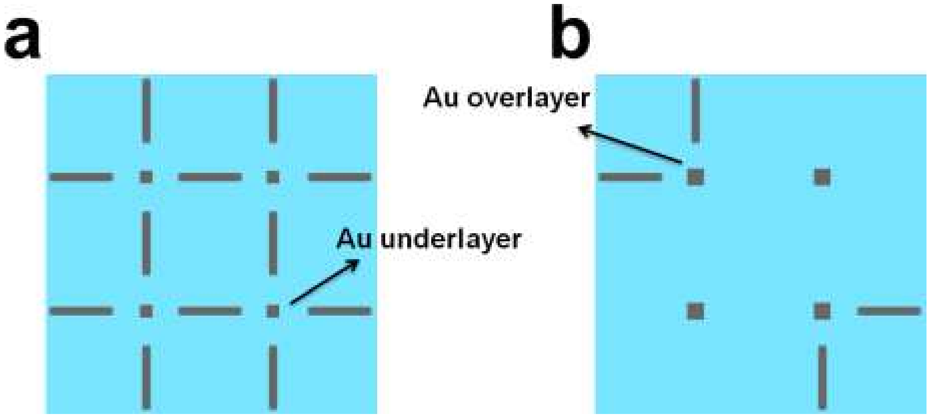

Figure B.1 Illustration of the patterns fabricated on the two photomasks used: (a) first mask to create the bottom Au layer and (b) second mask to deposit the top Au layer. Blue regions are glass and gray regions are chrome. The chrome square of the second mask is 1 µm bigger than the squares on the first mask. Vertical and horizontal lines are used to locate the etalons easily.

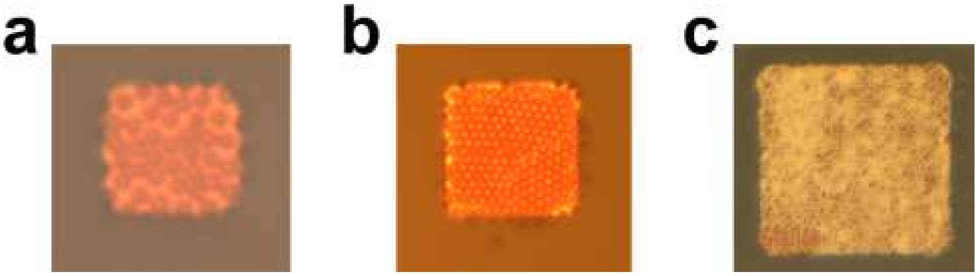

Figure B.2 Optical microscopic imagens for (a) 25 (c) 100, and (d) 400 μm^2 Cr/Au bottom layer coated with microgels.

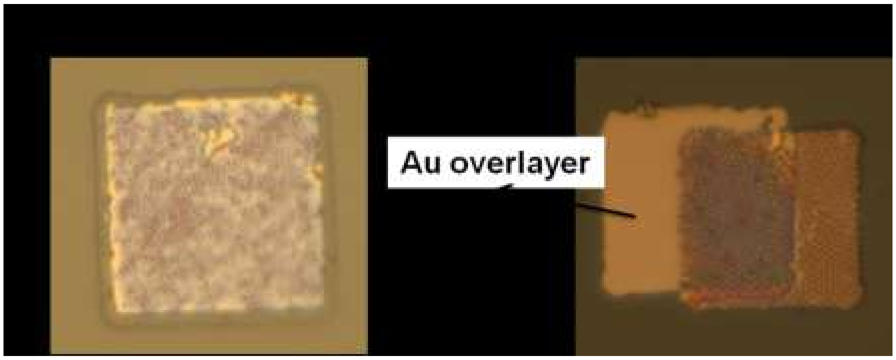

Figure B.3 Optical microscopic images for etalons of 625 μm^2 with the top Au layer perfect aligned (a) and not aligned (b).

In parallel, the immobilization of the aptamers on a Au coated glass substrate was performed and the immobilization of E. coli on the surface was evaluated. Scheme B.2 illustrates the immobilization procedure. Here, Au coated (50 nm thickness) substrates were immersed in a aptamer (sequence: CCG GAC GCT TAT GCC TTG CCA TCT ACA GAG CAG GTC TGA CGG)[227-228] solution of 1 μM for 20 hr. Following, the substrates were rinsed with DI water and incubated in a solution of 1 mM of 6-mercapto-1-hexanol (MCH) for 2 hours. Next, the substrates were washed with DI water and incubated in 10 mM PBS bufferpH 7.4 containing 1.5 mM of $MgCl_2$ for overnight at room temperature after which they were transferred to a *E. coli* solution of 10^7 CFU/mL also prepared in PBS buffer, pH 7.4, 1.5 mM MgCl2 but containing 0.05% wt BSA. The substrates were rinsed carefully with DI water and imaged with SEM which are shown in Figure B.4. For the control experiments, the substrates were only immersed in the MCH solution (no aptamers).

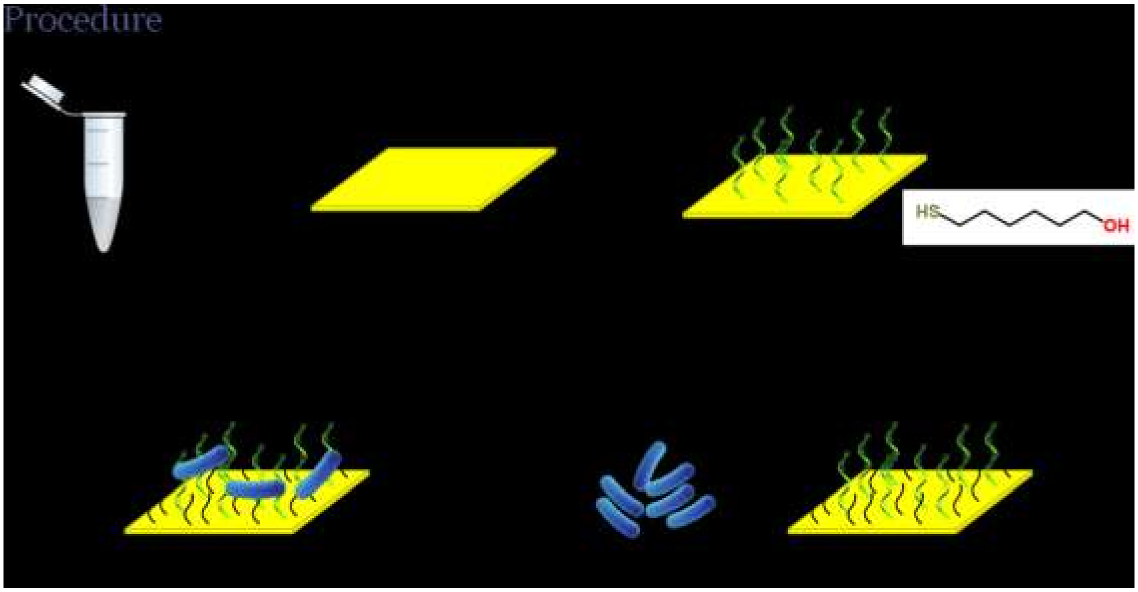

Scheme B. 2 Immobilization procedure for the thiol modified aptamer and *E. coli* capture.

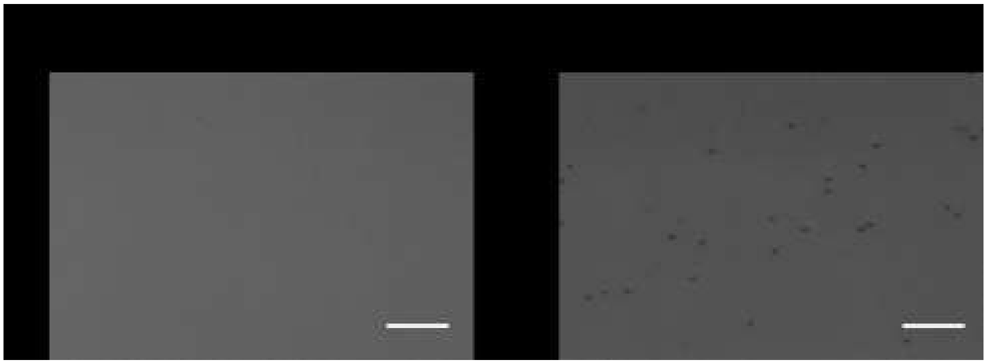

Figure B.4 SEM images for (a) control experiments and (b) *E. coli* immobilization by aptamers on a Au coated glass substrate. The white scale bars correspond to 20 μm.

B.3 Conclusions and Future Outlooks

Micro etalon devices with size of 625 μm^2 were fabricated by photolithography. Smaller etalons could not be fabricated due to complications with the second mask alignment. Furthermore, the ability of the aptamers to bind and immobilize *E. coli* was investigated. For control experiments, no E. coli was observed on the surface due to the lack of aptamers while very low concentration of *E. coli* could be seen for the substrates containing the aptamers. In future, studies focused to increase E. coli immobilization on the surface should be carried out and the color change of the micro etalons can be characterized using an optical microscope in reflection mode.

Appendix C: Box #1 Dimensions

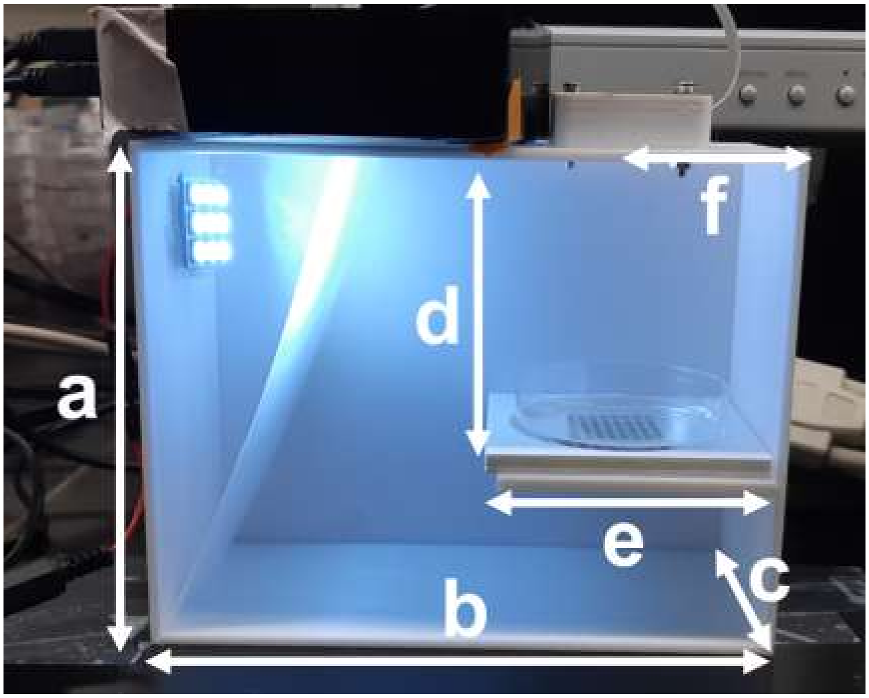

Figure C Photograph of Box #1 showing the dimensions where a = 12 cm, b = 15 cm, c = 6.9 cm, d = 7.3 cm, e = 6.5 cm, and f = 3 cm.